Ultra-low-dose CT-based attenuation correction for respiratory motion compensation in PET/CT imaging

Tzu-Cheng Lee

A dissertation

submitted in partial fulfillment of the

requirements for the degree of

Doctor of Philosophy

University of Washington

2017

Reading Committee:

Paul Kinahan, Chair

Adam Alessio

Michalakis Averkiou

Program Authorized to Offer Degree:

Bioengineering

University of Washington

Abstract

Ultra-low-dose CT-based attenuation correction for respiratory motion

compensation in PET/CT imaging

Tzu-Cheng Lee

Chair of the Supervisory Committee:
Professor Paul Kinahan
Department of Radiology

Positron emission tomography (PET) is a commonly used imaging tool in the management of patients with lung cancer and is of considerable interest in quantitative imaging of the thorax. Mismatch of PET data with computed tomography (CT) attenuation correction (CTAC) due to respiratory motion is a known source of errors in PET imaging. In theory, this can be corrected by matching individual PET and CT phases which have been generated by respiratory-correlated PET and CT. However, due to the high variability of patient breathing patterns and the nature of the scanning time differences between PET and CT, current respiratory-gated CTAC protocols for the irregular breather may cause additional bias in the PET image values. A ten-fold extension of the CT scanning time duration helps reduce PET imaging bias, but leads to the higher radiation dose to the patient. Lowering the CT source flux level to reduce dose, however, leads to increased noise

and bias. Here we test the possibility of using model based iterative reconstruction algorithms (MBIRs) for generating the sparse-view, ultra-low-dose (i.e. an order lower than current low-dose protocols) CTAC images for both phantom and patient PET data. We also propose a new variance estimation model, which considers statistical changes caused by the non-positivity correction process, for the MBIR algorithms. The model based iterative CT reconstruction approach does generate more accurate CTAC map compared to current approaches. However, since iterative reconstruction algorithms typically assume a normal distribution of the attenuation data, we tested if the assumption is still valid in the ultra-low-dose regime. The simulation and empirical ultra-low-dose CT studies showed a skewed post-log likelihood distribution in certain ranges. The information delineates the estimation limits of model based iterative reconstruction approach on the ultra-low-dose CT imaging, and potentially helps guide scanning protocols customized for a lowest-reasonable radiation dose.

TABLE OF CONTENTS

i

LIST OF FIGURES

LIST OF TABLES

ACKNOWLEDGEMENTS

Special thanks to my collaborators at GE Healthcare: Drs. Bruno De Man, Xue Rui, Lin Fu, and Paul Fitzgerald. It was a great honor for me and a blissful experience to work with these top-notch scientists, your suggestions and advice really widen my thoughts in this thesis. I would also like to thank all of my past committee members: Drs. Chun Yuan, Mike Averkiou, Eric Siebel, George Sandison, Ruikang Wang, and Gunther Uhlmann, for your precious comments and guidance.

Very grateful to my previous advisors at UCSF: Drs. Youngho Seo and Grant Gullberg, you enlightened my interest for the research in CT and nuclear medicine imaging, and I could not even start this amazing journey without your encouragement, many thanks. A very special gratitude goes to my program advisors: Marta, Peggy and Dorian, all staffs, and my classmates at UW-Bioengineering graduate program. What a great program!

I always consider myself as the luckiest person in Seattle for meeting all my friends here, where it never rains or gloomy because of you guys. Finally, I would like to thank my family, without your support, I wouldn't have had enough strength and faith for doing all of these. Thanks, love you.

DEDICATION

In memory of my Aunt Chiu-Ling,

your selfless love continues to inspire me today.

Chapter 1. MOTIVATIONS AND SIGNIFICANCE

Both single-photon emission computed tomography (SPECT), and in particular positron emission tomography (PET), are unique in medical imaging for their high sensitivity and direct link to a physical quantity, i.e. radiotracer concentration. This gives PET and SPECT imaging unique capabilities for accurately monitoring disease activity for the purposes of clinical management or therapy development. However, to achieve a direct quantitative connection between the underlying radiotracer concentration and the reconstructed image values several confounding physical effects have to be estimated, notably photon attenuation and scatter. With the advent of dual-modality SPECT/CT (CT: computed tomography), PET/CT, and PET/MR (MR: magnetic resonance imaging) scanners, the complementary CT or MR image data can enable these corrections, although there are unique challenges for each combination. This chapter covers the basic physics underlying photon attenuation and scatter and summarizes technical considerations for multimodal imaging with particular regard to PET quantification and methods to address the challenges for each multimodal combination.

1.1 WHAT IS HYBRID IMAGING

PET and SPECT imaging have been used to contribute important functional information such as perfusion, tissue metabolism, receptor density, and other functional parameters regarding both oncologic and non-oncologic disease activity which is not easily obtained by other clinical methods. However, PET and SPECT often lack morphological information needed to localize the disease. The combination of both functional and morphological modalities into single devices, like PET/CT, SPECT/CT and PET/MR, provides a solution for offering both the functional and

morphological information in a single-study evaluation of patients in clinical practice[1-4] (*see Figure 1-1, Figure* 1-2). The synergism of combining imaging modalities into a single device with shared mechanical components offers images with potentially less functional to morphologic alignment errors than multiple distinct systems that acquire images separately. Moreover, combining with anatomical imaging removes the need for additional time and cost for the transmission scan for the attenuation correction (AC)[5-7]. In other words, the synergism of CT or MRI with PET and SPECT not only provides the precise anatomical localization of regions identified by the uptake of radionuclide tracers, but also offers essential anatomical information for AC so that the uptake value can be correctly quantified. Herein, I review CT-based AC methods for PET and SPECT, and also MR-based AC methods for PET; starting with a brief explanation of the physics of attenuation of x-ray and nuclear medicine signals. Next, we discuss the advantages and disadvantages for doing AC. We summarize CT-based AC methods commonly used with PET and SPECT today and then discuss the evolving field of MR-based AC for PET. Finally, we review challenges for CT- and MR-based AC methods and possible approaches for future pursuit.
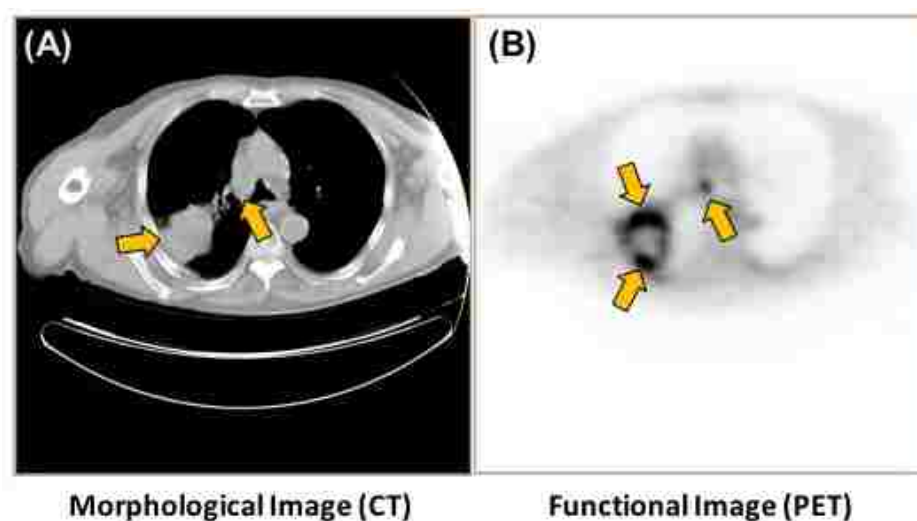
Figure 1-1. Hybrid PET/CT imaging offers complimentary information in one scan

(A) CT image shows good anatomical detail but no functional information while (B) PET shows tracer uptake in lesions but with limited morphological information.
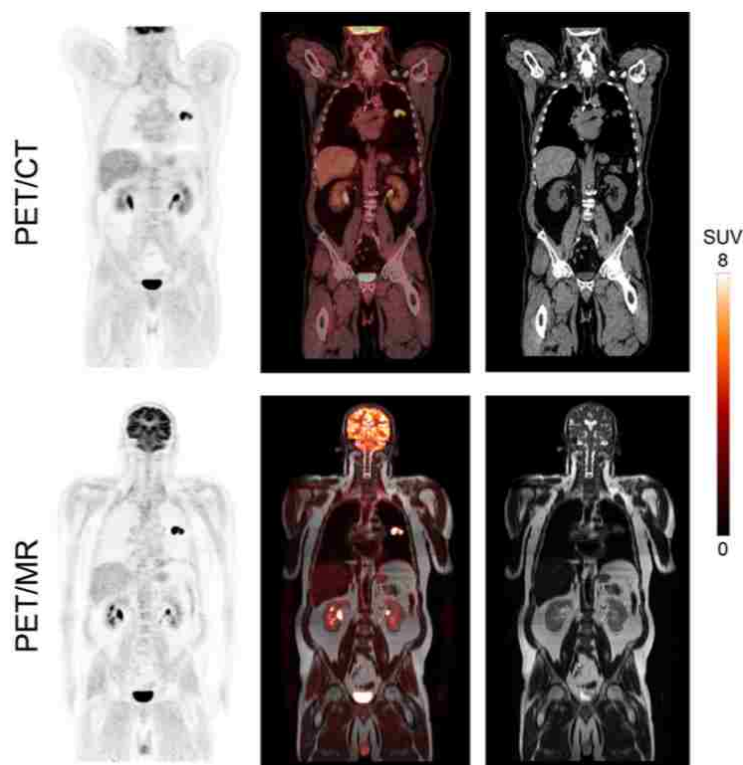
Figure 1-2. PET/CT vs PET/MR images from a same patient[4]

PET/CT imaging at approximately 1 h after injection of 15 mCi of 18F-FDG followed by PET/MR imaging at 1 h and 10 min after PET/CT imaging.

1.2 WHY ATTENUATION CORRECTION

In addition to the tasks of cancer detection and staging, PET and SPECT imaging are becoming more important as a quantitative indicator for individual treatment planning or response evaluation for therapy[3]. However, numerous corrections need to be performed before the measured signal can provide insight into the response to therapy. Physical effects like photon attenuation, scattered and random coincidences (PET), depth-dependent blur (SPECT), collimator effect (SPECT), variance

of the detector efficiency, and geometric dependent signal response can all perturb tracer uptake values in the image[2,8-10]. Of these, the most important effect in PET imaging is photon attenuation. In SPECT imaging, attenuation is also an important factor. As the emission photon from PET and SPECT tracers travel through the body it can be absorbed or scattered; the combination of these interactions is described as the linear attenuation of the photons. Essentially, all physical interactions that cause photons to deviate from a straight line contribute to linear attenuation. The attenuation effect not only leads to underestimation of the uptake activity, it also causes inhomogeneous bias of activity's distribution due to the different attenuation paths from the tracer source to detector. Some common artifacts such as enhanced activity in skin and in pulmonary regions ('hot' lungs) or negative tracer concentrations in mediastinal regions can be seen in uncorrected images[11] (*see Figure 1-3*). The lack of attenuation correction can also mask the presence of hot features, such as solid lesions with moderately elevated tracer uptake, or cold regions, such as mildly ischemic regions on cardiac perfusion exams[6]. However, reconstructing radionuclide images without AC can still provide complementary information, for example: to check for the presence of artifacts introduced by patient motion or mechanical misalignment occurring between the emission and attenuation maps (*see Figure 1-4*), or to check problems solely with the attenuation map. Therefore, for many applications, best practice dictates the review of images generated with and without attenuation correction[6].

PET image without AC — **PET image with AC** — **CT image**
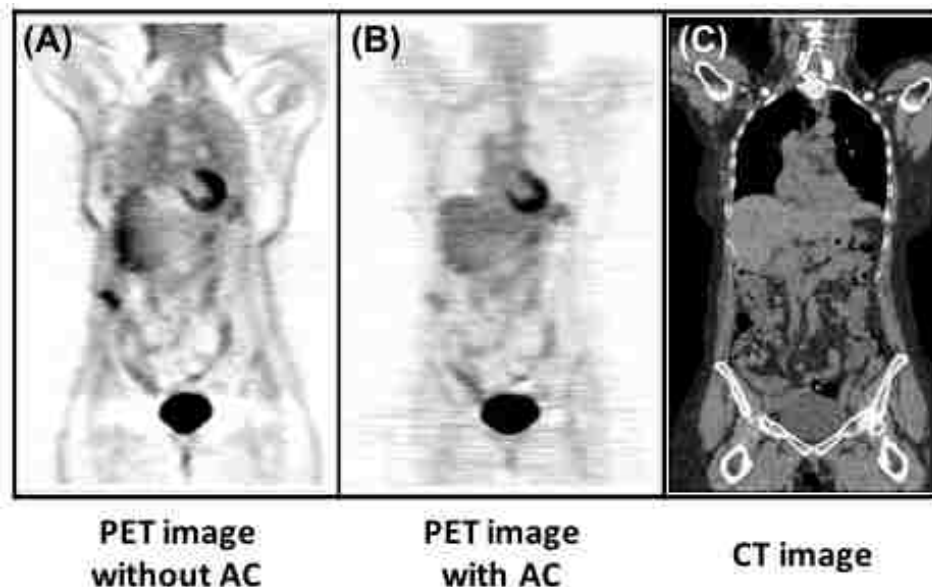
Figure 1-3. Accurate PET images require correction for photon attenuation

(A) PET image without attenuation correction, showing several artifacts. (B) PET image with CT attenuation correction. (C) Corresponding CT image.

PET image fused with CT — **PET image with AC** — **PET image without AC**
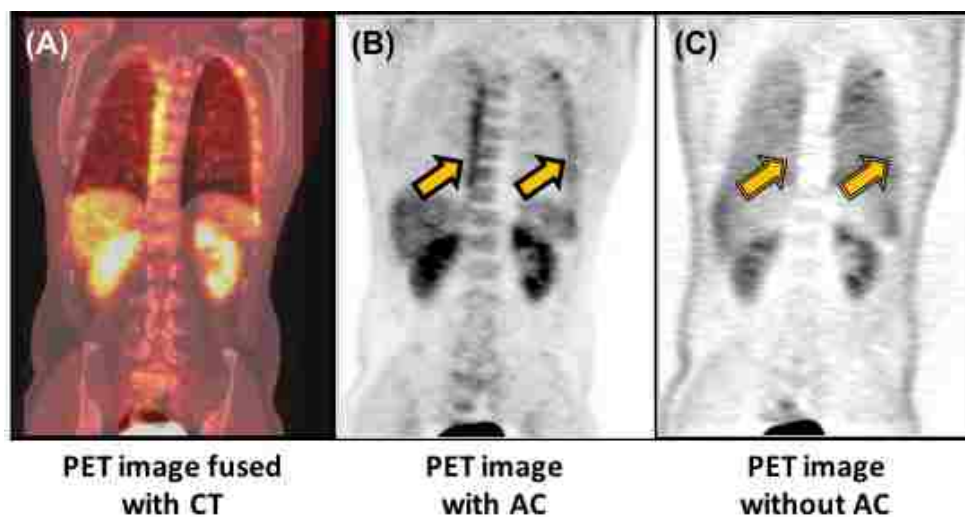
Figure 1-4. Artifacts when a patient shifted between CT and PET scans

(A) Elevated tracer uptake evident at one side of lung boundaries in the PET/CT fused image. (B) PET image with CT-based attenuation correction with increased uptake value at lung boundaries (arrows). (C) The PET image without attenuation correction does not show elevated uptake at same locations (arrows).

1.3 ATTENUATION AND ATTENUATION CORRECTION

A photon's probability of traveling along a straight line through material is an exponential function of the linear attenuation coefficient (LAC, μ_l, usually expressed in cm^{-1}) of the absorber and the path length[8,12]. Under conditions of narrow-beam geometry, the transmission of a mono-energetic photon though an absorber can be expressed in the exponential equation:

$$I(x) = I(0)e^{-\mu_l x} \quad [1]$$

where $I(x)$ is the photon intensity transmitted through the thickness (x) of the absorber. The quantity of μ_l linearly related with the absorber density (ρ). The mass attenuation coefficient (μ_m, usually expressed in cm^2/g) for a specific material with a specific μ_l can be expressed as:

$$\mu_l = \mu_m \cdot \rho \quad [2]$$

For the range of photon energies in nuclear medicine and radiology, the attenuation is due to three potential interactions, where τ represents photoelectric effect, σ represents Compton scattering effect, and κ stands for the pair production effect, resulting in:

$$\mu_m(Z,E) = \tau + \sigma + \kappa \quad [3]$$

The relative magnitude of τ, σ, and κ varies with the atomic number (Z) of the absorber and the photon energy (E). Consequently, LAC varies in different transmitted materials (e.g. bone or muscle) and photon energies (e.g. 10 to 1000 keV). In Figure 1-5[13], as expected, total $\mu_{m,bone}$ is higher than total $\mu_{m,muscle}$ because the effect of atomic number's difference. On the other hand, we could see the photoelectric effect (τ) dominates the change of total μ_l for lower photon energy while Compton scattering (σ) dominates the total μ_l value for photon energy higher than 100 keV (*see Figure 1-5*). We do not consider the pair production effect in the emission imaging here since it only occurs for the photon energies higher than 1.022 MeV. The density and Z dependent properties of LAC are reasons why an AC method incorporating knowledge of the non-uniform

morphology is preferred to simple uniform AC methods. The energy dependent property of LAC also explains why the LAC for x-ray (e.g. 50-80 keV mean energy for CT) needs to be carefully "scaled" for doing the CT-based attenuation correction of the emission data for γ-rays (e.g. 140 keV for ^{99m}Tc), and the annihilation photons (511 keV).
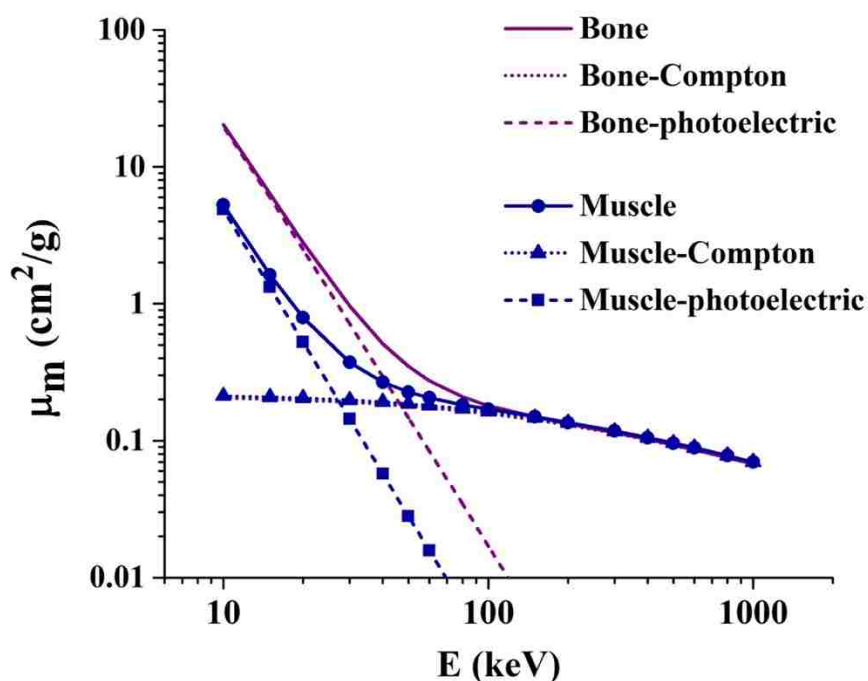
Figure 1-5. Mass attenuation coefficients (μ_m) for bone and muscle

The photoelectric absorption and Compton scattering components are also shown. The total attenuation coefficient accounts for all photon interactions, not just photoelectric absorption and Compton scattering

The equation for SPECT and PET signal (P) along each line of response (LOR) of the scanner, where r and θ represent the LOR at radial location r with the projection angle of θ is shown below. The signal is essentially the integral of activity, A, along the LOR, between the emission source location, s, and the detector location D. The signal is attenuated based on the exponential relationship with the LAC and the attenuation path length, l'. Again, μ is the LAC of the LOR, and *E* is the emitted photon energy

$$p_{SPECT}(r, \theta) = \int_s^D A(l) \cdot exp\left\{-\int_s^D \mu(l'; E)dl'\right\} dl \quad [4a]$$

$$p_{PET}(r, \theta) = \int_{-D}^D A(l) \cdot exp\left\{-\int_s^D \mu(l'; E)dl'\right\}\left\{-\int_{-D}^s \mu(l'; E)dl'\right\} dl$$

$$= \int_{-D}^D A(l)dl \cdot exp\left\{-\int_{-D}^D \mu(l'; E)dl'\right\} \quad [4b]$$

To correct for the effects of attenuation, one needs to know the inverse of the exponential signal loss in the above equation [4]. This correction term is called the attenuation correction factor (ACF). For SPECT, this factor is a function of r, θ, s.

$$e.g. \; ACF_{SPECT}(r, \theta, s) = exp\left\{\int_s^D \mu(l'; E)dl'\right\} \quad [5a]$$

For PET, this factor is only a function of r and θ.

$$e.g. \; ACF_{PET}(r, \theta) = exp\left\{\int_{-D}^D \mu(l'; E)dl'\right\} \quad [5b]$$

In other words, in order to accurately compensate the effect from attenuation, one needs to know both LAC (μ) and the attenuation path length (s') for each position in the scanning object. Considering that the PET signal comes from two photons leaving the radionuclide emitter in opposite directions, the attenuation path length is a fixed value for each LOR in PET no matter where along the LOR the photons originate (*eq. [4b]*). In contrast, in SPECT, the signal originates from a single photon and the attenuation experienced by that photon depends on the location of the emission (*eq. [4a]*). Consequently, it is slightly harder to correct for attenuation in SPECT. In SPECT imaging, *Chang's multiplicative method* provides a relatively simple attenuation correction method [12,14]. In this approach, an initial emission image f´ (x, y) is reconstructed and the boundary of it is delineated without any attenuation correction. For each pixel f (x, y) in the recon image, the attenuation path lengths (s') of every projection angle (θ) is then measured based on

the approximated boundary information. This approach is usually implemented with the assumption of identical LAC (μ) values throughout the scanning object leading to the ACF calculated by summing the impact of attenuation from all angles at each emission location[12]:

$$ACF(x, y) = \frac{1}{\frac{1}{N}\Sigma_{\theta=1}^{N} e^{-\mu \cdot s_\theta'}} \quad [6a]$$

Finally, the reconstructed image is corrected pixel-by-pixel multiplying with ACF:

$$f(x, y) = f'(x, y) \cdot ACF(x, y) \quad [6b]$$

The attenuation correction based on Chang's approach provides reasonable results especially for the brain and abdomen images where the assumption of uniform attenuation is reasonable. Many SPECT systems still offer this correction technique today; however, a more elaborate method for carefully considering the inhomogeneity of LAC distribution in the regions like the thorax and pelvic regions is needed.

1.4   ATTENUATION CORRECTION FOR PET AND SPECT IMAGING BEFORE CT

For both PET and SPECT imaging, accurate attenuation correction factors were originally estimated from a transmission scan at the same or similar photon energy. This approach used an additional radionuclide source to do a transmission scan on the scanning object. Rod, line or flood source containing a radionuclide, e.g. ^{123m}Te ($T_{1/2}$ = 120d, Eγ = 159 keV) and ^{68}Ge/^{68}Ga ($T_{1/2}$ = 270d, E$_{annihilation}$ = 511 keV), with similar photon energy but much longer half-life compared to the emission source were used to rotate around the object for 360 degrees to get a full set of projections. Often, these projections were acquired using the same detectors as the native emission detectors. The ACF for PET images can be easily estimated by dividing the reference scan (blank scan, I_0) with transmission scan.

$$ACF(r, \theta) = \frac{p_{reference}(r, \theta)}{p_{transmission}(r, \theta)} = \frac{I_0}{I_0 \cdot \exp\{-\int_{-D}^{D} \mu(l'; E)dl'\}} \quad [7a]$$

$$p_{corrected}(r, \theta) = p_{emission}(r, \theta) \cdot ACF(r, \theta) \quad [7b]$$

For SPECT images, the attenuation correction factor must be estimated for each location in the object. With modern iterative methods, the emission image is estimated first without attenuation correction and the non-uniform ACF factors are applied to this image; With each iteration, the emission image becomes more accurate and the ACF factors converge to more accurate values. Initially, some drawbacks of the transmission scan-based attenuation correction method impeded its application in practice. There were active "To AC or Not to AC" debates in the nuclear medicine community[15-17]. In summary: (1) the transmission scan adds considerable scan time (~10-45mins) so that the patient throughput or the emission scan time is compromised; (2) the transmission scan is relatively noisy, and the noise will be propagated to the emission scan and further degrade the final image quality; (3) patient movements between the transmission and emission scan (both tens of minutes) lead to mis-registration of the attenuation correction map and artifacts; (4) the transmission scan signal could be contaminated by the injected radionuclide for the emission scan, and (5) an additional cost for periodically replacing and maintaining the transmission sources.

Some variant of the transmission scan-based AC had been developed for coping with the image noise and the extended acquisition time. Instead of directly using the transmission map for AC, a segmented AC technique separates the transmission image into anatomic regions by multi-level thresholding into several specific LACs, e.g. lung, soft tissue, and bone[18]. While this substantially reduces the noise in the transmission image, the drawback is that some tissue regions may have continuously varying densities that are not accurately represented by a discrete set of segmented values.

Simultaneous acquisition of emission and transmission image for SPECT can shorten the acquisition time and indirectly minimize the patient movement between scans. This is performed in SPECT with a lower-energy gamma source for the transmission scan (e.g. [201]Tl:75keV, [241]Am:60keV); considering these systems support acquisition of multiple energy windows, the camera can simultaneously image the primary higher-energy emission photons (e.g. 99mTc:140 keV) at the same time[19,20]. This approach, however, introduces cross-talk effects between the signals at the two spectrums. In addition, the transmission energy is not the same as the emission energy, requiring a conversion of the transmission scan attenuation values to the emission scan attenuation.

1.5 CT-BASED ATTENUATION CORRECTION FOR PET AND SPECT IMAGING

With the advent of dual-modality SPECT/CT and PET/CT imaging systems introduced in 1990's [5,8], the patient-specific LAC map now can be rapidly acquired with an integrated x-ray CT scanner. The simplified narrow-beam projection can be written as[21] :

$$p_{CT}(r,\theta) = I_0 \cdot exp - \int_0^{kV_p} \Omega(E) \int_0^D \mu(l';E)dl'dE \quad [8]$$

Where Ω represents the spectrum of the x-ray source from 0 to the peak energy (kVp). The common procedure of the CT-based attenuation correction generally is to do the CT transmission scan (30 s – 2 min) before the emission scan (5 – 45 minutes). The CT image, in Hounsfield unit, will then be down-sampled to SPECT or PET resolution and "transformed" to the LAC at emission energies. The translated image is then forward projected into the projection view for the *ACF (r, θ)*, and then the attenuation-corrected emission data, *P_corrected (r, θ)*, are reconstructed for the final

image. In addition to the order of magnitude faster acquisition, the CT-based method offers advantages over previous radionuclide transmission methods in other aspects including: a) the statistical noise in a CT image is much lower than radionuclide transmission images leading to virtually noise-free attenuation maps, b) CT acquisitions avoid the signal contamination from SPECT or PET's tracer, and c) it eliminates the cost of the periodic replacement of decayed transmission sources[8].

The poly-energetic nature of the CT energy spectrum and the "energy difference" between CT x-rays and emission sources cause additional challenges. Beam-hardening effects arise from differential absorption of lower-energy photons as the poly-energetic x-rays are transmitted through the scanning object, and causes location-dependent LAC bias in the CT image. Most CT scanners have beam-hardening correction methods that are effective for water-equivalent tissues, but these systems are generally still challenged by non-water equivalent regions such as bone and metal implants[21]. To account for the energy difference between x-ray and radionuclide tracers, the CT estimates of attenuation must be transformed to an estimate of the attenuation coefficients at the emission energy. However, there is no unique transformation from effective energies of x-ray to the emission photoenergy since to the relative contributions of photoelectric effect (τ) and Compton scattering (σ) are a function of energy (*see Figure 1-5*). In other words, two materials with similar CT values may have different attenuation coefficients at 511 keV, and conversely, it is possible for two distinct materials with the same value of attenuation coefficient at 511 keV to have different CT numbers. The bias in LAC map will cause an artifact in the final emission image and these localized errors will propagate to the same general location in the emission image.

Therefore, methods for accurately converting a CT image to attenuation coefficients at the higher energy need to be carefully considered[6,8].

Finally, we note that the (LAC) attenuation image, which are used for attenuation correction, also enable estimates of the amount and distribution of scattered coincidences. These estimates can then be used for scatter correction in PET and SPECT[12].

1.6 ATTENUATION CORRECTION FOR PET/MR IMAGING

The motivation for combining the emission image with MRI is three fold[10,22,23]; (1) For certain applications, for instance neuroimaging and abdominal imaging, MRI is the preferred anatomic imaging modality to CT because of its superior soft tissue contrast. (2) The radiation dose of PET/MR is significantly lower than it is in PET/CT, and this could be particularly important for pediatric imaging or for a patient requiring multiple consecutive scans; (3) this hybrid system can further correlate PET imaging with MR-based functional measurements, for example, dynamic contrast-enhanced MRI, diffusion-weighted MRI, functional MRI, or MR spectroscopy. The first commercially available whole-body PET/MR (Biograph mMR, Siemens AG, Healthcare Sector, Erlangen, Germany) was introduced in 2010[24]. While it has not been adopted as a routine clinical tool yet, a hybrid PET/MR system offers the potential for innovative research and clinical studies and there have been over fifty PET/MR systems installed for clinical use today [25]. The biggest challenge for integrating the MRI with emission detectors is that conventional PET or SPECT detectors can not be placed inside the MRI scanner primarily because they use photomultiplier tubes (PMT). Furthermore, the moving components (collimators and gamma cameras) of SPECT scanner could be highly susceptible to magnetic fields. MR compatible detectors such avalanche photo diodes (APD) or silicon photomultipliers (SiPM) were used for the integration of PET/MR system; however, there is still no efficient or economic solution of making a whole-body SPECT/MR[10].

Attenuation correction for PET without a CT-image or radionuclide transmission scan is another technical challenge for integrating emission imaging with MR[26,27]. Unlike the CT image, which measures the radiodensity of tissue, the MR signal correlates with the density of hydrogen nuclei and their relaxation properties. New approaches for AC based on MR (MRAC) rather than CT-based AC were required to estimate the attenuation coefficient map. To date, these approaches can be roughly categorized into three classes[22,23,26]: (1) Segmentation-based methods: segment the MR image into several classes to which uniform LACs are assigned. (2) Atlas-based methods: use a attenuation atlas templates from CT images or other knowledge and morph these onto the patient's MR image in order to obtain a continuous attenuation maps from the MR data. (3) TOF-MLAA (time-of-flight maximum likelihood activity and attenuation estimation) method: the method exploits TOF PET emission data for jointly estimating the emission activity and the attenuation coefficients.

1.6.1 *Segmentation-based method*

Segmentation methods use both MR pulse sequence and image processing techniques to segment MR image data into different tissue classes and to assign the tissue compartments with known LACs at 511keV. For example, for a whole-body PET/MR scan, segmentation can be performed on a T1-weighted gradient echo image with proper Dixon-based water-fat separation to classify the MR image into air, lung, fat, and soft tissue compartments, and respectively, assigned with the 511keV LAC values of 0, 0.015-0.03, 0.086, and 0.095 cm^{-1} [28,29]. However, a major problem with segmentation method of MRAC is the detection of bone tissue; both air and bone lack signal in MRI, but conversely, bone tissue requires the largest LAC (0.15-0.17 cm^{-1}) compared to other tissues. One approach to improve MR bone contrast is to use ultra-short echotime (UTE) sequences[30]; using fast acquisition techniques like radial (in *k*-space) imaging with nonselective or half pulse excitation, also with half-Fourier readout and ramp sampling, TE can be as short as a few microseconds. The UTE images themselves are heavily proton density-weighted, and by acquiring a second echo (milliseconds TE) and subtracted it from the UTE image, the subtracted image then highlights the short T_2 tissues as bright structures against a darker surround[27,31](*see Figure 1-6*). The UTE-based

protocols have been validated in the numerous head PET/MR imaging studies[23] but not for the whole-body PET/MR. One current challenge with whole-body UTE MR is that it requires either a smaller FOV or a longer scan time (several minutes per bed position) that may cause a motion artifact that further reduces the accuracy of MRAC[23]. Until a more efficient bone-contrast enhanced MR sequence is developed, the following atlas-based MRAC seems a more applicable method for whole-body PET/MR acquisition for accurate bone imaging. To estimate LACs in lung is also a challenge for segmentation methods; Not only because the LACs of lung varies between patients, but also since visualizing lung parenchyma with MRI is challenging[32]. Studies have shown the relative error of uptake value in PET could be reduced from 12% to less than 5% by using a patient-specific lung LAC map instead of assigning a globally constant coefficient[32].
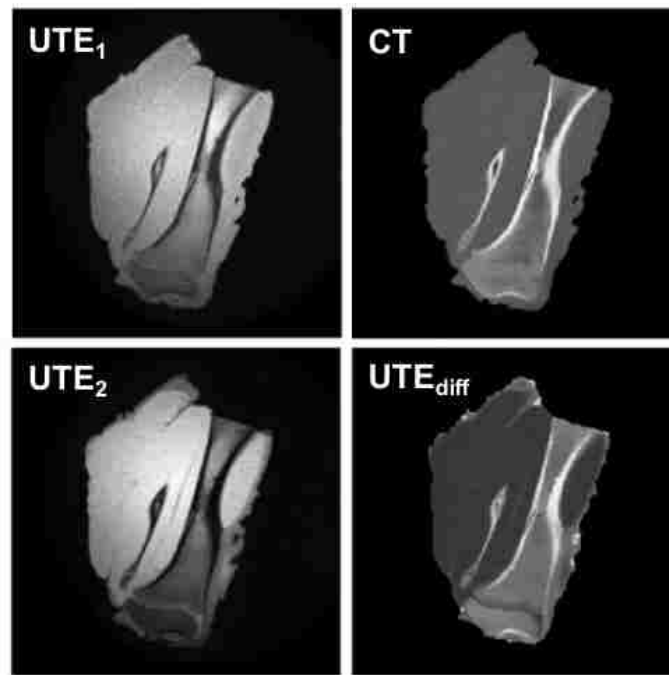
Figure 1-6. MR ultra-short echo time (UTE) acquisitions for showing the cortical bone image on a porcine shank phantom

UTE$_1$ being acquired during the free induction decay (FID) at time TE$_1$, and UTE$_2$ acquired at the first echo at time TE$_2$. UTE$_{diff}$ is relative difference image between two acquisitions, and it shows contrast of cortical bone similar tow the CT image.

1.6.2 *Atlas-based method*

Most atlas-based methods first build an "averaged" atlas from a repository of CT images with known HU values. Then for a given patient exam, the atlas image is morphed to the patient MR based on their shared anatomical features   through standard image registration, machine learning, or pattern recognition techniques[7,33,34](*see Figure 1-7*). With atlas based methods one can retrospectively add bone information to a continuous scale LAC map with or without time-consuming UTE acquisitions. A weakness of this approach is that the LAC map registration process can be computationally intensive. And, when a patient has a unique morphology, pathology, or implants that are substantial anatomically different from the atlas, the morphed attenuation map will not represent the patient's attenuation leading to bias in the emission image[22].
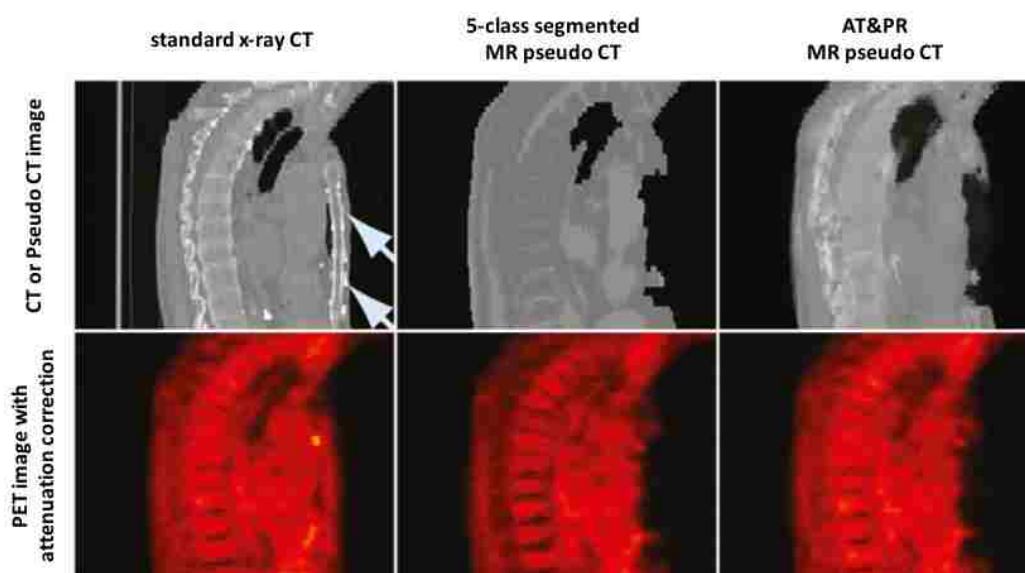
Figure 1-7. Image comparison of two MR-based pseudo-CTAC methods

CT or Pseudo CT images were shown in the top row, and its corresponding PET images with attenuation correction were shown in the bottom row. In x-ray CT image, arrows indicate the position of metal implant. 5 classes in the segmentation method are air, lungs, fat tissue fat-nonfat tissue mixture, and non-fat tissue.

1.6.3 *MLAA-based method*

The time-of-flight maximum likelihood activity and attenuation estimation (MLAA) approach uses only the emission data to jointly estimate the activity distribution and attenuation of the PET image with a maximum likelihood reconstruction method [35]. Based on the ideal Radon consistency conditions that noise-free coincidence PET data after accurate attenuation correction can only come from a certain set location, in theory, the tracer's activity and the attenuation coefficient can be derived at the same time solely using the emission data. However, the uncertainty of crosstalk between activity and attenuation effectly limits its application in practice. With advent of TOF PET, the activity distribution now can be constrained down to the sub-nanosecond (few centimeters) resolution; the TOF information adds another constraint enabling the attenuation map so that it can be more accurately determined [36,37]. Recently, additions to MLAA have been proposed that further constrain the estimation by exploiting the edge of whole-body PET/MR images with (or without) using the segmented MR image as priori knowledge[38-42]. Research groups continue to develop this approach and some combination of this method with methods discussed above will likely provide a viable technique for high fidelity MRAC for soft tissue and the challenging areas of bone and lung regions.

1.7 GENERATING CTAC MAP FOR PET IMAGING

Multi-linear scaling approaches are the basis for common CT attenuation correction methods currently in use in conventional PET and SPECT scanner. Since the attenuation values (in Hounsfield units) produced by CT are approximately linearly related to the physical LAC of the correspondent tissue type in emission energy, it is possible to simply multiply the entire CT image by the ratio of LAC of water (soft tissue) at the photon energy of CT and emission image[43]. However, this simple linear model will be inaccurate for the high Z absorbers like bone, since the photoelectric absorption to Compton scattering ratio changes differently for bone compared to the

soft tissue (*Fig. 5*). Therefore, bilinear models that separately depicted the LAC conversion ratio for air-and-water rich tissue (-1000≤H≤0) and water-and-bone rich tissue (H≥0, CT energy dependent) for both PET and SPECT imaging were proposed[5,8,21,44-46]: where $CT_{H.U.}$ means the value of CT number in the Hounsfield unit. μ with the subscript "E" represents the target translated emission energy, while "keV$_{eff}$" represents the effective x-ray photoenergy.

$$\mu_{air+water,E} = \frac{CT_{H.U.} \cdot \{\mu_{water,E} - \mu_{air,E}\}}{1000} \qquad [9a]$$

$$\mu_{water+bone,E} = \mu_{water,E} + \frac{CT_{H.U.} \cdot \mu_{water,keV_{eff}} \cdot \{\mu_{bone,E} - \mu_{water,E}\}}{1000 \cdot \{\mu_{bone,keV_{eff}} - \mu_{water,keV_{eff}}\}} \qquad [9b]$$

Furthermore, taking into consideration that the LAC of cortical bone tissue (~ 3000 HU) may be overestimated comparing to the cancellous bone tissue (~ 700 HU), a three-line model was suggested to more precisely convert the high CT number (H > 1000)[47,48](*see Figure 1-8*).
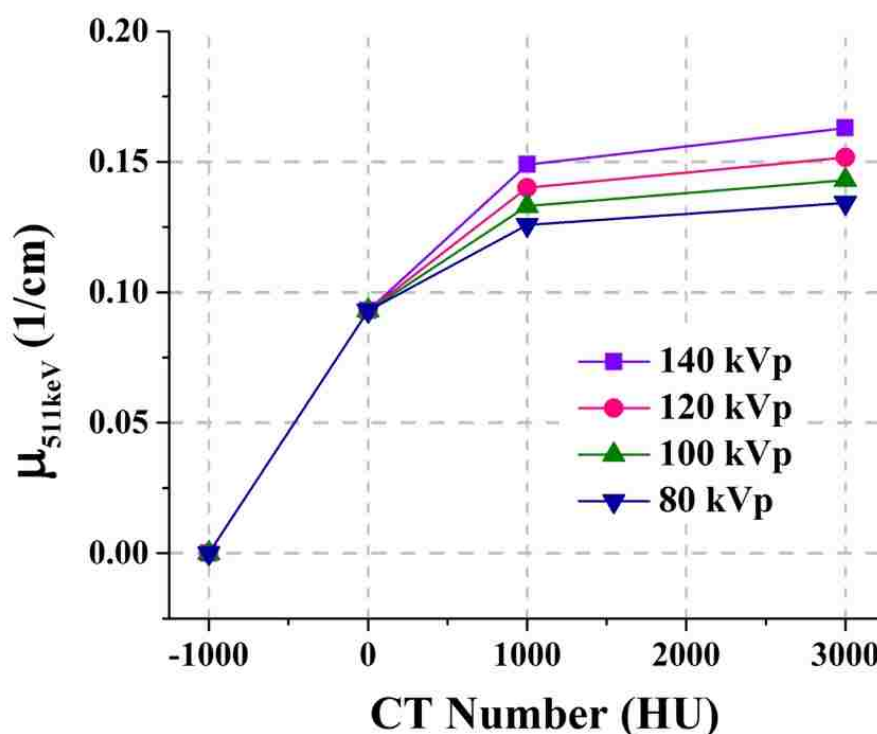
Figure 1-8. Three-line model scaling method used to convert CT numbers to linear attenuation coefficient at 511 keV for different x-ray tube potentials[47]

Dual-energy CT is a more accurate approach to convert CT images to LAC at emission energy. It can be achieved by collecting two scans generated with different peak energy (kVp)[5,49-51]. In practice, the multilinear scaling methods mentioned above have been shown to give reasonable results for low-Z biological materials. However, high-Z materials, such as contrast agents and implants, can introduce significant bias. Therefore, with the idea that the mass attenuation coefficient can be considered the composition of attenuation due to the photoelectric effect (τ) and the attenuation due to the Compton scatter (σ) effect (*eq.[3]*). The DECT approach can be understood by measuring the linear attenuation coefficient (μ_m) within both low and high (E_L, E_H) tube voltage as a weighted (α_τ, α_σ) sum of known photoelectric absorption (τ) and Compton scattering (σ) contribution at each energy[21]:

$$\mu_m(E_L) = \alpha_\tau \tau(E_L) + \alpha_\sigma \sigma(E_L) \quad [10a]$$

$$\mu_m(E_H) = \alpha_\tau \tau(E_H) + \alpha_\sigma \sigma(E_H) \quad [10b]$$

This simple system of equations includes two measurements ($\mu_m(E)$) and two unknowns (α_*). One can solve for α_τ and α_σ so that the mass attenuation coefficient can be converted to any emission energy with proper τ (E) and σ (E) constants. Several approaches have been proposed to acquire the dual energy measurements and to solve for the weights[52]. A potential disadvantage of this approach is that the solutions for the weights require essentially a generalized subtraction of the two separate CT scans. The noise in each scan will propagate into the weight images leading to noisier images than the original. Therefore, although dual-energy techniques theoretically offer the highest degree of accuracy, they also can have degraded SNR characteristics in comparison with attenuation maps calculated from a single CT scan. Another potential drawback of dual energy is the additional patient radiation dose required to acquire two separate energies[6,53].

1.8 CHALLENGES FOR CT-BASED ATTENUATION CORRECTION

1.8.1 *Motion compensation*

Misalignment of the emission data and the attenuation correction factors due to patient movement, cardiac contraction, and respiratory motion are known sources of quantitative error in radionuclide imaging[54,55](*see Figure 1-9*). One basic solution to minimize gross patient movement is to give the patient some physical aids like arm or head holding devices to limit the movement [56]. Other approaches such as automatic or semi-automatic registration can be used for correcting misaligned images due to the patient movements, although all practical implementations are generally only effective at fixing rigid-body misalignments[55].

Considering PET and SPECT imaging is acquired over multiple respiratory and cardiac cycles and CT imaging is often acquired at essentially one or two locations in these cycles, there are commonly challenges

in aligning the CT-derived attenuation map[57-60]. For applications of myocardial perfusion and lung imaging, to improve AC, electrocardiogram (ECG)-gating and respiratory-gating techniques can be applied on both the emission and anatomical scans[59]. In theory, phase or displacement matching individual PET or SPECT gated images with the corresponding gated CT images for attenuation correction could effectively minimize attenuation misalignment.

Numerous methods have been developed for improving the overall accuracy of 4D-CTAC. Phase-based sorting methods are often the default method for 4D-gated acquisition due to their implementation simplicity. It has been shown that amplitude-based[61-63] and anatomical similarity-based realignment[64,65] methods potentially provide higher accuracy than phase sorting, particularly for non-periodic motion with high inter-phase variations. Another approach to improve gating is to optimize the tradeoff between gating number and the emission image noise.

In brief, finer temporal binning size generally provides better tracking of motion at the expense of increased noise and methods that optimize this tradeoff are advantageous[66,67]. Considering that gated CT imaging (and gated emission imaging) can have native artifacts from poor respiratory signal measurement or in the presence of high respiratory variation, studies have shown that 4D phase-matched CTAC methods may cause more bias on the corresponding PET image than CTAC with less artifact-prone images such as phase-averaged or phase-maximum intensity projected (MIP) methods[68,69]. In the presence of phase-to-phase motion variability, the average of extended cine duration CT acquisitions, across numerous cycles at each bed position from 6s to 10~14s, may be able to mitigate AC motion artifacts[69,70]. While CT can only be acquired sequentially either before or after the emission scan, some integrated PET/MR systems offer the potential for acquiring the anatomical image simultaneously with the emission image, minimizing or eliminating attenuation map misalignment issues[71].
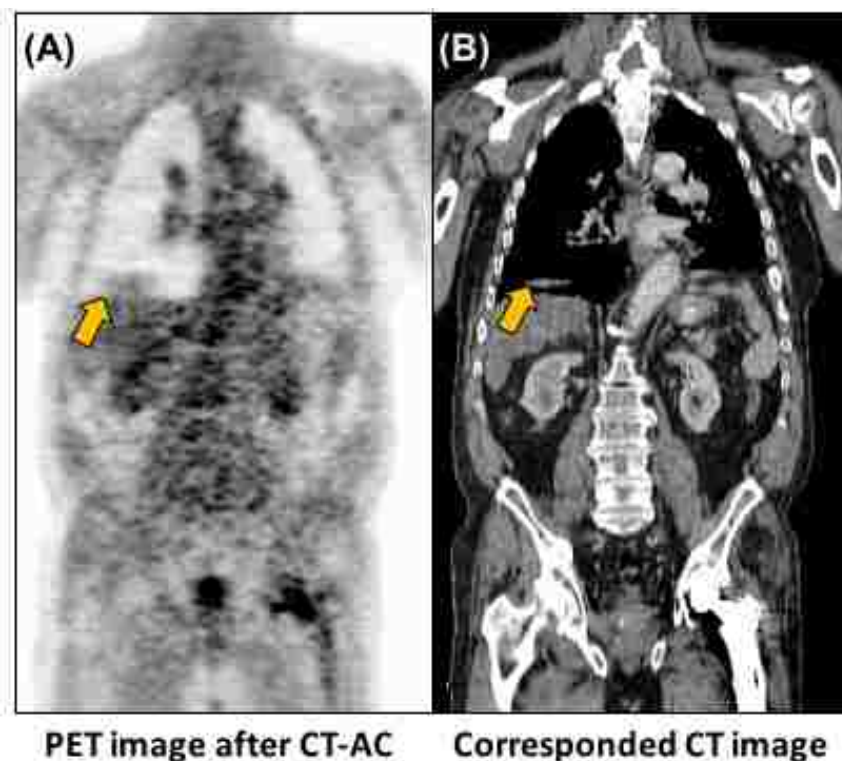
Figure 1-9. Respiratory motion artifact of CTAC

(A) A suspicious tracer uptake/artifact at the base of lung area (arrow) in the PET image. (B) PET uptake is actually due to respiratory motion artifact in the CT image (arrow).

1.8.2 *Non-biological materials*

The multi-linear scaling methods for converting CT numbers to the LAC's at emission energies generally work well for soft tissue and bone regions. However, CT contrast agents like iodine have a high LAC for CT photon energies but for 511keV photons the LAC is very similar to other soft tissues. When contrast agents are present, the existing conversion factors may overestimate the emission LAC for iodine and cause the bias for the final activity uptake[50]. Initial studies indicated that these contrast errors are likely not significant for diagnosis in a variety of cases[72], but these AC errors will cause quantitative issues that will impact treatment evaluation and further treatment planning[50]. A simple solution that is available on several commercial systems is to use a different

set of conversion factors when CT contrast is present. This will effectively lead to more accuracy in contrast present regions at the expense of reduced accuracy in other high-CT number regions (i.e., bone regions). Metallic objects, such as implanted pacemaker or dental fillings, also complicate the use of CT-based attenuation correction[73,74](*see Figure 1-10*). A general approach for metal artifact reduction is to use a threshold method to segment out the high CT number regions on the raw sinogram or reconstructed image. After segmentation, a following algorithm can be used for regenerating the missing voxels [74,75]. DECT is another approach for getting accurate emission attenuation information in the face of non-biologic media[50,51,76] (*see Figure 1-11*); as described in the previous section, the mass attenuation coefficients from photoelectric effect and Compton scattering of the absorber can be decoupled and rescaled to the target emission energy. In consideration of increasing image noise and radiation dose of the DECT-AC process, several approaches have been proposed such as: to use a very-low-dose scan as a second CT image, to alternate x-ray energies on alternating slices in a single CT scan, or to suppress the signal noise with sinogram smoothing [51,53,76].
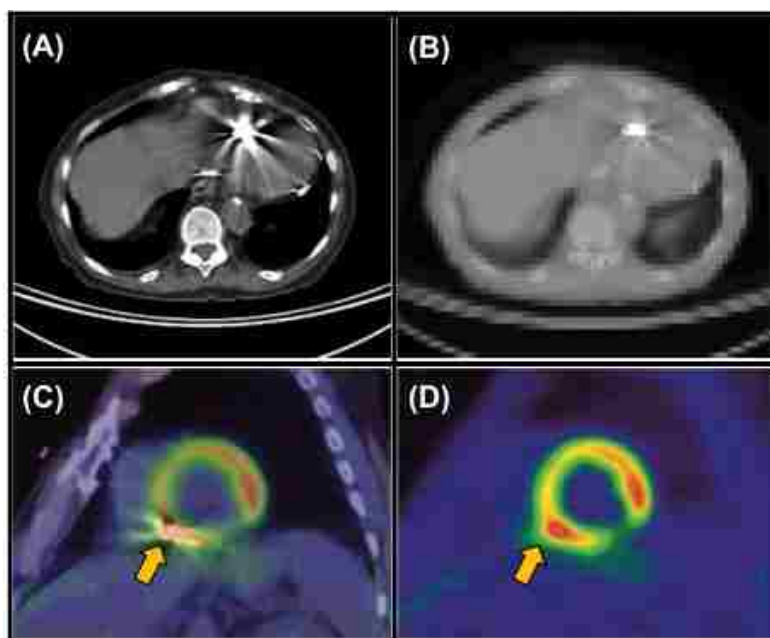
Figure 1-10. Representative CT and PET images illustrating artifacts from implanted pacemaker/implantable cardioverter defibrillator (ICD)[73]

(A) Original CT image. (B) Down-sampled CT image for PET attenuation correction. (C) Fused PET/CT and (D) PET images using (CT) for attenuation correction, showing the biases in attenuation corrected PET uptake image due to implant (arrows).
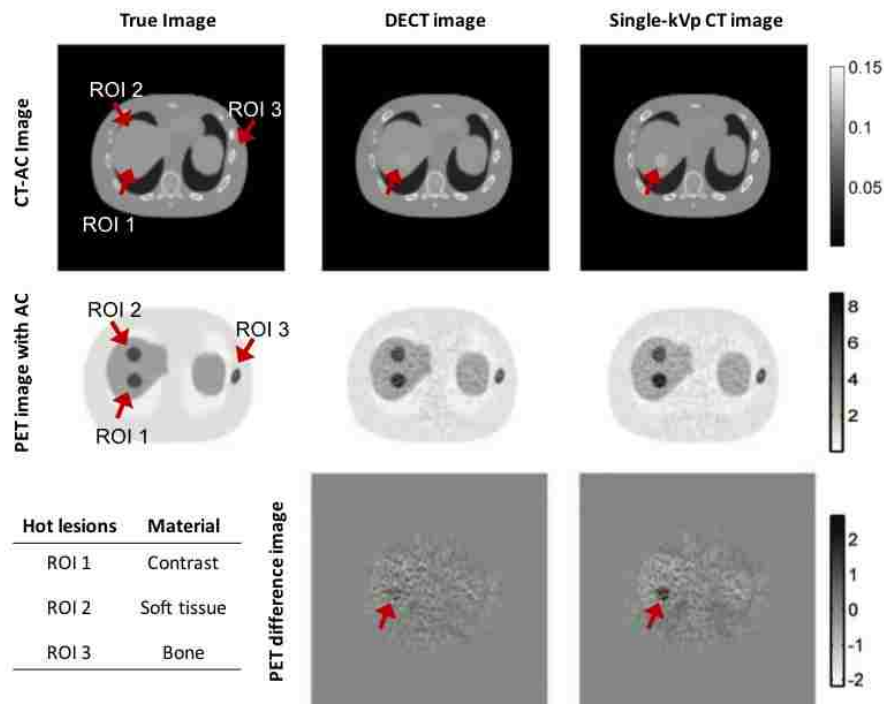
Figure 1-11. Comparison of PET images using simulated DECT-based and single-kVp CT-based AC methods[76]

The DECT-AC caused less bias for PET uptakes in ROI1 (contrast agent) compared to the uptake bias from single-keV CT-AC method (arrows in the third row).

1.8.3 *Truncation of the imaging field of view (FOV)*

Current CT fields of view (FOV) in commercial PET/CT systems are usually slightly smaller than it is for the emission image. Therefore, PET images may find no corresponding CT information when a large patient is in the bore or a patient is imaged with their arms at their side. This lack of attenuation information at the edge of the PET FOV can lead to a FOV truncation artifact. Several techniques have been proposed to correct this [77,78]. Most of the approaches use an extrapolation-based algorithm to estimate the missing CT data based on the assumption that the total attenuation for each projection view should be a constant value[79].

1.9 APPROACHES FOR ULTRA-LOW DOSE IMAGING

In recent years, the radiation dose from CT scanning is a growing concern in both the medical community and the public. It is widely accepted that additional vigilance is required to ensure appropriate CT usage leading to numerous efforts to reduce CT radiation burden, both for the pediatric and adult populations[80-82]. If generating an AC map is the sole purpose for the CT acquisition, the dose levels can be reduced substantially below conventional acquisitions for diagnostic or anatomical localization. In 2002, Kamel *et al.* showed that there was no significant difference in terms of apparent FDG uptake or measured lesion size in PET when the tube current was lowered from 120mA to 10mA in 18 patients[83]. Today a standard PET/CT exam with a low-dose CT for attenuation correction (e.g. 120kVp, 35 mAs ,pitch = 1) imparts a whole body effective dose of approximately 12 mSv (7 mSv from injection of 10mCi 18F-FDG[84] and 5 mSv from the CT scan)[85-87]. Several approaches or combinations of approaches have been purposed to achieve ultra-low dose (sub-mSv) CT scans for attenuation correction. Some of these methods include the following. Optimizing the beam energy spectrum with the proper kVp and filtration combination along with pre-log sinogram smoothing methods like adaptive trimmed mean filter (ATMF) have been shown effective in the recent studies[88-90]. Methods proposing tube-pulsing to enable ultra low-dose CT acquisitions with fewer views but with the same number of total photons (or integrated signal) such that the effect of the electronic noise can be reduced[91]. After acquisition, images can be reconstructed from the reduced view data with compressed sensing-type methods[92]. At very low flux levels, the CT signal can suffer from extremely high noise measurements and photon starvation. In this regime, iterative reconstruction methods that more accurately model low-flux signal statistics have been applied for achieving better image quality[93]. In the future, methods

that incorporate even better descriptions of photon statistics, like the compound-Poisson model or

pre-log reconstruction algorithms, may allow for even lower dose CT for AC[94,95].

Chapter 2. IMPACT OF CTAC METHOD ON QUANTITATIVE REPIRATORY-GATED PET/CT IMAGING

2.1 MISALIGNMENT BETWEEN PET AND CT UNDER THE RESPIRATORY MOTION

Positron emission tomography (PET) with ^{18}F-fluorodeoxyglucose (FDG) is commonly used in the management of patients with lung cancer and is of considerable interest in quantitative imaging of the thorax. The addition of PET imaging is useful in staging of atelectasis and the mediastinal nodes[96-98]. The use of PET-guided segmentation may reduce inter-observer variability compared to CT-only guided segmentation and provide clinical benefit for radiotherapy target definition[99-101]. FDG metrics have been shown to predict therapeutic outcome early in the course of chemo-radiotherapy in non-small cell lung cancer. Dose escalation to metabolically active tumor sub-volumes, so-called "dose painting", has been proposed as a strategy to increase tumor control[102,103].

Mismatch of PET data with computed tomography attenuation correction (CTAC) due to respiratory motion in a known source of quantitative error in PET imaging[6,104-106]. In theory, this can be corrected by matching individual PET and CT phases which have been generated by respiratory-correlated PET (4DPET)[107] and respiratory-correlated CT (4DCT)[108-111]. However, differences in the physics of image acquisition between PET and fast CT imaging lead to challenges for this approach. Namely, emission PET integrates motion over several minutes with large (i.e., 15 cm) axial fields-of-view, while fast helical or axial transmission CT has the effect of "freezing" motion over several seconds with smaller (i.e., 2 cm) axial fields-of-view. In practice, both imaging modalities are known to be susceptible to respiratory imaging artifacts. Therefore, it

is important to understand the quantitative impact of CTAC methods for respiratory-correlated PET imaging.

2.2 A PHANTOM STUDY FOR COMPARING DIFFERENT CTAC METHOD FOR 4-D PET/CT

A small body of prior work exists regarding choice of CTAC method for 4DPET quantification in the ground truth setting with anthropomorphic phantoms. Nagel *et al* found 4DPET with phase-matched 4DCT attenuation correction was superior to 3DPET with helical CT attenuation correction under sinusoidal respiratory motion[112]. Ponisch *et al* and Park *et al* investigated 4DPET with phase-matched 4DCTAC and 4DPET with helical CTAC under sinusoidal motion and found superior recovery with phase-matched 4DCTAC[113,114]. Killoran *et al* investigated artifacts at the lung-diaphragm interface with helical CTAC, phase-averaged 4DCT, and phase-matched 4DCT attenuation correction under sinusoidal motion[115]. They noted minor improvements in quantification with phase-matched 4DCTAC versus phase-averaged 4DCTAC or helical CTAC in regions with lung-equivalent background density, but no advantage to using phase-matched 4DCTAC at interfaces of similar tissue density.

We present new work to comprehensively evaluate the accuracy of six CTAC methods for 4DPET imaging using measured data from a respiratory phantom. We report on 4DCT maximum intensity projection (4DMIP) attenuation correction, which has shown advantages in accuracy of cardiac PET[116] but has not been previously investigated in thoracic PET. While prior phantom studies considered only sinusoidal motion cases, we investigate patient-specific respiratory waveforms, which more accurately represent clinical conditions and may be expected to increase CT and PET mismatch due to irregular respiratory patterns. Additionally, we report on the recovery of metrics

not previously investigated, including SUV_{peak}, which is recommended over SUV_{max} by PERCIST guidelines[117], and SUV_{mean}, which is commonly used in the literature. Finally, comparisons of accuracy between 3D and 4D PET are evaluated in context of CTAC method. These results may be useful to guide the implementation, analysis, and development of respiratory-correlated thoracic PET/CT in the radiation oncology and diagnostic settings.

2.3 METHODS

2.3.1 *Phantom design*

A programmable respiratory motion phantom consisting of the Quasar™ Multipurpose Torso Phantom and Respiratory Motion Assembly (Modus Medical Devices Inc., ON, Canada) was used for this study (*see Figure 2-1*). A custom movable insert was designed to emulate a lung lesion (2.2 cm fillable NEMA sphere) and lung tissue (fillable chamber with polystyrene beads to mimic lung tissue density). A static control insert was similarly designed with a 3.7 cm NEMA sphere and fillable chamber with polystyrene beads. Phantom spheres and lung-equivalent backgrounds were filled with ^{18}F-FDG solutions at nominal activity concentrations of 1.0 and 0.125 MBq/ml, respectively.

The moving insert was driven by one of 5 waveforms: two sinusoidal waveforms or three patient-specific respiratory waveforms. The sinusoidal waveforms had 1.5 cm and 3.0 cm peak-to-peak amplitude and 4 s period. The patient-specific waveforms were supplied by the vendor and had the following parameters as depicted in Figure 2-1: 3.0 cm peak-to-peak amplitude; mean amplitude 1.86±0.27, 2.00±0.42, and 2.16±0.31 cm; mean period 4.2±0.7, 4.5±0.7, 4.9±0.7 sec, respectively. The Quasar phantom drives a platform which is suitable for mounting a real-time position

management (RPM) marker (Varian Medical Systems, Palo Alto, CA), which moves proportionally to the insert.
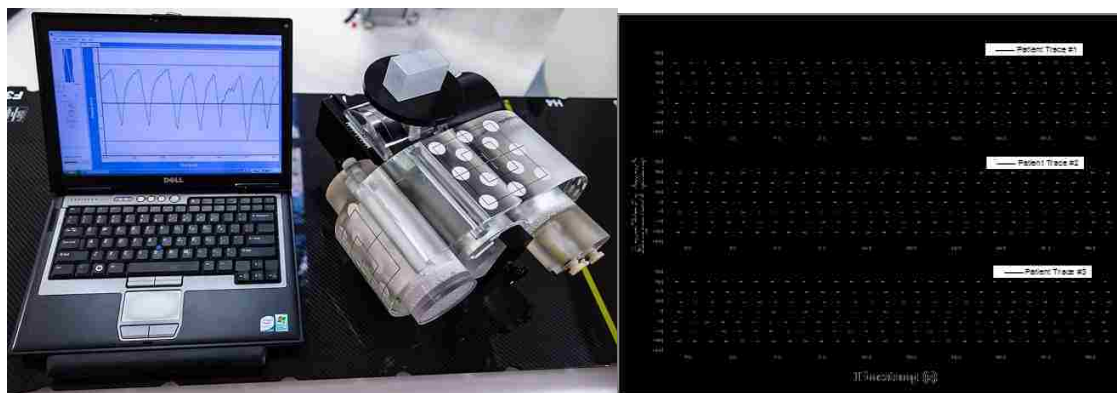
Figure 2-1. Respiratory phantom and patient-specific respiratory waveforms

Left: Programmable respiratory phantom with custom anthropomorphic PET inserts. Right: Patient-specific respiratory waveforms under investigation, representing regular, irregular, and intermediate respiratory waveforms. Two sinusoidal waveforms were also investigated.

2.3.2   *Image acquisition and reconstruction*

PET/CT images were acquired on a Discovery STE PET/CT scanner (GE Healthcare, Waukesha, WI) at a single 15 cm axial field of view in 3D mode. PET emission data were acquired for 5 minutes under the no-motion condition to define the reference case. Then, PET data were acquired under the 5 motion conditions with matched numbers of emission coincidence counts to the reference case (261.5 million events; typical whole-body FDG fully 3D PET acquisitions acquire 200-300 million prompt events for each bed position). Phantom motion waveforms were captured in real-time with the RPM infrared camera system and PET emission data were in-line tagged at peak inspiration during list mode acquisition to enable 4D data sorting.
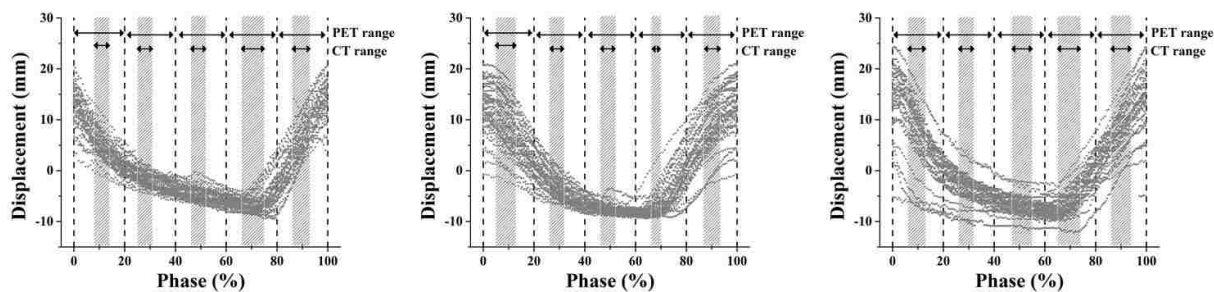
Figure 2-2. Schematic representation of 4DPET and 4DCT phase range versus phantom displacement for each of the patient-specific respiratory waveforms.

Phase range for the 4DCT is depicted with the grey shading and centered within PET bins. Phase range for the 4DPET is depicted with vertical dashed lines.

Following PET acquisition, CT images were acquired. A static helical CT (3DHEL) analogous to an idealized breath-hold CT was used as the reference CTAC dataset. Then, CT images were acquired for each respiratory waveform, including a helical CT under respiratory motion (3DMOT) analogous to a free-breathing CT and a cine CT series for 4DCT reconstruction. For 4DCT acquisitions, the cine duration parameter was defined as the breathing period plus 1 second and the time between cine images parameter was defined as the respiratory period in seconds divided by 10. All CT imaging was acquired with 512x512x176 voxels, 0.0977x0.0977x0.25 cm/voxel at 120 kV and auto mAs.

For 4DCT reconstruction, RPM traces were visually reviewed for accuracy of peak fitting retrospectively in the RPM software. RPM traces were used to phase-define the cine CT data in Advantage 4D (GE Healthcare). Five 4DCT phase-defined images were selected with 10% phase shift for phase-matched CTAC reconstruction (4DMATCH) so that 4DCT phases would be centered on 4DPET phases in the respiratory cycle (*see Figure 2-2*). Additionally, 4DCT phase-

binned images were reformatted into average intensity projection (4DAVG) and maximum intensity projection (4DMIP) CT images, and the 4DCT phase image that corresponded to the end-exhale phase was identified as 4DEXH. The protocols are summarized in Table 2-1.

Table 2-1. Summary of investigated PET and CTAC methods.

PET	PET acquired under motion?	CTAC	CTAC acquired under motion?	Description
3DPET	No	3DHEL	No	Motion-free 3DPET with motion-free helical CTAC (reference case)
3DPET	Yes	3DHEL	No	3DPET with motion-free helical CTAC (representing idealized breath hold)
3DPET	Yes	3DMOT	Yes	3DPET with helical CTAC (representing free breathing helical CT)
3DPET	Yes	4DAVG	Yes	3DPET with average intensity projection 4DCTAC
3DPET	Yes	4DMIP	Yes	3DPET with maximum intensity projection 4DCTAC
4DPET	Yes	3DHEL	No	4DPET with motion-free helical CTAC (representing idealized breath hold)
4DPET	Yes	3DMOT	Yes	4DPET with helical CTAC (representing free-breathing helical CT)
4DPET	Yes	4DAVG	Yes	4DPET with average intensity projection 4DCTAC
4DPET	Yes	4DMIP	Yes	4DPET with maximum intensity projection 4DCTAC
4DPET	Yes	4DMATCH	Yes	4DPET with phase-matched 4DCTAC
4DPET	Yes	4DEXH	Yes	End-exhale phase 4DPET with end-exhale phase 4DCTAC

CT data were then transferred from the Advantage workstation to the PET/CT console for attenuation correction of PET data. The static PET with static helical CTAC was used to define the reference case. For the five motion cases, all PET data was reconstructed in both 3D mode, and 4D mode with 5 equal phase bins unlisted from the tagged emission data (*see Figure 2-2*). The choice of 5 phase bins was based on Park *et al*, who found 5 bins to provide superior image quantification versus 10 or 20 bins[114], in addition to the clinical practicality of this approach. CT attenuation correction was applied to both the 3D and to each phase of the 4D PET data with 3DHEL, 3DMOT, 4DAVG, 4DMIP, and 4DMATCH CTAC methods, and to the end-exhale phase of the 4DPET data with 4DEXH (*see Figure 2-3*). For the 4DMATCH reconstruction, visual inspection of image phases was required to assure optimal matching between 4DPET and 4DCT images (ie, PET bin 1 might best match the CT bin located between 10-30% phase or 90-10%

phase). Note that in our naming convention, 3DPET refers to non-respiratory-correlated PET in 3D mode, 4DPET refers to respiratory-correlated PET, 3DCT refers to non-respiratory-correlated helical CT, and 4DCT refers to respiratory-correlated cine CT.

In total, 24 3DPET and 125 4DPET images were reconstructed over all motion cases. All PET images were reconstructed with an ordered-subsets-expectation-maximization (OSEM) algorithm (4 iterations, 28 subsets) using 128x128x47 voxels, 0.547x0.547x0.327 cm/voxel, 0.8 cm full-width at half-maximum filtration, and standard Z filtering.
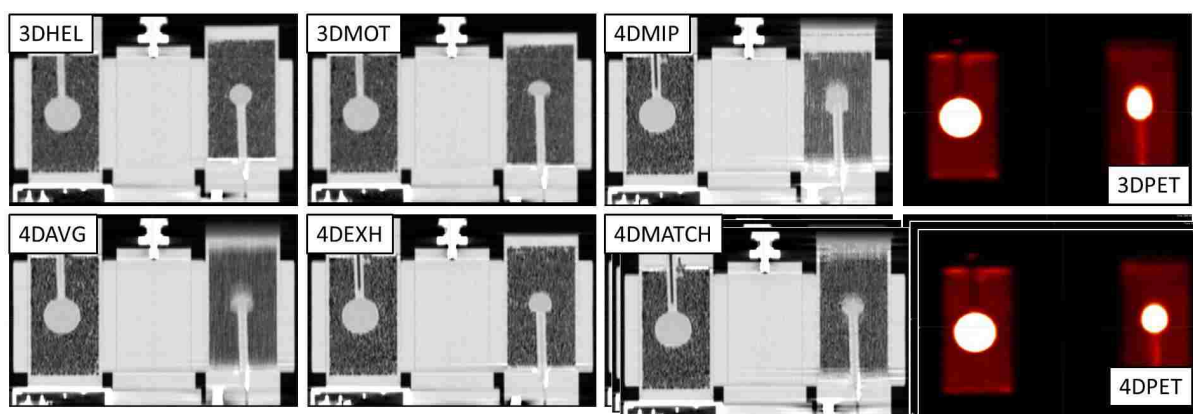
Figure 2-3. Examples all CTAC and PET acquisitions for a typical patient-specific respiratory waveform

3DHEL: Static helical "breath hold" CTAC. 3DMOT: Helical "free breathing" CTAC under motion. 4DMIP: 4D maximum intensity projection CTAC. 4DAVG: 4D average intensity projection CTAC. 4DEXH: 4D end-exhale phase CTAC. 4DMATCH: 4D phase-matched CTAC (1 of 5 phases shown). 3D PET: Non-respiratory-correlated PET. 4D PET: respiratory correlated PET (1 of 5 phases shown)

2.3.3   *Image analysis*

Quantitative accuracy was evaluated with ratios between the motion case and the reference case for the following metrics: SUV_{max}, SUV_{peak}, SUV_{mean}, and fixed threshold volume segmentation.

Two reference methods were defined. In reference method I, activity of the 2.2 cm sphere under respiratory motion was compared to the activity measured from the 2.2 cm sphere in the static reference scan. For method II, activity of the 2.2 cm sphere under respiratory motion was normalized to the activity of the static 3.7 cm sphere in the same scan. Results reported are for method I unless otherwise indicated.

Activity and volume recovery coefficients, defined as the ratio of uptake or segmented volume between the moving sphere and the reference sphere, were calculated. Change in recovery coefficients of maximum, mean, and peak activity and segmented volume were defined as RC_{max}, RC_{peak}, RC_{mean}, and RC_{vol}; for example, RC_{max} was defined as the ratio of the voxel with maximum activity in the moving sphere divided by the voxel with maximum activity in the reference sphere minus 1. The lesion volume of interest was formed by threshold segmentation (*see Figure 2-4*). The segmentation threshold was defined on the no-motion reference PET image to correspond to the internal volume of the 2.2 cm diameter sphere. The threshold corresponded to 45.5% of maximum activity (320 kBq/mL). To test the impact of threshold choice on segmentation results, threshold segmentation with 10% change in magnitude to 40.5% and 49.5% was also investigated, which is in line with prior phantom studies. The segmentation thresholds were subsequently applied to the cases under motion following decay correction. RC_{peak} was defined as the ratio of the mean activity of a 1 cm diameter sphere that is placed such that it encompasses the greatest integral activity in the respective images. RC_{mean} was defined as the ratio of mean uptake in the threshold segmentation volumes defined above. For 4DPET analysis, recovery coefficients were averaged across all phase bins unless explicitly noted.
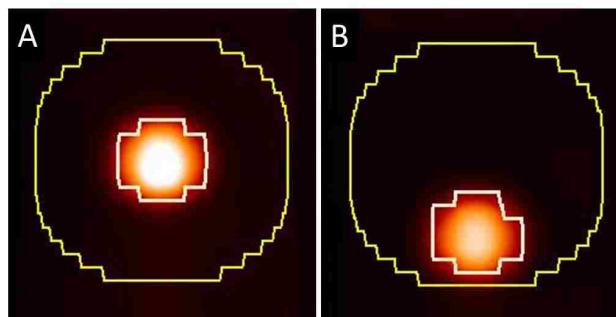
Figure 2-4. Segmented volumes of interest in the reference case of no motion and the case of 3.0 cm sinusoidal motion

The reference volume (left inner contour) was defined by taking the percent threshold segmentation that yielded the known object volume on the reference PET/CT. Then, the same percent threshold segmentation was applied to the object under motion (right inner contour). To investigate the effects of CTAC in the vicinity of the lesion, a 2 cm isotropic expansion was applied to the reference case (left outer contour) and the same contour was used for all motion cases (right outer contour).

To investigate effects of CTAC on the warm background region surrounding the lesion, a 2-cm isotropic expansion was performed around the reference segmentation volume on the static scan. Then, the segmented lesion volume on each scan was subtracted from this expansion to form a background volume of interest for each scan (*see Figure 2-4*). Ratios of activity between the motion case and the static reference case were evaluated.

Image analysis was done in MIM v.6.2.5 (MIM Software Inc., Cleveland, OH). To ensure robustness against non-normal distributions, statistical testing was performed with non-parametric paired Wilcoxon tests. To correct for the effect of multiple sampling with repeated hypothesis testing, Bonferroni's correction was applied such that the threshold of significance was set at

α=0.002. To evaluate trends across multiple variables, non-parametric Kruskal-Wallis ANOVA was used.

2.4 RESULTS

Recovery of maximum, mean, and peak activity and segmented volume are shown as RC_{max}, RC_{peak}, RC_{mean}, and RC_{vol} in Table 2-2 and
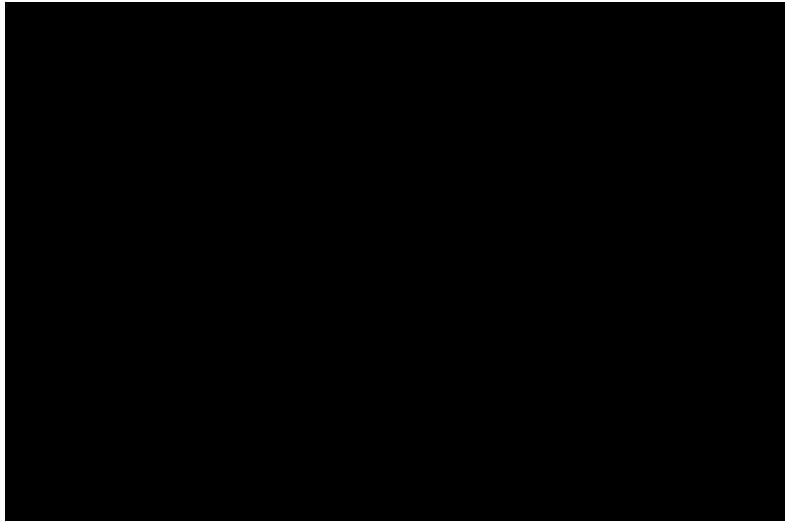
Table 2-3. for patient-specific and sinusoidal motion, respectively. Perfect recovery of activity under motion relative to the reference case would result in percent difference of zero. Box plots of recovery for 4DPET results as a function of CTAC method and image metric are shown in Figure 2-5.

2.4.1 *3D vs 4D PET*

Activity and volume recovery was improved through the use of phase-binned (4D) PET versus non-binned (3D) PET, especially for cases with large motion. In the worst case of the 3.0 cm peak-to-peak sinusoidal waveform with the helical CTAC under motion (3DMOT), errors on the order of 40-50% were observed (-40.8%, -41.9%, -23.2%, -52.1% for RC_{max}, RC_{peak}, RC_{mean}, and RC_{vol}, respectively). The best results for 3DPET reconstruction of the 3.0 cm peak-to-peak sinusoidal

waveform were obtained with the 4D maximum intensity projection (4DMIP) CTAC, but errors on the order of 30-40% persisted (-33.5%, -34.5%, -17.1%, -40.9%). For the 4DPET reconstruction, errors were reduced to 10-15% for the 3DMOT CTAC case (-9.0±3.0%, -11.2±3.7%, -8.1±2.8%, -13.5±2.7%) and to less than 5% for the 4DMIP CTAC case (2.3±2.3%, -0.3±4.2%, -2.3±3.9%, 3.1±3.0%). Smaller differences were measured between 3D and 4D PET under patient-specific motion and the 1.5 cm sinusoidal motion, on the order of 10% and 5%

respectively (*see Table 2-2*
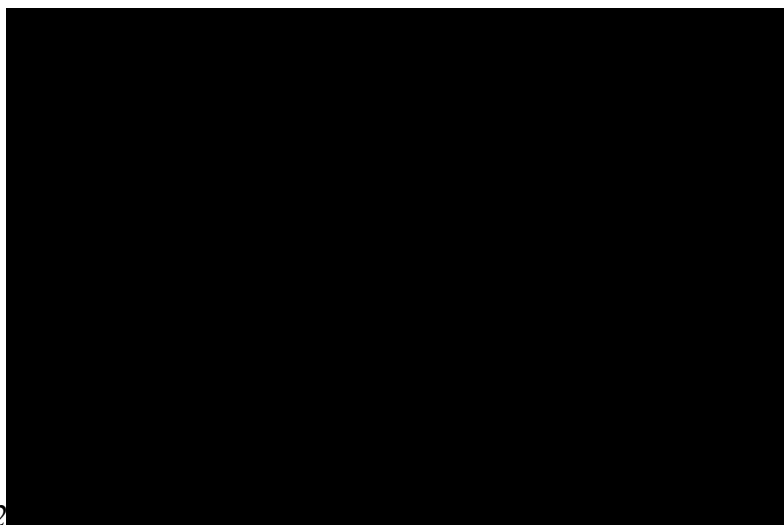
Table 2-3).

Table 2-2. Percent difference of recovery of SUV and volume metrics as a function of PET reconstruction and CTAC under patient-specific respiratory motion versus the no-motion reference

case (recovery coefficients and standard deviations are calculated across waveforms and image phases).
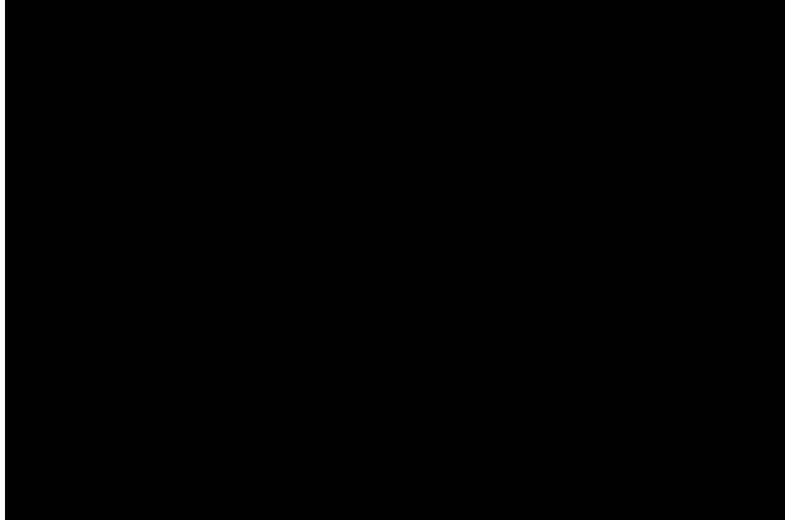
Table 2-3. Percent difference of recovery of SUV and volume metrics as a function of PET reconstruction and CTAC under sinusoidal respiratory motion versus the no-motion reference case (recovery coefficients and standard deviations are calculated across image phases).
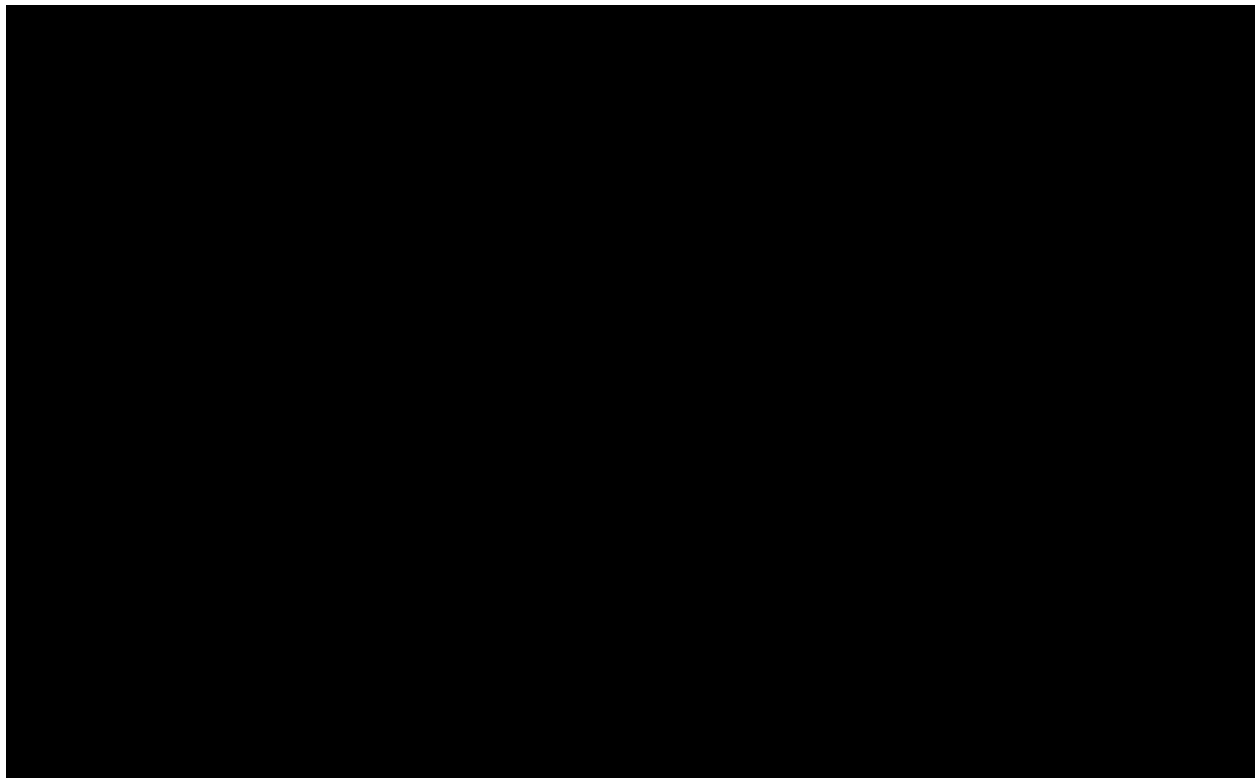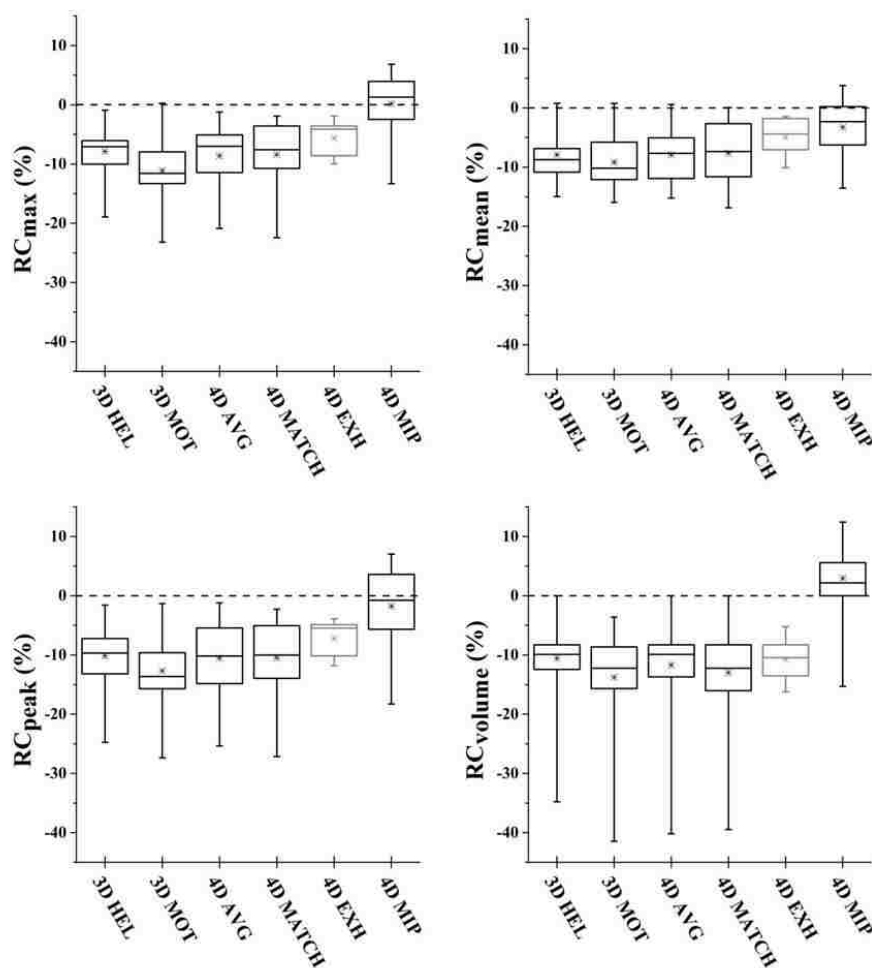
Figure 2-5. Box plots depicting 4DPET activity recovery over all investigated respiratory motion waveforms as a function of CTAC

4DMIP CTAC produced significantly more accurate recovery coefficients. The end-exhale case of 4DEXH demonstrated the least variability; however, note that 4DEXH (depicted in grey) represents only a single PET/CT image phase, versus five image phases for the other CTAC methods. Similar trends were seen between metrics. Box represents median and interquartile range of distribution; x represents mean; hash marks represent minimum and maximum.

2.4.2 *Impact of CTAC on 4D PET*

For 4DPET imaging, the maximum intensity projection (4DMIP) CTAC produced significantly more accurate recovery coefficients than all other CTAC methods (*p<0.0001* over all metrics; *see Figure 2-5)*. Over all waveforms, ratios of 4DMIP CTAC recovery were 0.2±5.4, -1.8±6.5, -3.2±5.0, and 3.0±5.9 for RC_{max}, RC_{peak}, RC_{mean}, and RC_{vol}. In comparison, recovery coefficients for phase-matched CTAC (4DMATCH) were -8.4±5.3, -10.5±6.2, -7.6±5.0, -13.0±7.7 for RC_{max}, RC_{peak}, RC_{mean}, and $RC_{vol.}$, 4DMATCH CTAC recovery was significantly more accurate than 3DMOT, the "free breathing" helical CTAC when evaluating RC_{max} (p=0.001), but not significantly more accurate than other CTAC methods or when evaluating other image metrics. When considering only the subset of 4DMATCH images that corresponded to the end-exhale image phase, 4DEXH, mean and interquartile range was similar to 4DMATCH but variability was considerably reduced.

When evaluating the distribution of recovery coeffecients between RC_{max}, RC_{mean}, RC_{peak}, and RC_{vol} in Kruskal-Wallis ANOVA, significant differences between recovery was found between the different metrics (p=0.001). These trends were characterized by increased variability in the distribution of RC_{vol} recovery and decreased variability with RC_{mean} recovery; however, trends in mean and median recovery were similar between metrics.

PET bin	1	2	3	4	5
CT phase	10%	30%	50%	70%	90%
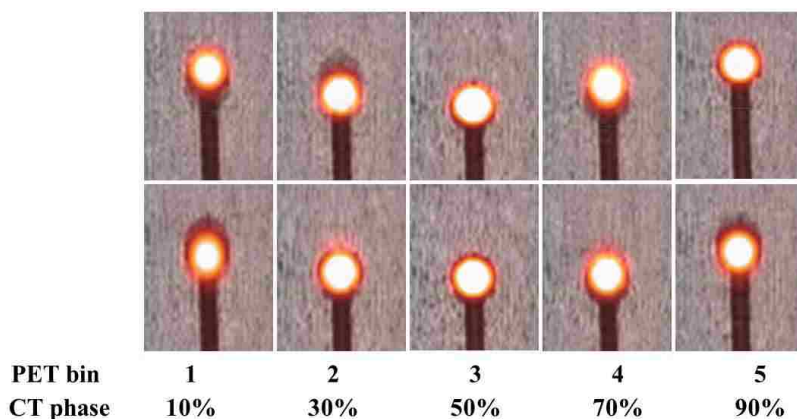
Figure 2-6. 4DPET/CT images with phase-matched CT attenuation correction for two representative patient-specific respiratory motion cases

While good agreement is generally seen at end-exhale phases (middle panel), phase mismatch is evident at other phases. CT phase number indicates center of phase bin.

2.4.3 *4DPET recovery as a function of phase*

Visual inspection of 4DPET/CT with 4DMATCH reconstruction revealed mismatch between PET and CT images phases (*see Figure 2-6*). When testing differences between phases over all CTAC methods and waveforms with Kruskal-Wallis ANOVA, significant differences between phases were revealed (p=0.005). However, these differences were driven by the patient-specific respiratory waveforms; when testing patient and sinusoidal waveforms separately with Kruskal-Wallis ANOVA, patient waveforms were significantly different between phases (p<0.0001) while the sinusoidal waveforms were not significantly different (p=0.98). The 70% and 90% phases, which correspond to the inhale phases where motion is typically greatest in a patient's respiratory cycle, demonstrated poorest accuracy and greatest variability in recovery coefficients (*see Figure 2-7*).
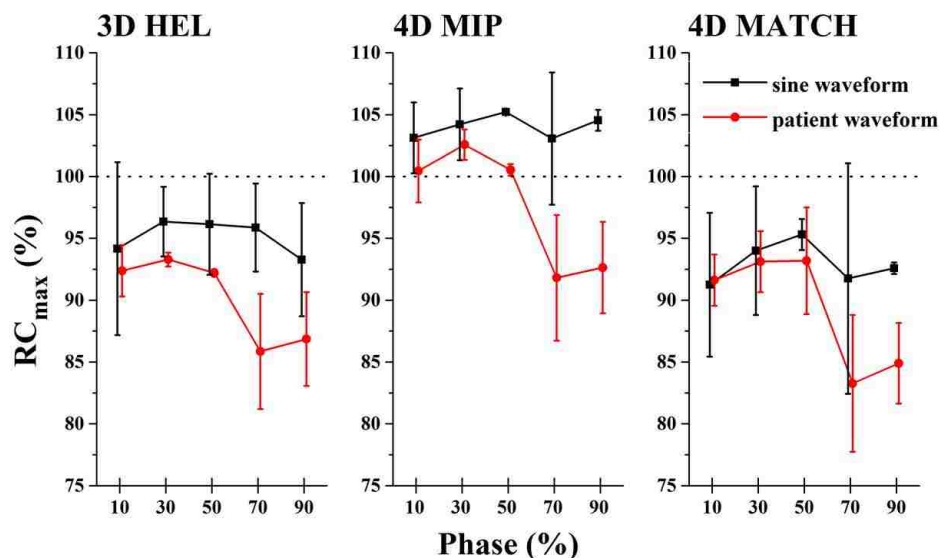
Figure 2-7. 4DPET recovery coefficients for maximum uptake as a function of respiratory phase and CTAC method

Patient-specific respiratory waveforms result in reduced accuracy and increased variability versus sinusoidal waveforms in the 70-90% phase range, which corresponds to inhale phases.

2.4.4   *Lesion periphery and threshold sensitivity*

The effect of CTAC choice on peripheral enhancement of RC_{max} and RC_{mean} was measured within an isotropic 2 cm expansion of the lesion (*see Figure 2-4*). For RC_{max}, a uniform elevation of peripheral uptake for the motion case versus the static case was observed, but no significant differences were measured between CTAC types (*see Figure 2-8*). For RC_{mean}, a significant increase in background uptake in the vicinity of the lesion was measured for 4DMIP CTAC versus other CTAC methods on the order of 10% (*p<0.0001*).
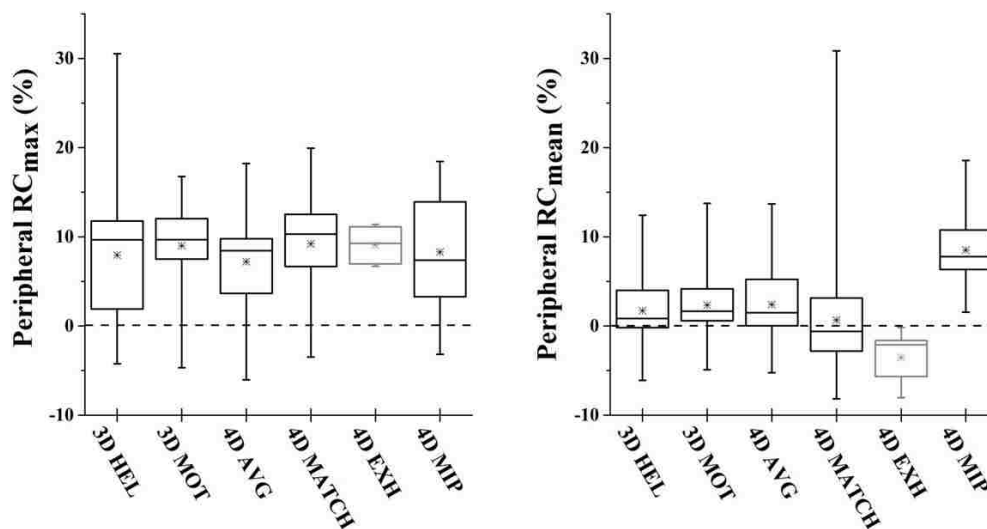
Figure 2-8. Effect of CTAC on background enhancement within a 2-cm volumetric
expansion of the lesion

*No significant differences in maximum uptake were measured. For RC_{mean}, 4DMIP CTAC
resulted in higher uptake within the 2-cm expansion. Box represents median and interquartile
range of distribution; x represents mean; hash marks represent minimum and maximum.*

The effect of variance in segmentation threshold on RC_{vol} was also investigated by scaling the
threshold obtained from the ground truth comparison of sphere volume. Changes in threshold
setting led to proportional changes in recovered volume (*see Figure 2-9*). For example, recovered
volume for 4DMIP was 5.05+0.40 mL for 49.5% of maximum, 5.72+0.33 mL for 45.5% of
maximum, and 6.45+0.32 mL for 40.5% of maximum. As a consequence, while 4DMIP
demonstrated highest accuracy of the six methods for thresholds of 45.5% (derived from the
ground truth comparison) and 49.5%, it showed lowest accuracy for the 40.5% threshold
segmentation.
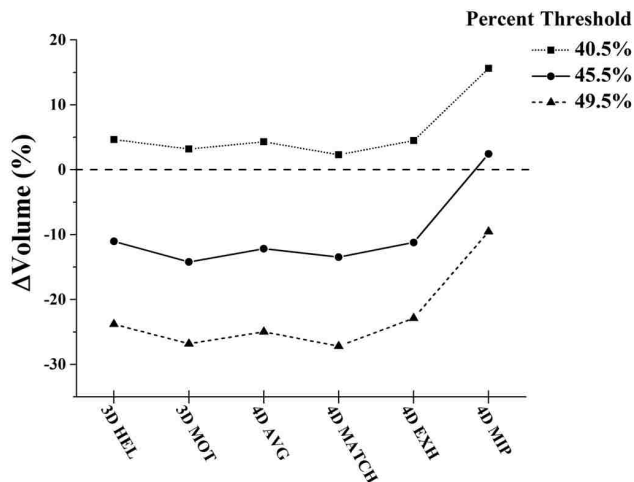
Figure 2-9. Volume recovery coefficients as a function of CTAC method and threshold segmentation method

Volume recovery scaled proportionally as a function of percent maximum threshold.

2.5   DISCUSSION

CT attenuation correction method is an important consideration for thoracic PET quantification in the presence of respiratory motion. In this study, we have investigated the impact of six CTAC methods on PET image quantification in the presence of simulated patient-specific and sinusoidal respiratory motion. In contrast to previously published work, minimal advantage from the use of phase-matched (4DMATCH) CTAC was shown versus other methods such as helical CTAC. Here, strong advantages in accuracy of SUV metrics and thresholded volumes were demonstrated with the use of the maximum intensity projection (4DMIP). These results indicate that though respiratory phase-matched CTAC should in theory provide optimal corrections, image artifacts and differences in implementation of 4DCT and 4DPET sorting can reduce the benefits of this approach.

Despite the theoretical advantages of the phase-matched CTAC method, this study noted significant advantages over other methods in only a single case (significant improvement in RC_{max} compared to helical CTAC in the presence of motion). No significant differences were detected for RC_{peak}, RC_{mean}, or RC_{vol} or versus other CTAC methods. This result for RC_{max} was similarly reported in the literature by Ponisch et al[113], though their work showed a substantially greater improvement in accuracy, and also an advantage in thresholded volumes, which was not observed here. One distinction between this work and the prior work is the investigation of five motion conditions, including three patient-specific respiratory waveforms. By comparison, the prior work investigated only a single eccentric sinusoidal waveform. The use of patient-specific waveforms is hypothesized to lead to increased CTAC artifacts due to changes in motion patterns over time (*see Figure 2-2*). Additionally, the present work used a lung-equivalent background, which leads to more substantial and realistic 4DCT and 4DPET artifacts than the homogeneous background used by the prior work. Killoran et al investigated four sinusoidal waveforms with heterogeneous background and noted mixed results in comparisons of phase-matched, phase-averaged CTAC, and helical CTAC[115], which agrees more closely with our results. More investigation is required as differences in experimental design, including design of phantom, respiratory correlation techniques, scanner vendor, commercial or in-house reconstruction software, 2D or 3D PET acquisition, and reconstruction settings will affect image quantification. However, it is clear that 4DPET/CT accuracy is limited by the difference in respiratory sampling during image acquisition: long acquisition time of respiratory-correlated PET integrates motion over many respiratory cycles per phase bin, while the short acquisition time of respiratory-correlated CT integrates motion over only 1-2 respiratory cycles per phase bin, which in turn contributes to phase mismatch of CT and

PET images. These effects should be investigated before implementing phase-matched 4DPET workflows for clinical use.

The 4DMIP CTAC showed the highest accuracy in quantitative applications in this phantom study, and has similarly been shown to be advantageous in cardiac PET. However, other factors could lead to reduced accuracy depending upon the application. One concern could be overcorrection at the periphery of the lesion, though the results presented here suggest this is a minor effect. The maximum uptake in the periphery was not increased while the mean uptake in the periphery was elevated on the order of 10%. This suggest modest enhancement of uptake in the voxels closest to the object in motion; however, this enhancement remains below the lesion activity. Furthermore, many of the specific applications of thoracic FDG PET, such as SUV_{max} or SUV_{peak} assessment for treatment response, may be unaffected by minor enhancement in the lesion periphery. Another factor that this experiment is incapable of evaluating is the effect of the maximum intensity projection on the external patient contour, which may appear larger under respiratory motion and lead to overcorrection of photon attenuation and thus uniformly escalated SUV values. Again, for response evaluation, this effect may be reduced in importance assuming general consistency in body habitus and respiration between scans. Despite these limitations, these results motivate further study of the application of the maximum intensity projection CT for thoracic PET/CT attenuation correction.

While the use of a physical respiratory phantom offered the benefit of a controlled experimental design, there are additional limitations with this phantom. Considering that the moving feature was surrounded by lung equivalent material, the presented results may be specific to PET imaging of

lesions in low-density regions. Likewise, the hot sphere/tumor was filled through a stem that retained modest amounts of residual activity (approximately 10% of the sphere activity) and translated during motion in and out of the tumor position. While this may bias results, the fillable area of the stem is roughly 0.2 cm in diameter compared to the 2.2 cm sphere and should have minimal impact on results. Similarly, the effects of tumor heterogeneity or tracer kinetics in the patient could bias the results versus the uniform sphere used here and cannot be evaluated. Furthermore, we evaluated only a fixed count density and the standard caveats apply that results may vary as a function of lesion-to-background ratio, count density, and noise levels. However, the previous investigation by Park et al of three different tumor-to-background ratios suggests that contrast does not strongly affect 4DPET recovery, and thus the corresponding fractional changes as a function of CTAC method are likely to be small[114]. Counts for 4DPET acquisition were matched to the reference 3DPET acquisition per scan, not per bin, which most closely reflects clinical practice, but could bias the results. However, an analysis of normalizing activities to reference objects defined on 3DPET or 4DPET with corresponding differences in count levels suggests this is not a significant effect.

When considering 4DEXH, which consists of only the end-exhale phase of the 4DMATCH dataset, considerably reduced variability was seen with similar accuracy profiles to 4DMATCH. While accuracy remained lower than 4DMIP, 4DEXH may be an appropriate strategy for response assessment, where reduced variability may be of higher importance than small gains in accuracy, and relative response rates may wash out absolute bias. However, as 4DEXH only represents 20% of the entire respiratory waveform, it would not be appropriate for applications where it is desired to encompass motion, such as radiotherapy target definition in the free-breathing setting.

Limitations of 4DCT image quality in the presence of respiratory motion appeared to be a limiting factor in the performance of various 4DCTAC approaches. Various methods have been proposed to improve robustness and reduce artifacts in respiratory-correlated imaging, including long duration scanning with low dose CT[88] and various mathematical approaches such as amplitude-based sorting, deformable interpolation, and respiratory modeling through principle component analysis. Similarly, new developments are underway for 4DPET. The use of linear surrogates such as the camera-based or pressure belt-based systems have been criticized for various reasons, including lack of correlation to tumor motion at depth, and alternative methods under investigation include marker-less tracking and full surface tracking[118].

In this study, we evaluated four common PET image metrics. However, these metrics may not evaluate the impact of attenuation correction methods on other important image characteristics that are used for diagnosis or target definition. As an example, the effect of CTAC on lesion shape, uniformity, heterogeneity, or textural features was not evaluated. Similarly, the limitations of fixed threshold segmentation are well-known; for example, the seminal work of Nestle et al[119]. While other advanced segmentation techniques such as adaptive thresholding, gradient methods, or statistical modeling may provide more accurate lesion segmentation[120-122], the purpose of this study was not to define the optimal segmentation method, but to evaluate the quantitative impact of CTAC choice on threshold segmentation because it is the most commonly-used volume metric in the literature. In this study, changes in threshold setting on the order of 10% led to proportional changes in volume recovery, with the magnitude of recovery between CTAC methods remaining roughly constant in proportion to each other. As a result, the 4DMIP CTAC showed poorest

accuracy at the 40.5% percent maximum threshold despite greatest accuracy for all other threshold settings and SUV metrics. This reinforces the challenges of defining an optimal threshold setting outside of a ground truth phantom study, such as for patient data in the clinical setting. Unfortunately, no consensus exists on more optimal segmentation techniques and they are not yet widely available in the clinical environment. Further investigation is warranted on this topic.

2.6   CONCLUSION

CT attenuation correction method is an important consideration for thoracic PET quantification in the presence of respiratory motion. While respiratory phase-matched CTAC should in theory provide optimal corrections, image artifacts and differences in implementation of 4DCT and 4DPET sorting can degrade the benefit of this approach. Comparative advantages in accuracy and precision of SUV metrics and thresholded volumes were demonstrated with the use of the maximum intensity projection and end-exhale CT attenuation correction. These results may be useful to guide the implementation, analysis, and development of respiratory-correlated thoracic PET/CT in the radiation oncology and diagnostic settings.

Chapter 3. EXTENDED DURATION FOR RESPIRATORY-GATED PET/CT

3.1 WHY EXTENDED DURATION?

Positron emission tomography/computed tomography (PET/CT) imaging has emerged as a standard component for cancer staging and treatment. However, PET/CT imaging of the lung and abdomen is usually compromised by respiratory motion, of which the attenuation correction error caused by mismatch between PET and CT images is one of the major reasons. To reduce the mismatch, cine CT, which acquires multiple axial scans over time at a single bed position, has been adopted to provide phase-matched respiratory-gated CT data for respiratory-gated PET attenuation correction. However, due to a broad variability of intra-scan motion and inter-PET-CT motion in practice[123], traditional short-duration cine CT may be inadequate to match PET scan data and consequently compromise the quality of attenuation correction[69]. Thus, in this work, we propose to use long-duration cine CT with the cine duration 10 times as long as the traditional short-duration cine CT. We note that extending the duration by a factor or 10 requires an equal reduction in patient dose per unit time to keep the total dose constant, and we are addressing that separately[88,124]. The goal of this study is to determine if extending the cine CT duration will reduce the mismatch between PET and CT motions and therefore improve the accuracy of attenuation correction and thus the PET images.

3.2 METHOD

We simulated FDG-PET/CT scans with the 4D extended Cardiac-Torso (XCAT) phantom[125] to generate 3D distributions of radiotracers and linear attenuation coefficients of the patient body,

with two 1.5 cm diameter spherical objects added to simulate lung tumors. We used Varian Real-time Position Management (RPM) traces from 11 patient PET/CT scans to drive the rendering of XCAT images with simulated tumors, with amplitudes of anterior-posterior expansion in XCAT images matching amplitudes of RPM displacements. For each respiratory motion trace, we first simulated PET acquisition over 4 minutes for 1 bed position covering 16 cm axially, and then we simulated cine CT images for 4 consecutive bed positions, each covering 4 cm. Note that there was no overlap in RPM traces between PET and CT simulations. We used the retrospective phase-gating strategy in our simulation. For a given respiratory cycle determined from the RPM trace, we generated 10 equally spaced frames, with each corresponding to 1 of 10 respiratory phases. For each cycle, the PET frames were generated using percentage binning with each frame covering 1/10 time of the cycle, while the cine CT frames were generated with each frame covering one full rotation (0.5 second). Each final phase is then generated by averaging over all frames corresponding to the same phase over multiple breathing cycles. This method ensures phase matching between PET and associated cine CT images.

To simulate PET acquisition of a free breathing patient, we first created a 4D XCAT emission phantom dataset by generating 50 3D XCAT emission phantoms with anterior-posterior expansion sampled over a 5-mm amplitude. Each 3D XCAT emission phantom was then forward projected with the matched attenuation map to generate 50 emission sinograms. We used a method[126] to form noisy motion-blurred sinograms according to a given RPM trace. That is, for each respiratory phase, the 50 emission sinograms were weighted according to the histogram of the RPM displacements corresponding to this particular phase, and then summed and normalized to form a phase-gated motion- blurred sinogram. All the resultant sinograms were convolved with a spatially variant PSF model measured from the GE D690 scanner to simulate the detection blurring effect.

Poisson noise, scatter events, and random events were also added to the emission sinograms.

We compared the traditional short-duration cine CT (5 seconds cine time) with the proposed long-duration cine CT (50 seconds cine time). More specifically, we simulated 5-second cine CT and 50-second cine CT both starting at the same time point. For performance evaluation, we simulated the phase-gated average attenuation anatomy image as a benchmark, which represents the CT image that would be obtained if one performed the respiratory-gated CT scan simultaneously with the PET scan and would therefore produce arguably the most accurate attenuation correction for PET images. Thus, the resultant PET reconstruction using average anatomy images for CT attenuation correction (CTAC) is considered to be the most accurate reconstruction as we can possibly have in this experiment and will therefore be used as a reference.

We reconstructed each phase-gated PET sinogram data with a voxel size of 2.73 x 2.73 x 3.27 mm^3 using the ordered- subset expectation-maximization (OS-EM) reconstruction algorithm with 3 iterations and 32 subsets. A Gaussian post- filter with 6 mm full-width-at-half-maximum (FWHM) and a heavy axial filter were applied to the reconstructed images. The noisy emission data was reconstructed with three different CTAC factors converted from the abovementioned CT images. Each reconstructed activity image was normalized using the lung background activity measured on the same image.

For comparison, we calculated the root-mean-square-error (RMSE) between gated average attenuation anatomy images and associated cine CT images for each phase, which reveals the mismatch between PET and CT acquisition. We also computed the RMSE between reference reconstruction using average anatomy as CTAC and reconstructions using subsequent cine CT images as CTAC, which indicates the accuracy of using cine CT images for PET attenuation

correction. Note that the RMSE was evaluated within the support of the XCAT phantom with all surrounding air pixels excluded.

3.3   RESULTS

3.3.1   *Results for an irregular, medium amplitude breathing pattern patient*

Figure 3-1 shows that the 50-second cine CT eliminates the artifact on the diaphragm in the 5-second cine CT image caused by mismatch between adjacent bed positions, and thus prevents the propagation of the CT artifact at the diaphragm into PET reconstruction via attenuation correction.
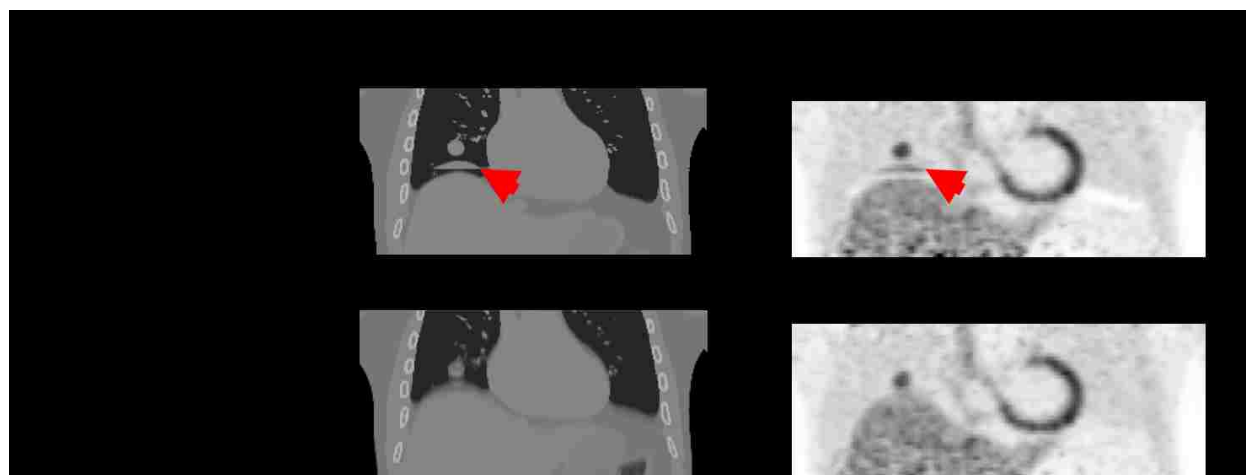
Figure 3-1. Representative 4-D gated CT and PET images of different cine acquisition time

3.3.2   *Results for all patients in this study*

The 50-second cine CT also produces more accurate reconstruction of the overall activity than the 5-second cine CT on average for almost all patients. Table 3-1 presents the average RMSE evaluated over all phases and patients. It shows that, among all patients in our study, extending the cine CT duration from 5 seconds to 50 seconds reduces the mismatch between PET and CT by roughly 41%, and also results in a roughly 42% improvement in overall PET reconstruction

accuracy.

Table 3-1. Average RMSE over all respiratory phases and patients in attenuation maps and normalized reconstructed activity images for different cine CT durations.

Average RMSE over all patients	Attenuation maps (HU)	Normalized activity images (a.u.)
5-sec cine CT	61 ± 20.8	0.072 ± 0.042
50-sec cine CT	36.6 ± 15.5	0.042 ± 0.032

3.4   CONCLUSION

In this work, we propose to use a long-duration cine CT for respiratory-gated PET/CT, whose cine acquisition time is ten times longer than a traditional short-duration cine CT. The results of phantom simulation with real respiratory traces show that, the long-duration cine CT reduces the mismatch between PET and cine CT by 41% and improves the overall reconstruction accuracy by 42% on average, as compared to the traditional short-duration cine CT. The long-duration cine CT also reduces artifacts in PET images as caused by misalignment and mismatch between adjacent slices in phase- gated CT images. The improvement in data matching by extending the cine duration depends on the patient, with potentially greater benefits for patients with irregular breathing pattern and larger diaphragm movement. Future work includes experimenting with more respiratory traces with a wide variability of breathing patterns and evaluating local activity for individual lesion.
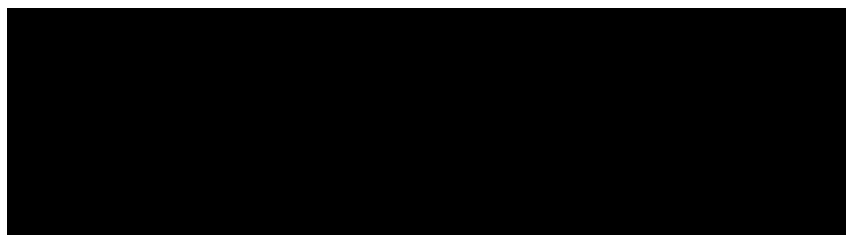
Chapter 4. POST-LOG APPROACHES FOR THE LOW DOSE IMAGING

4.1 ULTRA-LOW DOSE CTAC FOR PET/CT: ANALYSIS OF SPARSE VIEW DATA ACQUISITION AND RECONSTRUCTION ALGORITHMS[124]

4.1.1 *Introduction*

As introduced in Chapter 3, extended duration of CT acquisitions over multiple respiratory cycles could help compensate for respiratory motion induced artifacts. On the other hand, extended scanning time also means increased the total radiation dose. In the previous publication, with proper settings of voltage and x-ray spectra, we had shown that low dose CTAC for PET is clinically feasible[88]. For ultra-low dose CT imaging, due to the photon starvation effect, streak artifacts and HU bias could compromise the accuracy of CT-based attenuation correction for PET. One way to reduce the bias is reducing the projection view number so that the relative electronic noise could be lower while total number of detected photon remains[127,128]; however, it also lead to aliasing artifacts. Therefore, in this research, seven sparse-view acquisition protocol were tested -- 984, 328, 123, 41, 24, 12, and 8 views. Two different sparse-view simulations were tested: continuous exposure averaging approach and the tube pulsing approach. On the other hand, two CT reconstruction algorithms, FBP and MBIR, were used for generating the CT image for AC of PET. Dose scheme were varies from 0.35 mAs to 0.04375 mAs. Though comparing the quantitative information on the CTAC PET image, we are able to determine the optimal ULDCT acquisition protocol in order to achieve the relative best PET image accuracy.

Table 4-1. Acquisition protocols for the sparse-view ultra-low dose CT imaging

4.1.2 *Method*

We used the Computer Assisted Tomography Simulator (CatSIM[129]) for the simulation of the x-ray CT imaging. A 140 kVp polychromatic x-ray spectrum was used in our simulation. The x-ray photons reaching the detector at each energy bin is modeled as a Poisson process and are converted to a signal proportional to the sum of energies. Electronic noise is modeled as Gaussian noise (see Chapter 6.3.6, page 91, for similar simulation details). Continuous exposure mode was simulated by summarizing sub views between neighboring views prior to log conversion. To simulate the tube pulsing data which is acquired by turning on the tube at desired location, we performed the simulation with all 984 views then dropped the views which are not needed. In this way, the exposure time for each view remains unchanged. In the tube pulsing data acquisition mode, the mA level is increased to maintain the equal dose level. Details for the MBIR algorithm can be seen in the section 5.2.3.

3D PET geometry of the GE Discovery 600 scanner was simulated in this report, but used a single block ring consisting of 6 axial detectors resulting in 31 direct and oblique planes. The simulated system geometry has 339 radial bins, 256 angular bins, a FOV diameter of 700 mm and 40 mm longitudinal coverage per bed position. The resulting PET simulation data had 10 million counts including true and scattered coincidence events. Random coincidence events, detector blurring,

and normalization were not modeled as our study focused on investigating the effects of attenuation correction with CT images on PET quantitation. 20 i.i.d. Poisson noise realizations of the PET sinogram data were generated. A bilinear transformation was used to convert the CT reconstructed images to attenuation coefficients at 511 keV and used for PET reconstruction. PET images were reconstructed with 2 iterations, 28 subsets of OSEM using attenuation estimates from ultra-low dose CT.

4.1.3   *Result and discussion*

Table 2-2 and

Table 2-3 shows the ensemble RMSE of the PET uptake value comparing to the regular-dose CTAC PET image. The simulation demonstrated that ULDCT-based attenuation correction can be achieved at dose levels on the order of 0.044 mAs with little impact on accuracy of PET uptake value. Highly sparse 41- or 24- view ULDCT scans are feasible for PET attenuation correction, providing the best tradeoff between electronic noise and view aliasing artifacts. The continuous exposure acquisition mode could potentially be implemented in current commercially available

scanners, thus enabling sparse view data acquisition without requiring x-ray tubes capable of operating in a pulsing mode. On the other hand, pulsing mode also showed marginal improvement in the uptake accuracy, which imply it could be a potential approach for more accurate ultra-low dose CT when pulse CT acquisition mode is available on the PET/CT scanner.

Table 4-2. Ensemble RMSE of PET images from CT-based attenuation correction for continuous exposure technique[124]
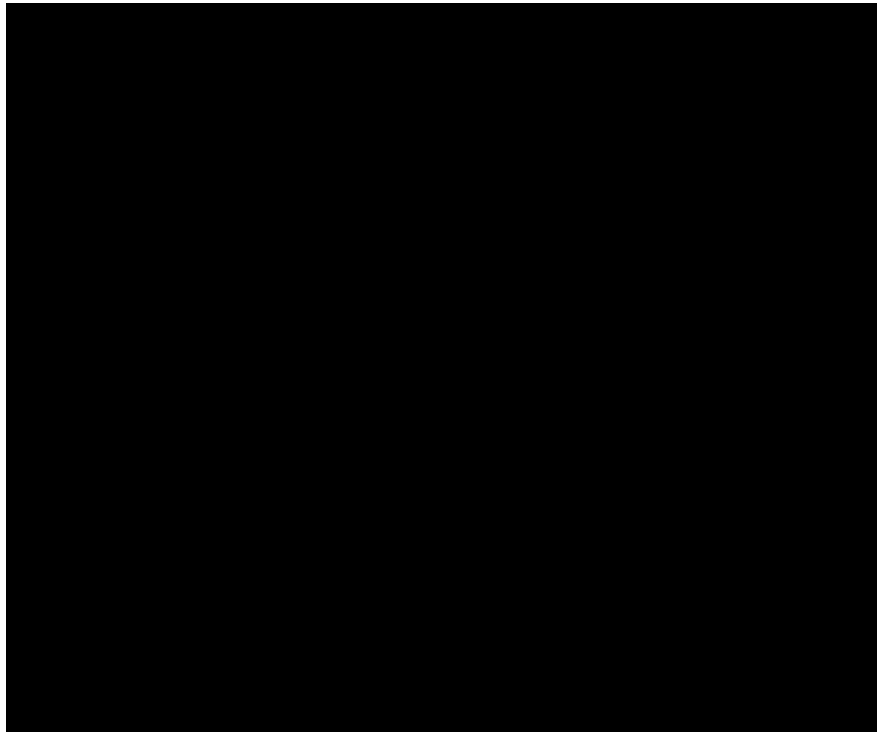
Table 4-3. Ensemble RMSE of PET images from CT-based attenuation correction for tube pulsing technique[124]
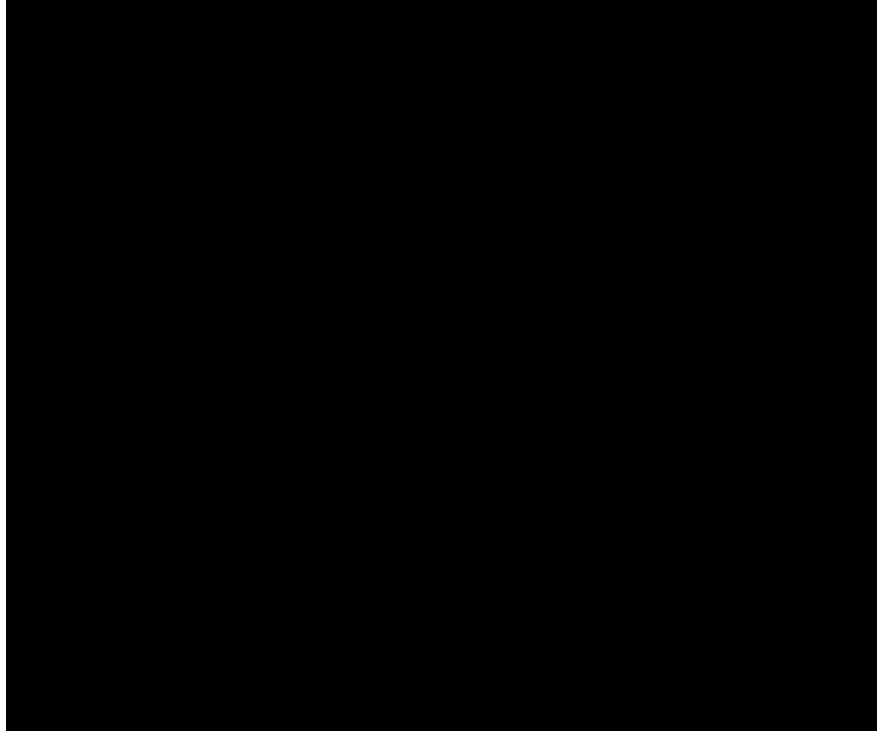
4.2 VARIANCE ESTIMATION FOR ITERATIVE RECONSTRUCTION OF EXTREMELY LOW-DOSE CT DATA

4.2.1 *Introduction*

In ultra-low dose protocols, the CT images suffer from the increased bias and noise in measurements. There are numerous efforts to improve the image quality for low-dose acquisitions, and here we focus on post-log reconstruction excluding the additional low dose techniques such as sparse view recovery [127,130,131] or penalty functions[132]. One inherent limitation of post-log reconstruction is how to treat the non-positive sinogram values prior to logarithm operation. We investigated the impact of the mean preserving filter (MPF)[133] for the variance of the CT data, and we proposed a new variance expression including the effect of non-positive correction in the intensity domain to make WLS (weight-least squared) reconstruction more accurate in estimate

for the variance (weight). In this report, we compared two different weight estimation models: quantum and electronic noise model (W_{SQE})[93] and the proposed advanced variance estimation model (W_{AQE}) for the MPF-operated ultra-low dose CT data in the PWLS algorithm. Through analyzing the bias of final reconstructed CT images, we would like to show that the statistical distribution (here: variance) change by the non-positivity correction should also be considered in the iterative reconstruction process, and that could benefit the overall accuracy in the ultra-low dose CT image.

4.2.2 *Method*

Thibault *et al*. proposed a combined Poisson quantum and Gaussian electronic noise (Gaussian variance: σ_e^2) model[93]. The approximate weight:

$$\qquad\qquad\qquad\qquad\qquad\qquad\qquad\qquad\qquad\qquad\qquad (1)$$

However, both noise models, quantum only and combined quantum and electronic variance models, do not consider the effect of pre-corrections performed prior to log conversion of the measured data. Here, we chose MPF (*see section 6.3.7*) for non-positivity correction in the variance model analysis. We extended Thibault's weight estimation including the effect of two successive steps, positivity enforcing and error dispersion, in MPF. Since $\tilde{\lambda}$ is a function of a random vector $\tilde{\mathbf{X}}$, which is a sum of offset-subtracted pre-log ($\mathbf{X}$) and error dispersion ($\mathbf{E}$) random vectors, the variance of $\tilde{\lambda}$ in denominator of (1) can be approximated by Taylor expansion for the first and second moments of the function as follows

$$\blacksquare \qquad (2)$$

The mean and variance of $\widetilde{\mathbf{X}} = \mathbf{X} + \mathbf{E}$ are

$$\blacksquare \qquad (3)$$

$$\blacksquare \qquad (4)$$

The inverted and first derivative forms of MPF function are

$$\blacksquare \qquad (5)$$

$$\blacksquare \qquad (6)$$

Each element of error dispersion random vector ($\mathbf{E}$) is computed as weighted sum of the changes of neighbors (N_i) of i-th sinogram bin to go previously through MPF function as follows

$$\blacksquare \qquad (7)$$

Assuming independent error random variables, $\boldsymbol{\varepsilon}_n$, of neighbors, the variance of $\mathbf{E}_i$ is approximated as follows, $\sigma_{E_i}^2 \triangleq$

$$\qquad\qquad\qquad (8)$$

The variance of each neighbor, $\boldsymbol{\varepsilon}_n$ is

$$\qquad\qquad\qquad (9)$$

The covariance term in (9) is derived as follows

$$\qquad\qquad\qquad (10)$$

Using (4), (9) and (10), the variance of $\widetilde{\mathbf{X}}_i$ can be practically computed as

$$\blacksquare$$

(11)

with the approximation of $m_Q \cong X = \tilde{X} - E$.

Thus the variance of pre-corrected pre-log data in the denominator of (9) can be changed for the advanced weight matrix as follows

$$\blacksquare$$

(12)

CT simulations with GE VCT scanner's settings were performed of the NCAT chest phantom using the CatSim simulator[129], which generates sinograms (984 views x 888 channel) wih poly-energetic compound Poisson data (0.5 & 10 mAs and 80 kVp) and Gaussian electronic noise ($m_e = 897, \sigma_e^2 = 15^2$) contributions (*see section 6.3.5*). For MPF non-positivity correction (*see section 6.3.7*), the parameter α was set at 20. Twenty iterations with optimized penalized terms were used for each ICD-PWLS CT (512 x 512 pixels) reconstruction[134].

4.2.3   *Result and discussion*

Figure 4-1 and Figure 4-2 shows the reconstructed CT images comparing between FBP and SQE and AQE method for PWLS weight estimation. For both low dose and ultra-low dose images, PWLS reconstruction shows improved RMSE and bias than the FBP reconstruction. For the comparison between SQE and AQE, some improvements could be seen for the bias value (see Table 4-4).
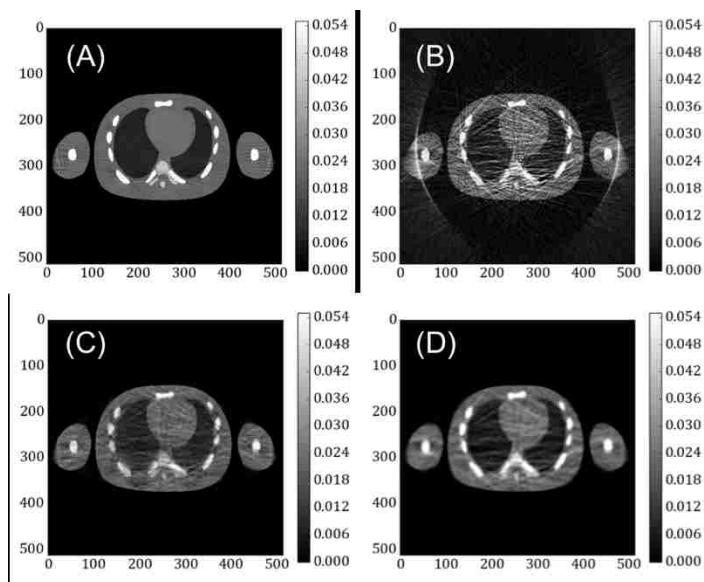
Figure 4-1. Comparison of reconstructed 10 mAs NCAT CT images

(A) 400 mAs FBP reconstruction as the positive control, 10 mAs (B) FBP reconstruction with MPF$_{20}$ non-positivity correction, (C) PWLS reconstruction with MPF$_{20}$ non-positivity correction and SQE weight estimation, and (D) PWLS reconstruction with MPF$_{20}$ non-positivity correction and AQE weight estimation
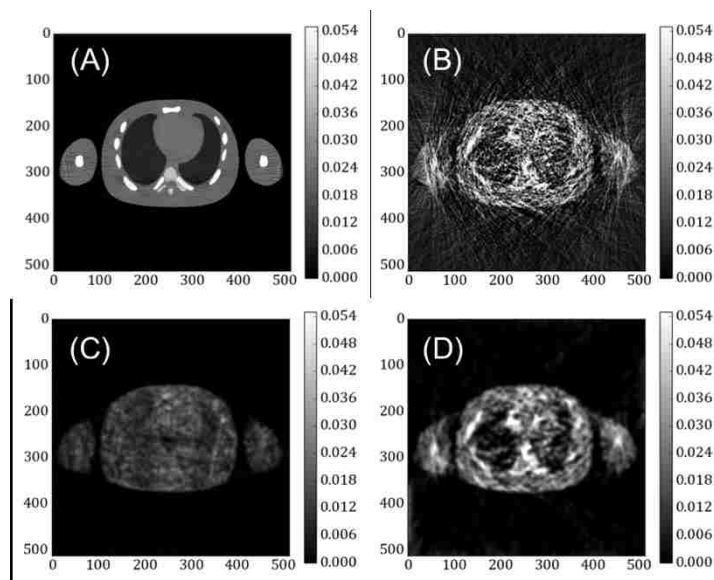
Figure 4-2. Comparison of reconstructed 0.5 mAs NCAT CT images

(A) 400 mAs FBP reconstruction as the positive control, 0.5 mAs (B) FBP reconstruction with MPF$_{20}$ non-positivity correction, (C) PWLS reconstruction with MPF$_{20}$ non-positivity correction and SQE weight estimation, and (D) PWLS reconstruction with MPF$_{20}$ non-positivity correction and AQE weight estimation

Table 4-4. Ensemble RMSE and BIAS of CT images for different acquisition and
reconstruction protocols, unit:1/mm

For the simulated image of 80kVp, 10 and 0.5 mAs of a chest phantom, compared to the
conventional FBP reconstruction methods, the iterative reconstruction method did reduce the
image bias for the low-dose and ultra-low dose image up to 8 times. With practical estimates of
weights for WLS, there was improvement with the advanced variance estimates (W_{AQE})
considering electronic noise and the effect of pre-processing on variance change. But there is an
inherent limitation on image quality improvement of WLS reconstruction based on Gaussian post-
log distribution for extremely low-dose CT imaging.

4.3 COMPARISON BETWEEN PRE-LOG AND POST-LOG STATISTICAL MODELS IN ULTRA-LOW-DOSE CT RECONSTRUCTION

4.3.1 *Introduction*

In chapter 4.1 and 4.2, we introduced applying the model-based iterative reconstruction method
(MBIR) on the ultra-low dose data. However, in previous two sections, we only considered the
case of reconstructing post-log sinograms, where the x-ray transmission data had already been pre-
corrected for detector non-uniformity, tube current fluctuation, non-positivity signals, scatters, etc.
Then the pre-corrected data are logarithmically transformed to the integral values and then
processing for the following model-based image reconstruction. On the other hand, since
algorithms in the pre-log category include Beer's law in the forward model and directly reconstruct

images from the transmission measurements without taking the log operation, there are few possible advantages for the pre-log approaches. First, the bias caused from the non-positivity correction process in order to dealing with DAS electronic noise could be prevented. Second, the bias in the weight estimation process due to the noisy data and the non-positivity correction *(see section 4.2*) could be further prevented too. Thirdly, the bias caused by the logarithm itself could be avoided. Despite certain theoretical advantages of the pre-log approach, both pre-log and post-log models are simplified approximations. It is still an open question whether the pre-log model could notably improve image quality over the post-log model for reconstructing the CT image under the ultra-low-dose level. Therefore, this report quantitatively compares several commonly used pre-log and post-log approaches for the ULDCT data.

4.3.2 *Method*

Here we showed the experimental setup for the ULDCT patient data. The dataset was acquired on a GE Discovery CT750 HD scanner (GE Healthcare, Waukesha, WI) with 64-row collimation, helical pitch of 0.516, 80 kVp, 10 mA, and 0.5 s rotation. This was an ultra-low-dose dataset acquired with the lowest possible setting on the scanner. A standard-dose reference scan was also acquired with 120 kVp, 310 mA, with other settings kept the same. Images were reconstructed on a grid of 512x512 with an in-plane pixel size of 0.98 mm^2 and a slice thickness of 0.625 mm. We compared five statistical options for this patient dataset, with the same definition as the phantom study:

1. Post-log.

2. Post-log with denoised data (3x3).

3. Post-log with denoised data (6x6).

4. Pre-log Poisson.

5. Pre-log shifted Poisson.

The regularization strength in option 4 was manually increased to approximately match image roughness of other reconstructions. For denoised data, a locally adaptive linear minimum mean squared error (LLMMSE) filter was applied[135]. Please refer to the full publication for the detail settings for the statistic model and the reconstruction algorithms[136].

4.3.3 *Result and discussion*

Figure 4-3 shows reconstructed images produced by different MBIR options from the ultra-low-dose patient dataset of chest. The standard-dose FBP image (a) demonstrates large mass in the left chest wall along with two right lung nodules. The ultra-low-dose FBP reconstructions (b) and (c) are extremely noisy even with a soft kernel and pre-denoising of the data. These images nearly obsure the large mass in the left chest wall. Post-log MBIR (d) contains much less noise but shows strong negative bias and precludes evaluation of lung and chest wall images. Application of pre-denoising to post-log MBIR (e) substantially reduces the bias, but even with aggressive denoising (f), substantial bias remains relative to the high-dose reference image. These images enable evaluation of both lung and left chest wall lesions. The pre-log Poisson algorithm (g) shows remarkable improvement of HU accuracy relative to all post-log options, almost fully removing the dark shading in the image, and the HU level as well as appearance of lung and left chest wall lesions are comparable to the high dose reference image. Further incorporating electronic noise model in the pre-log shifted Poisson MBIR (h) reduces some streaks and further reduces noise, but doing this also introduces some slight shading artifacts. The appearance of the abnormalities on image (h) is similar to image (g). Overall, modeling of electronic noise in pre-log MBIR did not

show a definite benefit in this patient dataset. Overall, the negative bias in post-log MBIR is reduced by incorporating pre-denoising filters, and further reduced by pre-log MBIR. Pre-log MBIR with Poisson and shifted Poisson model shows a comparable level of HU accuracy.
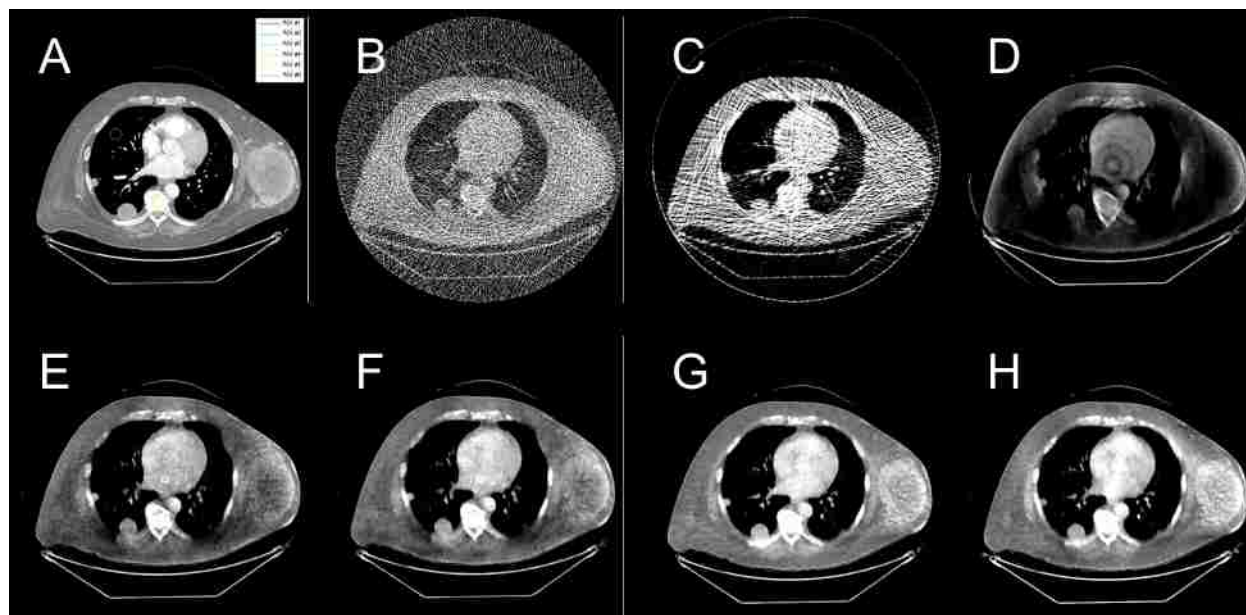
Figure 4-3.Images reconstructed by different algorithms from the same ultra-low-dose (0.5mAs) patient data set[136].

A: Control image, high dose FBP, B: ULDCT FBP, C: ULDCT with denoised data (6x6), D: ULDCT post-log, E: ULDCT post-log with denoised data (3x3), F: ULDCT post-log with denoised data (6x6), G: ULDCT pre-log Poisson, and H: ULDCT pre-log shifted Poisson. HU window [-210, 390]

We presented that the pre-log MBIR is the ability to directly accommodate non-positive transmission measurements in the presence of electronic noise, and reduce the reconstruction bias that would otherwise be caused by clipping of non-positive data. Our results show that pre-log MBIR can achieve notably better quantitative accuracy than post-log MBIR in ultra-low-dose CT, while post-log MBIR without pre-reconstruction denoising shows substantial reconstruction bias

and appears not suitable for photon-starved situations. Overall, pre-log MBIR and electronic noise modeling could play an important role in emerging ultra-low-dose CT applications.

Chapter 5. ULD-CTAC IN PHANTOM AND PATIENTS

5.1 INTRODUCTION

When CT images are used for PET attenuation correction, the images do not need to satisfy the requirement for diagnostic CT images, which are typically high-resolution images with high contrast and low noise. In fact, to match the PET resolution, smoothing filters are typically used to reduce the resolution and noise of the CT images. This allows a further reduction of the CT scan dose beyond the low dose limit of current CT protocols. On the other hand, PET reconstruction has its own specific requirement for the CT attenuation correction (CTAC) images. The artifacts and bias in the CTAC images can easily propagate to PET reconstruction images and results in errors on the PET images. Since the quantitative assessment of the tracer uptake is very important for the clinical diagnostic, the tolerant for artifacts and bias on the CTAC images are typically low. We have conducted a series of simulation studies to explore the opportunity of using ultra-low dose CT images for PET attenuation correction while preserve the quantitative accuracy for the PET images. It has been shown that by combining different techniques such as CT sinogram smoothing, CT spectrum optimization, sparse view data acquisition and iterative reconstruction, it is possible to use ultra-low dose CT scans for PET attenuation correction[88,124]. On the other hand, iterative reconstruction methods are effective in reducing noise and suppressing streaking artifacts, especially for low dose scans compared to the traditional FDK-based analytical reconstruction algorithms[93]. Therefore, we also adopted the model based iterative reconstruction algorithm (MBIR) to further reduce the dose of the CT scan.

In this study, we aim to apply the techniques that have been demonstrated in simulation to patient data acquired from a clinical PET/CT scanner at the lowest possible CT radiation dose. The

quantitative accuracy of the PET images is evaluated using the attenuation map generated based on CT images reconstructed using model based iterative reconstruction (MBIR) and analytical reconstruction. The preliminary results for the torso phantom and a patient study are included in this chapter.

5.2 METHODS

5.2.1 *Phantom PET/CT scan*

A RSD torso phantom (Radiology Support Device, CA) was used in the study, as shown in Figure 5-1. A chest PET scan with corresponding CT scans were performed for this phantom using a GE Discovery STE scanner. For the CT scans, we used a diagnostic CT protocol and an Ultra-Low Dose (ULD) CT protocol:

1. Diagnostic CT protocol: 80 kVp, 200 mA, 0.5 sec (100 mAs).
2. ULD CT protocol 80 kVp, 10 mA, 0.5 sec (5 mAs).

Axial scans for 2-cm thick coverage (16 x 1.25mm) at 8 bed positions were acquired. The CT images were reconstructed using FDK-based reconstruction and MBIR as described below to generate the attenuation correction map for PET image reconstruction. For the PET scan, 2.38 mCi F-18 was injected to the center cavity (around 8.3 liters) of the RSD torso phantom at one hour before a 10-minute 3D PET acquisition.
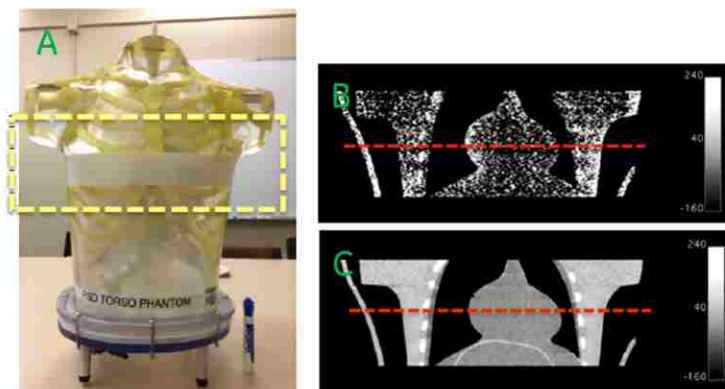
Figure 5-1. RSD torso phantom and its CT images

Image (A) shows the RSD torso phantom used in this study. The yellow rectangle in the dash line indicates the scan range. Image (B) and (C) show the coronal view of the CT scan images acquired at ultra-low dose and normal diagnostic dose. The red dash line indicates the center slice position.

5.2.2   *Patient PET/CT scan*

Patients were scanned by department of radiology, University of Washington using a GE Discovery STE scanner. In this chapter, we report results from two female patients.

A. Patient 1 – ULDCT in axial mode, sparse-view:

The reference CT images which server as ground truth for comparison is taken at 120 kVp. Helical mode is used for the reference CT scan with 60 mA, 0.917 s rotation time. An ultra-low-dose (ULD) CT scan was taken at 80 kVp for the same patient. The ULD CT scans were performed at axial mode at 5 mAs. Whole body PET/CT scans were taken for the patient. In the results presented here, we focus on the chest region.

To further lower the dose, we sparsely sampled the data acquired at three different protocols: a total of 41, 24 and 12 views. The 41 views data set was created by selecting 41 views from the 984 fully sample views uniformly. The same procedure was used to generate the 24 and 12 view data

set. Since the original scan was taken at 5 mAs, after dropping the views, the effective dose for the sparse sampled data set were 0.21 mAs, 0.12 mAs, 0.06 mAs for the 41-view, 24-view and 12-view data set. The fully sampled and sparsely sampled data sets were reconstructed using FDK-based reconstruction and MBIR as described below to generate the attenuation correction map for PET image reconstruction.

For the PET scan, 10.55 mCi F-18 FDG was injected to the patient (82 kg) at one hour before a 15-minute, 3 bed positions 3D PET acquisition.

B. Patient 2 – ULDCT in helical mode:

The reference CT images which server as ground truth for comparison is taken at 120 kVp. Helical mode is used for the reference CT scan with 375 mA, 0.917 s rotation time. An ultra-low-dose (ULD) CT scan was taken at 120 kVp for the same patient. The ULD CT scans were performed at helical mode at 9 mAs. Whole body PET/CT scans were taken for the patient. For the PET scan, 10.69 mCi F-18 FDG was injected to the patient (168 kg) at one hour before a 35-minute, 7 bed positions 3D PET acquisition. Since the patient had suspicious endometrial adenocarcinoma; in the results presented here, we focus on lesions in the pelvic region (*see red arrows in Figure 5-2*).
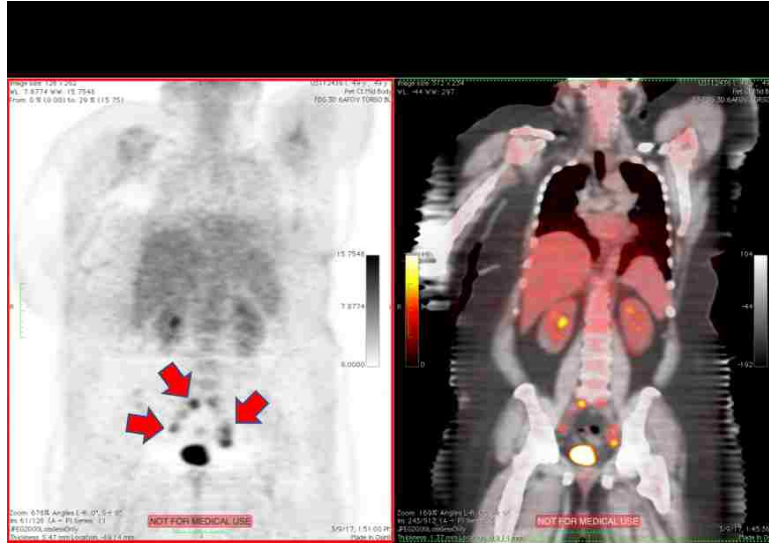
Figure 5-2. Representative PET and PET/CT images of a suspicious uterine cancer patient
(Patient 2)

5.2.3 *CT image reconstruction*

The CT scan data were reconstructed using both FDK-based and MBIR. For MBIR, we used a penalized weighted least square (PWLS) cost function:

$$\hat{x} = \min_{x} f(x)$$

$$f(x) = \left\{ \frac{1}{2} (y - Ax)^T W (y - Ax) \right\} + \beta U(x),$$

where x represents the object volume, y represents the sinogram, A is the system matrix, W is the statistical weighting, $U(x)$ is the prior term and β is the scalar regularization strength. A hyperbolic potential function $U(t)$ was used as the regularization function:

$$U(t) = \delta^2 \left(\sqrt{1 + \left(\frac{t}{\delta} \right)^2} - 1 \right)$$

where δ controls the shape of the prior function. We used $\delta = 0.02 \ mm^{-1}$ to approximate the quadratic prior function. To solve the optimization problem, OS-SPS method was used with 30

OS iterations and 41 subsets[137]. The CT images were reconstructed with a 700 mm in-plane field-of-view (FOV) and a 2.5 mm slice thickness.

5.2.4   *PET data reconstruction and quantification*

All 3D-PET data with attenuation corrections were reconstructed using the OSEM algorithm (4 iterations, 28 subsets). A large ROI was drawn at the middle part of the center slice to calculate the activity in the center region, and a smaller ROI was drawn to represent the non-uptake lung region (*see Figure 5-3Figure 5-7*). Maximum, mean, standard deviation (STDEV), and coefficient of variance (CV) values were measured through the OsiriX viewer v. 7.0 (Geneva, Switzerland). The recovery coefficient (RC) was defined by comparing the measured activity to the control PET image with high-dose (200mAs, 120kvp for the phantom and Patient 2 studies, and 80kVp for Patient 1 study) CT-image attenuation correction.

5.3   RESULTS

5.3.1   *Phantom study*

The representative CT images reconstructed using both FDK-based algorithm and MBIR are shown in Figure 5-1. The CT image acquired with diagnostic CT protocol is also shown in Figure 5-3 for reference. As expected, the CT images reconstructed using FDK-based algorithm with ultra-low dose data suffers from high noise and also significant bias due to the low-signal correction. The CT images reconstructed using MBIR show the advantage at this dose level by significantly suppressing the noise and reducing the bias on the reconstructed images. With the improvement of the CT images, improved PET image quality could be expected.
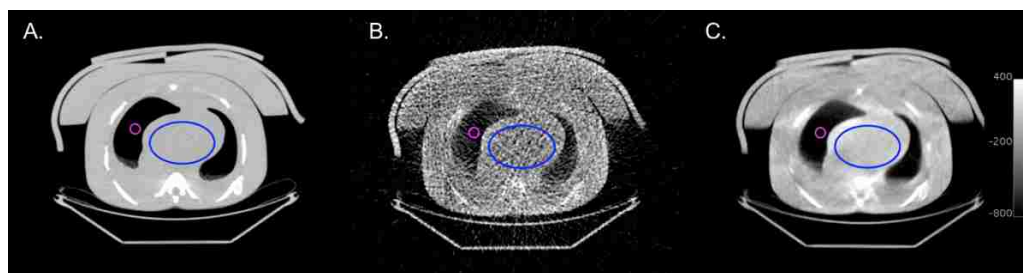
Figure 5-3. The center-slice CT images from the phantom study reconstructed from the ultra-low dose measurement

Control images A (80 kVp, 200 mAs) and B (80 kVp, 5 mAs) are reconstructed images from FDK-based reconstruction. Image C (80 kVp, 5 mAs) are reconstructed with MBIR. The display window for the images is [-800, 400] HU. The blue-color circle, center ROI, is mainly composited by water equivalent material, and magenta-color (lung ROI) circle represents the air.
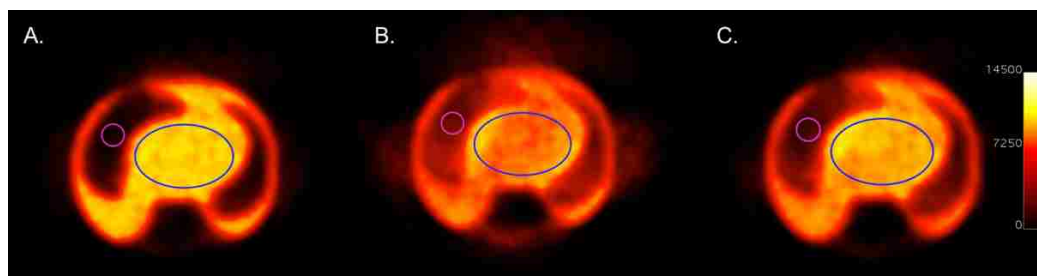
Figure 5-4. The correspondent PET images from the phantom study with the ultra-low dose CTAC

A. 80 kVp, 200 mAs, FBP-CT recon; B. 80 kVp, 5 mAs, FBP-CT recon; C. 80 kVp, 5mAs, MBIR-CT recon are reconstructed using OSEM. The display window for the images is set from zero to 14.5 kBq/ml. The blue-color circle represents the higher-uptake center ROI, and magenta-color circle represents the non-uptake lung ROI.

The corresponding PET images (*see Figure 5-4*) show a more uniform uptake in the MBIR-based CT-AC images than for the FBP-based CT-AC images. The bias in the PET images was -25% using the ULD-FBP-CT image, and -11% for the ULD-MBIR-CT image. The std. dev. for the PET image ROI was 529, 659, and 610 Bq/ml when using the FBP-CT, ULD-FBP-CT, and ULD-MBIR-CT images. The quantification results are shown in Table 5-1.

Table 5-1. PET quantification results of the phantom with three different CT attenuation corrections.
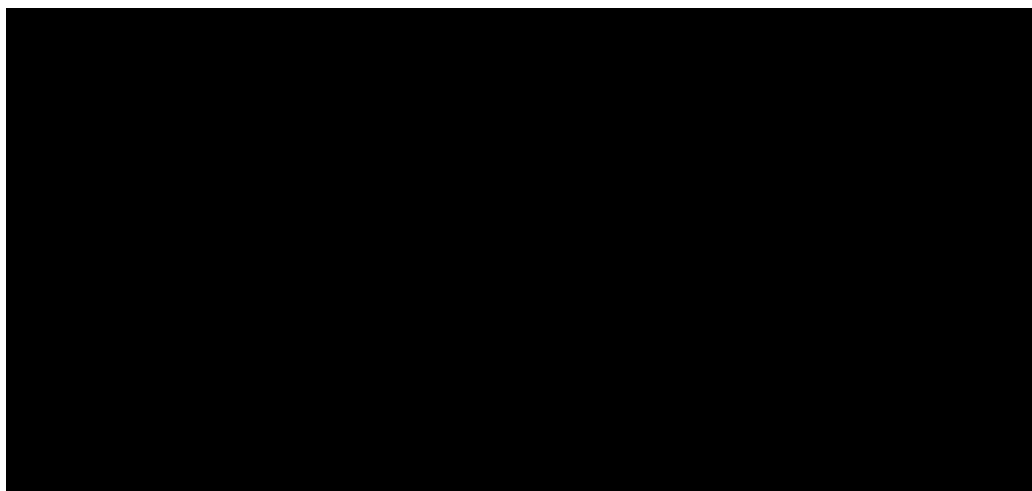
5.3.2   *Patient 1 Study (axial, sparse-view)*

The reconstructed CT images are shown in Figure 5-5. The data sets are sampled at 984 views, 41 views, 24 views and 12 views. Both FDK and MBIR were used to reconstruct the CT images for PET attenuation correction map. It is obvious the CT images reconstructed using MBIR (ULD-MBIR) at ultra-low-dose has less noise compared to the CT images reconstructed using FDK (ULD-FDK). For the sparsely sampled data set, the ULD-FDK CT images has obviously more aliasing artifacts compared to the ULD-MBIR CT images. As the number of sampled views reduces, the equivalent dose for the data set also reduces. Therefore, the ULD-FDK images have significantly higher noise compared to the ULD-MBIR images.

The corresponding PET images are shown in Figure 5-6. When the view number of CT data set reduces, there are obvious artifacts on the PET images reconstructed using the ULD-FDK CT images. For example, for the 12-view CT data set, the PET images reconstructed using ULD-FDK CTAC map has significant bias in the heart region, and dark streaks. The quantitative measurement

on the ROIs are shown in Table 5-2. for both CT and PET images. The noise on the ULD-FDK CT images are very high compared to that on the ULD-MBIR CT images. Especially for the sparsely sampled images, the standard deviation of the measurement is 10 times the mean measurement. The standard deviation measured for the ULD-MBIR CT images is much lower compared to that measured on FDK CT images. For the central ROI located on the heart region, the PET images reconstructed using ULD-MBIR based CTAC map and ULD-FDK based CTAC map shows similar max and mean uptake for the fully sampled data set. When the number of sampling goes down, the bias of the max and mean uptake compared to the control images rises quickly for ULD-FDK based PET recon images (from 17.7 % for 41 views to 90% for 12 views).
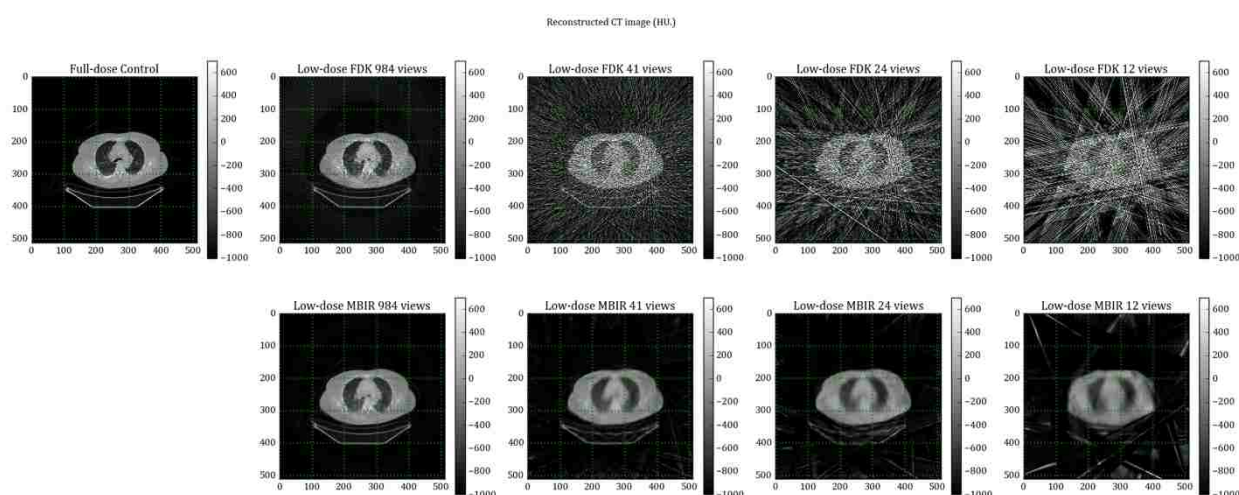
Figure 5-5. The CT images from the patient study used for

PET attenuation correction map generation.

Data were sampled at 984, 41, 24, 12 views. Both FDK (top row) and MBIR (bottom row) are used for the PET reconstructions
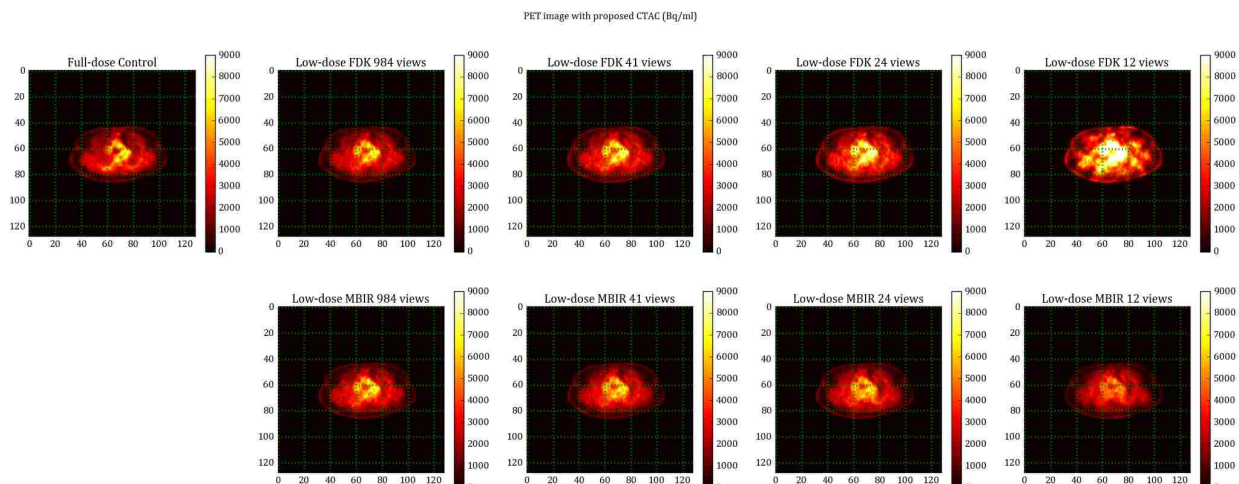
Figure 5-6. The corresponding PET images from the patient study reconstructed using the attenuation map generated from CT images

The CT data were sampled at 984, 41, 24, 12 views. The top row PET images were reconstructed using the correspondent FDK-CTAC images. The bottom row PET images were reconstructed using the correspondent MBIR-CTAC images.

On the other hand, the bias for ULD-MBIR based PET recon images rises slowly and is much smaller (from 0.8% for 41 views to -17.9%). Similar results can be observed for the lung ROI. However, the bias in the lung region is higher than the heart region. It appears, for this patient data set, the ULD scan dose might be too low for CTAC. The lung ROI measurement for the mean uptake is higher than 15% compared to the control images with full sampling. The bias is much higher for the sparsely sampled data set. Even though MBIR has the advantage in suppressing the noise and bias, the absolute bias is still high for Lung ROI.
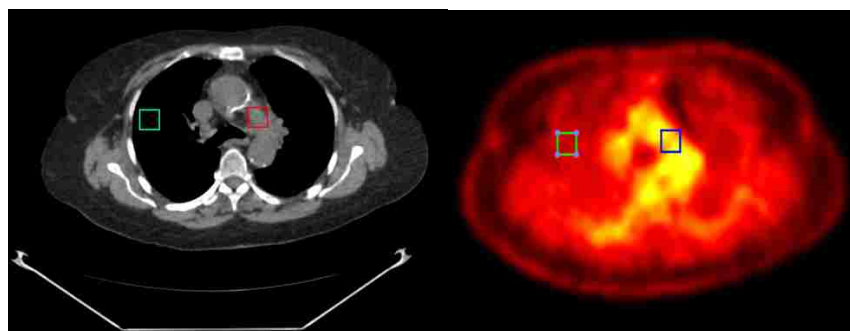
Figure 5-7 The reference CT and PET images for patient ROIs

The display window for CT image was set to [-160, 240] HU. The square indicate the ROI used for the following quantitative analysis.

Table 5-2. The quantitative measurement for the ROIs selected on CT and PET images from patient 1
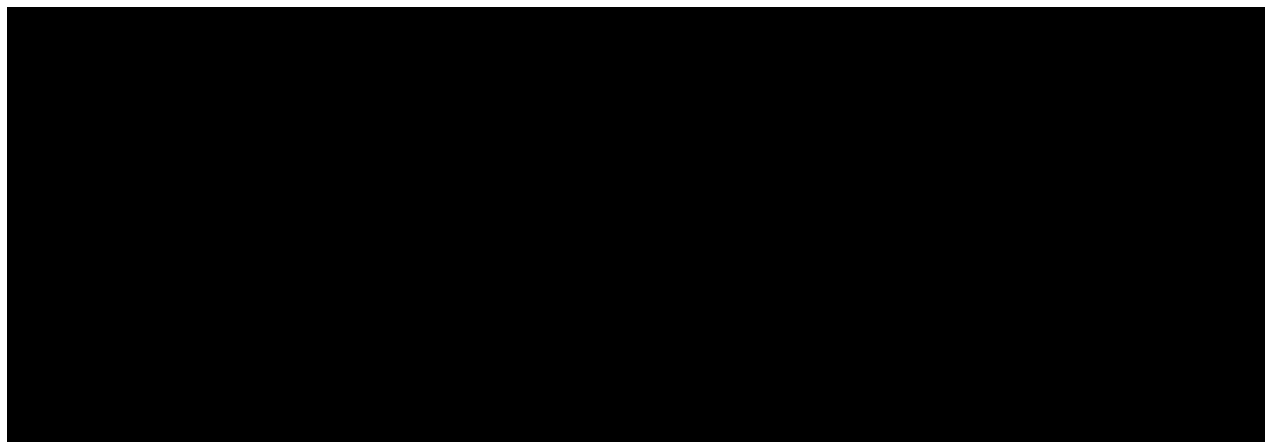
5.3.3 *Patient 2 Study (helical)*

The representative CT images of Patient 2 reconstructed using both FDK-based algorithm and MBIR are shown in Figure 5-8. As expected, the CT images reconstructed using FDK-based algorithm with low dose data (9 mAs) is much nosier and more bias than the image using MBIR algorithm. The corresponding PET images (*see Figure 5-8*) show a similar uptake in the MBIR-based CT-AC images and the FBP-based CT-AC images. The bias in the suspected PET lesion #2 images was -12% using the ULD-FBP-CT image, and 5% for using the ULD-MBIR-CT image. The bias of the mean uptake for the liver ROI was -31% and -29% when using the ULD-FBP-CT, and ULD-MBIR-CT images. The quantification results are shown in Table 5-3.
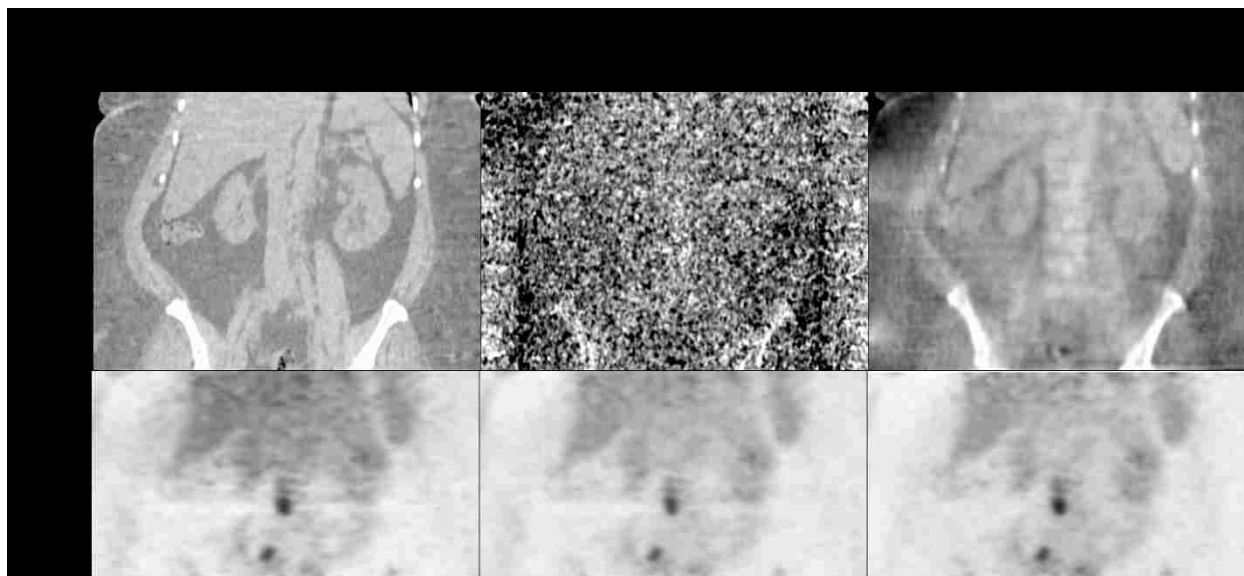
Figure 5-8. High and low-dose CT images and their correspondent PET images from the Patient 2 study

The window level for all CT images were set on [-500, 700] HU (top row). The window level for all PET images were set on 6 SUV with the size of 12 (bottom row).
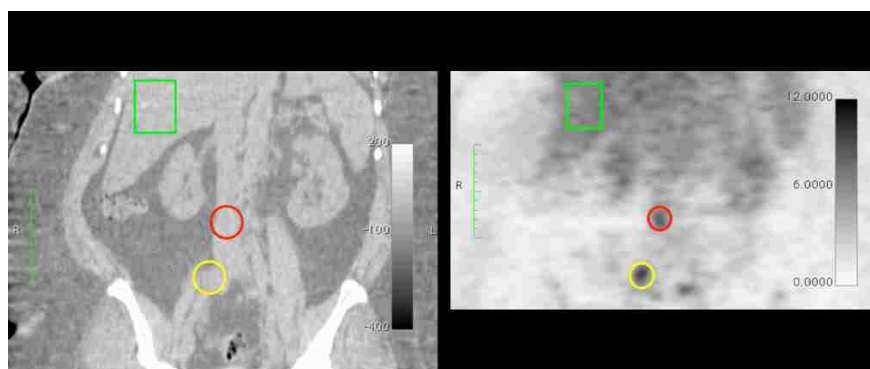
Figure 5-9. Representative ROI positions for patient 2 in Table 5-3

Table 5-3. The quantitative measurement for the ROIs selected on CT and PET images from patient 2
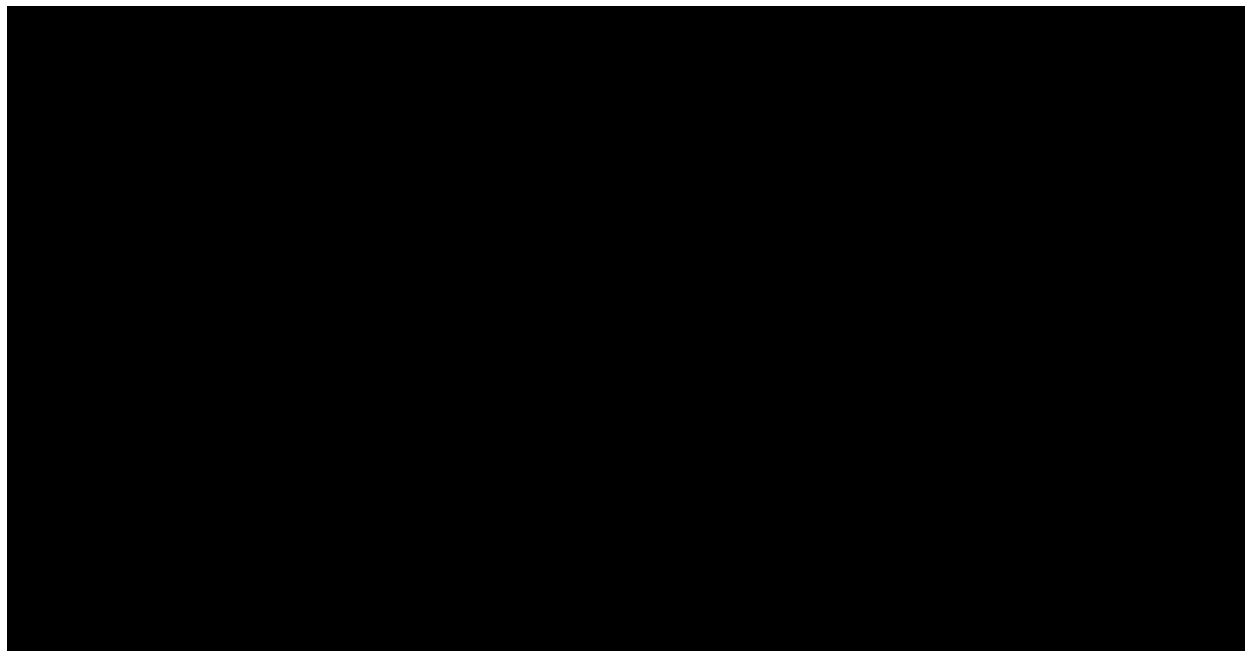
5.4 DISCUSSION

We acquired PET/CT scans of an enhanced RSD torso phantom using a diagnostic CT protocol (80 kVp 200 mAs) and an ULD protocol (80 kVp 5 mAs, lowest possible CT dose). FDK-based analytical reconstruction and MBIR are used to reconstruct the images. All three CT images were used for attenuation correction of the PET data which were reconstructed using OSEM. The FBP-CT and OSEM-PET images for the diagnostic CT protocol (80 kVp 200 mAs) were non-remarkable, while for the ULD protocol (80 kVp 5 mAs) artifacts were evident in the FBP-CT and OSEM-PET images. For the MBIR-CT and OSEM-PET images from the ULD protocol data, artifacts in the CT and PET images were suppressed but not removed entirely. For a large central region of interest (ROI), the bias in the PET images was -25% using the ULD-FBP-CT image, and -11% for the ULD-MBIR-CT image. The std. dev. for the PET image ROI was 529, 659, and 610 Bq/ml when using the FBP-CT, ULD-FBP-CT. For the ultra-low dose acquisition, the noise and

bias in the CT image can propagate to the PET image through the attenuation correction step. In this phantom study, we showed that using MBIR for ULD CT data reduces bias and noise in the corresponding PET image. This approach has the potential to enable extended-duration CT scanning for matching respiratory-gated CT attenuation correction.

Likewise, the low dose limit of the CT scans for PET attenuation correction purpose is evaluated on two patient data sets. For the Patient 1 study, a CT scan at 54 mAs was used as the reference image for comparison. An ultra-low-dose CT scan at 5 mAs was also performed for the same patient. We further lowered the dose by reducing the sampling of the fully sampled data set to generate three sparsely sampled data sets at 0.21 mAs, 0.12 mAs, 0.06 mAs. FDK and MBIR are used to reconstruct the CT images used for CTAC. Quantitative measurement on the selected ROIs are performed on both CT and PET images. At ultra-low-dose, MBIR shows great advantage in terms of reducing the noising and suppressing the aliasing artifacts due to sparse sampling. The quantitative measurement on both the central heart region and lung region confirms this. However, the dose might still be too low to ensure the quantitative accuracy of the PET images for this patient, especially for the lung region, the bias is more than 15% for both MBIR and FDK based CTAC. These results are still very useful in terms of determining the possible practical ultra-low-dose scans for patient.

For the Patient 2 study, similar approaches were used for comparing the PET uptake value in the suspected uterine cancer lesion. Again, we could find a big improvement for the accuracy of CT ROIs when comparing the low-dose FDK CT image and the MBIR CT image to the reference high dose image in lesion #2 (bias: 3579% vs. -1091%). However, this improvement did not fully reflect

on the accuracy of the correspondent PET image (bias: -12% vs. 5%). The possible explanation for it could be the 'truncated field of view' in the CT image lead by an oversize patient (BMI = 61.7). The Figure 5-10 shows the CTAC (PIFA, PET images for attenuation) images from the scanner, and we can see that all attenuation maps, especially for ULD images, were abruptly cropped due to the limited field of view of the bowtie. Lesion #1 was not included in the discussion is because of that an obvious white streak artifact across the lesion #1 is observed in the PET image, and it may affect the accuracy in its uptake (see streak artifact in Figure 5-8 PET images).
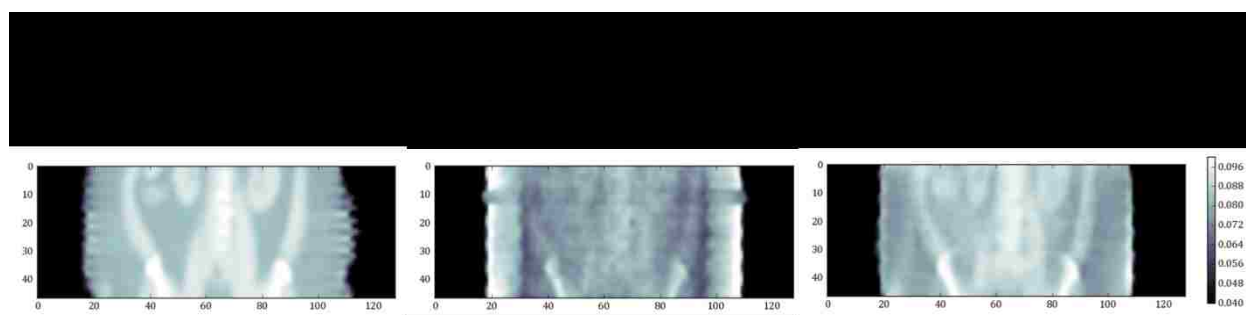
Figure 5-10. CTAC images (PIFA) for Patient 2 reconstruction

5.5 CONCLUSION

We explore the opportunity of using ultra-low dose CT images for PET attenuation correction while preserve the quantitative accuracy for the PET images. Although iterative reconstruction methods, model based iterative reconstruction (MBIR) in this study, are effective in reducing noise, suppressing streaking artifacts, and recovering the accuracy of the HU for low dose scans compared to the traditional FDK-based analytical reconstruction algorithms, there is still a dose boundary required in order to overcome the statistical bias. Besides, the truncated-FOV artifact is a critical bias factor especially for the ULD CTAC.

Chapter 6. LIMITS OF ESTIMATION FOR ULD-CT

6.1 MOTIVATION

Low-dose CT imaging is typically constrained to be diagnostic. However, there are applications for even lower-dose CT imaging, including image registration across multi-frame CT images and attenuation correction for PET/CT imaging. We define the ultra-low-dose (ULD) CT regime as a dose of a factor of 10 lower than current low-dose (~ 10mAs) CT dose levels. In the ULD regime it is desirable to use statistically-principled iterative reconstruction methods that make full use of the raw data information. Since most statistical-based reconstruction methods assume that noise distribution in projection images (post log) is nearly Poisson or Gaussian, our goal is to understand the statistical distribution shape of ULD CT data, and to determine the conditions that enable iterative reconstruction methods for attenuation correction in PET/CT imaging. Results indicate three general regimes for noise distribution in ULD CT projections: (1) Normal statistics, where post-log data are well modeled by normal distribution. (2) Skew statistics, where normal distribution remains a reasonable approximation and statistically-principled methods have an advantage. (3) An electronic-noise regime that is photon-starved and the quadratic approximation is no longer effective. For instance, a total integral attenuation of 4.8 (~24 cm of water) is the maximum post-log value where a definitive maximum likelihood value could be found for ULD projections using one particular X-ray technique, and it also indicate the fundamental dose limit in reconstructing ULD CT data when using standard data processing methods.

6.2 MODEL-BASED ITERATIVE RECONSTRUCTION WITH ASSUMPTION OF GAUSSIAN AND POISSON NOISE DISTRIBUTION

Concerns with CT dose have led to lower dose scanning protocols, often using statistically-principled (i.e. iterative) image reconstruction methods to suppress the effects of increased quantum noise[138]. These low-dose methods often assume that the projection data after the logarithm transform follow a Poisson or Gaussian distribution[93,134,139,140]. However, there are applications for even lower-dose CT imaging, including multi-frame (cine acquisition) CT image registration and attenuation correction for PET/CT[88,141]. Therefore, the aims of this study are twofold: 1) to determine whether ULD CT sinograms are normally distributed and how the different non-positivity corrections affect the distribution, and 2) to further determine the lowest radiation dose level that can reasonably be used so that normal-distribution-based iterative methods can be applied. The result may be informative for setting the minimum dose level for ULD CT scans and for estimating the HU bias in iterative reconstruction.

6.3 METHOD

We analyzed projection data obtained in the four experiments summarized below and described in more detail in sections 6.3.1 through 6.3.4. Simulation process for the data statistical distribution is summarized in Figure 6-1, and details of the simulation are described in sections 6.3.5 through 6.3.7.

Figure 6-1. Flow chart of the simulation process

We used the results of Experiments 1 and 2 with aluminum phantom to evaluate our poly-energetic cascade noise model and to compare different non-positivity correction methods; we then used the result of Experiment 3 and 4 with water phantom to simulate the signal distribution of projection data from different doses.

A.   Experiment 1: Empirical projection data after attenuation by an aluminum phantom. Three-dimensional (3-D) data were acquired in the form of multiple frames of two-dimensional (2-D) detector data using a clinical CT scanner and an aluminum phantom. X-ray techniques: 80 kVp; 50, 10, and 6 mAs.

B.   Experiment 2: Simulated projection data after attenuation by an aluminum phantom. One-dimensional (1-D) data were acquired in the form of multiple realizations of data from a single detector pixel by modeling the same clinical CT scanner, aluminum phantom, and X-ray techniques as used in Experiment 1.

C.   Experiment 3: Simulated projection data after attenuation by a water phantom. One-dimensional (1-D) data were acquired in the form of multiple realizations of data from a single-center detector pixel by modeling a water phantom scanned in the same clinical CT scanner as used in Experiment 1. X-ray techniques: 120 kVp; 200, 10, and 0.5 mAs.

D.   Experiment 4: Simulated projection data after attenuation by a water phantom, with reconstruction. Two-dimensional (2-D) data were acquired in the form of multiple frames of 1-D detector data (a single row of detector pixels) simulated by modeling a water phantom scanned in the same clinical CT scanner as used in Experiment 1. X-ray techniques: 120 kVp; 400, 50, 20, 10, 5.0, 3.5, 2.0, 1.0, 0.7, and 0.5 mAs.

6.3.1   *Experiment 1: Empirical projection data by an aluminum phantom*

This experiment was performed using a LightSpeed^{TM} VCT scanner (GE Healthcare, Chicago, IL). Using an X-ray tube voltage of 80 kVp, data were acquired using tube currents of 50 mA, 10 mA, and 6 mA; for each acquisition, 1640 projections were acquired over 1 second with no gantry rotation. We first acquired air data for each of the tube current settings, and then acquired data with a 7.18-cm-thick stack of aluminum plates placed in the center of the scanner. For each acquisition, we discarded the first 50 projections and included 8 center detector rows and 8 center detector columns for each of the remaining projections; hence, 101,760 realizations (1590 projections x 8 detector rows x 8 detector columns) of measured data were used from each acquisition.

6.3.2   *Experiment 2: Simulated projection data by an aluminum phantom*

Using the methods described in section 6.3.6, we simulated 1-D projection data for the same number of realizations that were generated in Experiment 1, using the same tube voltage and currents as for Experiment 1, transmission through air and through a 7.18-cm-thick aluminum phantom, and detected by a 1-pixel detector.

6.3.3   *Experiment 3: Simulated projection data by a water phantom*

Using the methods described in section 6.3.6, we simulated 1-D projection data for 20,000 realizations, using diagnostic-level (200 mAs), low-dose (10 mAs), and ultra-low dose (0.5 mAs) flux and various path lengths of water (1000 different thickness from 5 to 75 cm).

6.3.4 *Experiment 4: Simulated projection data by a water phantom, with reconstruction*

Using the methods described in section 6.3.6, we simulated 2-D sinograms (888 detector columns and 984 projected angles) using a 35-cm-diameter circular cylindrical water phantom at the center of the field of view. The "large" bowtie filter was included in the simulation. We simulated ten different dose levels: X-ray tube potential of 120 kVp; tube currents of 1.0, 1.4, 2.0, 4.0, 7.0, 10, 20, 40, 100, 800 mA, at 0.5-s rotation time.

Sinograms were then reconstructed into a 512 pixel x 512 pixel matrix using the iterative coordinate decent (ICD)–WLS method[142,143] for 10 iterations with 580-mm field of view. The highest-dose image (from the 400-mAs simulation) was used as a control for calculating the bias in the other, lower-dose images. Four combinations of electronic noise ($\sigma = 5, 15$) and weight estimation (W_Q, W_{Q+E}) methods were applied to all images, and only the water part of the reconstructed images were included in the region of interest for bias calculation; the thresholding was decided by Otsu's method[144] on the 400 mAs control.

6.3.5 *Simulation environment*

For all simulations, we used CatSim (ver. 5.6, GE Global Research, Niskayuna, NY) [129]; we modeled the scanner used in Experiment 1 above and we simulated projection data after attenuation by the phantoms described in Experiment 2 and Experiment 3 above. The X-ray spectra were generated using XSPECT (ver. 3.5c) and incorporated into CatSim. We used a 0.5 keV bin size for all spectra and attenuation simulations, with the peak energies of 80 or 120 keV. Source-to-detector and source-to-isocenter distance are 949.075 and 541.0 mm. Row and column size of the detector are set as 1.25 and 1.024 mm. Scatter was not included in our simulations, and beam hardening was not considered in Experiment 2.

6.3.6 *Poly-energetic cascade noise model*

A poly-energetic cascade noise model was used to simulate the CT signal distribution in this study[94,129]. The pre-log detector signal, s, was defined as:

$$s = G \cdot \{ \sum_{E=0.5keV}^{\max keV} P(C(E)) \cdot W(E)\} + N(0, \sigma^2)$$

where P is the Poisson function with the mean as the 'detected counts' (C, number of photons) integrated over the 0.5-keV-wide energy range centered on each energy E (keV), in 0.5 keV steps up to the peak energy of the spectrum. The weighting term (W) was set equal to the value of sub-energy for the energy-integrating detector. The gain factor (G) for converting photon counts to detector units was set to 0.0195 based on our previous results[145], the Gaussian electronic noise was set to a mean of 0 and a standard deviation of 15. The post-log p_i value in the attenuation domain was then calculated as $p_i = -\log(F(s)/A)$, where A is the air scan value and F is the non-positivity correction function which will be described in the following section.

6.3.7 *Non-positivity corrections*

For negative values in the pre-log projection data, three non-positivity correction methods were tested in this study: the flip method, the threshold (truncation) method, and part of the mean preserving filter (MPF) method. For the flip method, non-positive values of the pre-log signal were converted by simply taking the absolute value, and adding a small positive value to 0 values:

$$F(s) = \begin{cases} s, & s > 0 \\ \varepsilon = 10^{-3}, & s = 0 \\ -s, & s < 0 \end{cases}$$

For the threshold method, all non-positive values are replaced by a minimal value, ε, which is determined by calculating the attenuated intensity after passing through a possible maximum path length, L_{max}, (75 cm of water in this study).

$$F(s) = \begin{cases} s, & s > 0 \\ \varepsilon = I_0 \cdot exp(-\mu_{water} \cdot L_{max}), & s \leq 0 \end{cases}$$

The mean preserving filter (MPF) consists of two successive steps to enforce positive values by computing a new value through a function[133]: a non-linear converting process follow by an error dispersion process to distribute errors over two dimensions in the projection images. The α is set at 20 based on the previous study[146]. Since Experiments 1 through 3 are 1-D statistical distribution studies, we can only consider the first non-linear transform part of the MPF process and therefore we designate this method as MPF'.

$$F(s, \alpha) = \begin{cases} s, & s > \alpha^2 \\ \alpha \cdot \log\left(exp\left(\frac{s}{\alpha}\right) + 1\right), & s \leq \alpha^2 \end{cases}$$

6.3.8 *Normality test: Kolmogorov-Smirnov statistic*

The Kolmogorov–Smirnov (K–S) distance (D_{max}) describes a normalized distance (from 0 to 1) between a given sample distribution and a reference normal distribution as a metric for describing the normality[147]. If the sample data is normally distributed, D_{max} will be close to zero. For a given cumulative distribution function (*CDF*) of p_i, D_{max} is:

$$D_{max} = MAX|CDF[\log(L(\hat{p}_i|p_i))] - CDF[N(mean(\hat{p}_i), \sigma(\hat{p}_i)^2)]|$$

where *MAX* is the maximum value of the set of distances. $\hat{p}_i$ represents the estimated attenuation for a measured p_i, and N is the normal function. All calculations for D_{max} value were performed using Python-3 with the SciPy library (SciPy.Org, ver.0.16.0).

6.3.9   *Quadratic approximation and WLS reconstruction*

To understand how non-normal likelihood distributions could bias the statistical-based reconstruction process, we compared log-likelihood profiles simulated with the poly-energetic cascade model to the weight-least square (WLS)-based log-likelihood profiles[134,142] in a simple quadratic approximation form:

$$\log(L(\hat{p}_i|p_i)) = -\frac{1}{2}W(\hat{p}_i - p_i)^2$$

The *W* term is the weight for estimating the inverse variance of the post-log signal:

$$W(p_i) = \frac{1}{Var(p_i)}$$

Using a first-order Taylor expansion, the variance of the post-log signal can be approximated in the form of pre-log signal intensity s_i as[138]:

$$Var(p_i) \approx \frac{1}{(\overline{s_i})^2}Var(s_i)$$

When assumed quantum noise (Poisson distribution) is the dominant factor in estimating the variance, and since $Var(s_i) = s_i$ for a Poisson distribution, the $W(p_i)$ can be simplified as: [134]

$$W_Q(p_i) = s_i$$

Thibault *et al.* proposed a combined quantum and electronic noise model when electronic noise (σ_e) cannot be neglected[133]:

$$W_{Q+E}(p_i) = \frac{s_i{}^2}{s_i + \sigma_e{}^2}$$

We also compared the simulated likelihood variance as the best variance estimation which a WLS model could get:

$$W_{Best}(p_i) = \frac{1}{Var(\hat{p}_i|p_i)}$$

6.4 RESULT

6.4.1 *Experiments 1 and 2: Distribution of projection data after attenuation by an aluminum phantom, empirical and simulated results*

In Experiments 1 and 2, as the X-ray tube current decreased from 50 mAs to 10 mAs and 6 mAs, for both empirical data (*see Figure 6-2, colored histograms*) and simulated data (*see Figure 6-2, black lines*), we found that as the dose was reduced, not only did the signal variance or bias increase, but also the shape of distributions gradually deviated more from a normal distribution, regardless of which non-positivity correction method was applied. The data from Experiment 2 (simulated using the cascade noise model) showed very similar distributions compared to the empirically obtained data from Experiment 1; hence, we will use this simulation model for Experiments 3 and 4. The true (with no noise) p_i in Experiment 2 is 5.77.
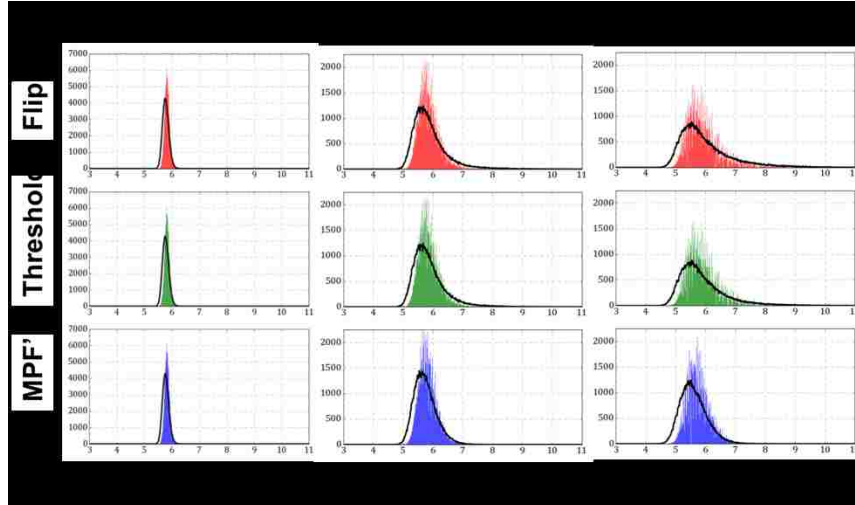
Figure 6-2. Histograms of post-log measurements by an aluminum phantom for empirical and simulated date

Histograms of 101,760 realizations of post-log measurements after attenuation by an aluminum phantom for empirical data (in colored regions) and simulated data (in black lines) at three different flux levels (tube currents of 50, 10, and 6 mAs) when using three non-positivity correction methods: (top) Flip method, (middle) Threshold method, and (bottom) Mean preserving filter without error dispersion process (MPF'). All histograms were generated with 1,000 bins from p_i = 2.0 to p_i = 14.0.

6.4.2   *Experiments 3 (water phantom simulation) results*

By combining histograms of simulated values including noise (p_i) for true attenuation $\hat{p}_i$, useful 2-D histograms can be generated. In the 2-D histograms of Figure 2A, vertical profiles are distributions of 20,000 simulated p_i values for each of the 1,000 true $\hat{p}_i$ values that were modeled, and horizontal profiles represent the likelihood function for each p_i. Comparing vertical profiles in the 2-D histogram, we found that the shape of distribution starts to deviate from the ideal normal histogram when $\hat{p}_i$ is greater than a certain attenuation level; for example, in Figure 6-3A, 0.5 mAs, the vertical profile of $\hat{p}_i$ = 2 looks very different from the vertical profile of $\hat{p}_i$ = 4. Furthermore, we found that p_i profiles become constant after passing a certain $\hat{p}_i$ value; for

example, profiles of 0.5 mAs in Figure 6-3A stabilize when $\hat{p}_i$ is greater than approximately 5. Figure 6-3B shows the likelihood profiles of the same post-log data for measured $p_i = 6$ acquired at three different dose levels. We found that the probability function becomes broader when the tube current decreases from 200 mAs to 10 mAs, but the maximum likelihood value remains constant at $p_i = 6$. Furthermore, we found that in the ULD CT regime (e.g. 0.5mAs), there is no peak value in the likelihood profile.
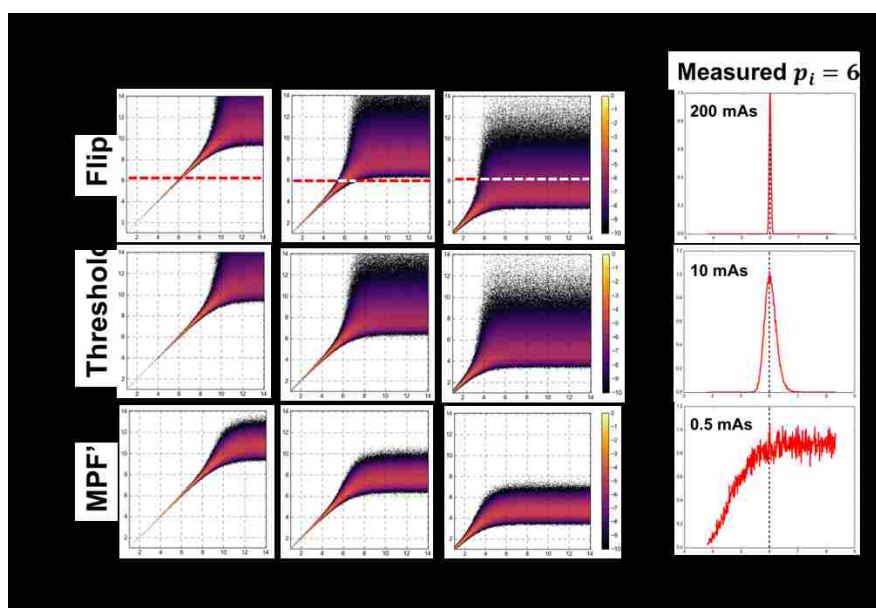
Figure 6-3. Two-dimensional histograms and representative likelihood profiles

(A) 2-D histograms of post-log signal (measured p_i) as a function of true $\hat{p}_i$ for diagnostic, low-dose, and ultra-low dose regimes. The horizontal axes are a function of the water thickness and the vertical axes are the distributions of simulated post-log attenuation values from 20,000 realizations for each plot. Histogram counts were normalized to the sum of realizations for each true $\hat{p}_i$ and shown on a $\log_{10}$ scale. (B) Likelihood profiles for a measured post-log attenuation of 6.0 (as indicated with dashed lines in part A) at diagnostic, low-dose, and ultra-low dose levels with 'Flip' non-positivity correction.

6.4.3 *Experiments 3: Estimation bias of WLS quadratic approximation*

Figure 6-4A shows likelihood profiles with 0.5 mAs tube current over the true $\hat{p}_i$ range of 2.0 to 5.0. The shape of profiles changes from a narrow, symmetrical, normal-like distribution (*in red*) to broader and increasingly skewed distributions (*in green and blue*). As the measured p_i increases, like the observation shown in the Figure 6-3B, the profile shows a "likelihood plateau" which for no maximum likelihood value can be found (*in magenta*). The estimation bias of WLS quadratic approximation is presented by overlapping the log likelihood profiles in Figure 6-4B (*in orange*) with quadratic approximated profiles, which are described in section 6.3.9. All three quadratic approximation approaches give very good estimation for likelihood functions when measured p_i is relatively small (e.g. 2.0). The quantum noise model (*in blue*) shows an underestimation in variance of the likelihood function when the measured p_i increased to 3.0. All three approaches (*in blue, green, and magenta*) greatly deviated from the simulation profiles when measured p_i is greater than 4. By repeating the same analysis with different $\hat{p}_i$ numbers and subtracting the simulation data with quadratic estimations, we can get 2-D difference maps for showing log-likelihood bias of WLS approaches (*see Figure 6-5A~C*). Figure 4D shows three relative weight estimations which were used in this approach.
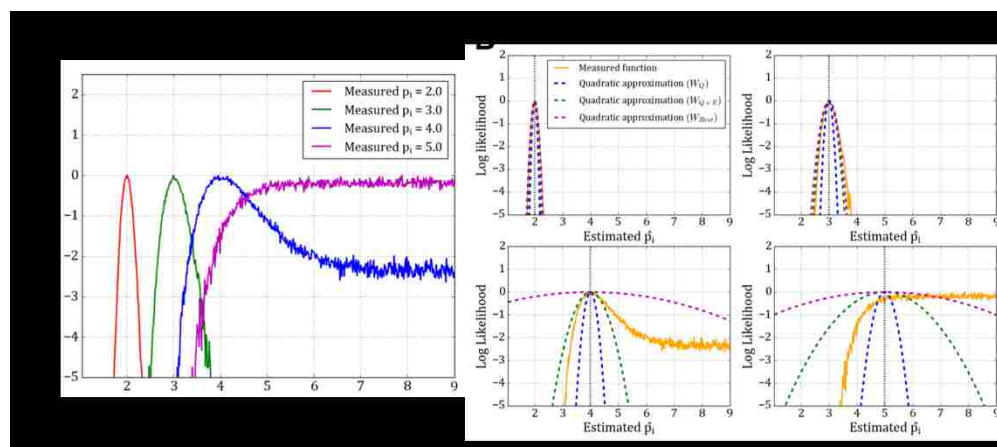
Figure 6-4. Log-likelihood profiles for measured attenuation

(A) Log-likelihood profiles for measured attenuation p_i of 2.0, 3.0, 4.0, and 5.0 in 0.5-mAs ULD data with 'flip' non-positivity correction. (B) Profiles of measured post-log signal (in orange) as described in (A), measured $p_i = 2 \sim 5$, with correspondent quadratic approximations (in dotted line). Three estimated weights were tested here: quantum noise-only estimation (W_Q, in blue), quantum and electronic noise estimation (W_{Q+E}, in green), and the true measured variance (W_{Best}, in magenta).
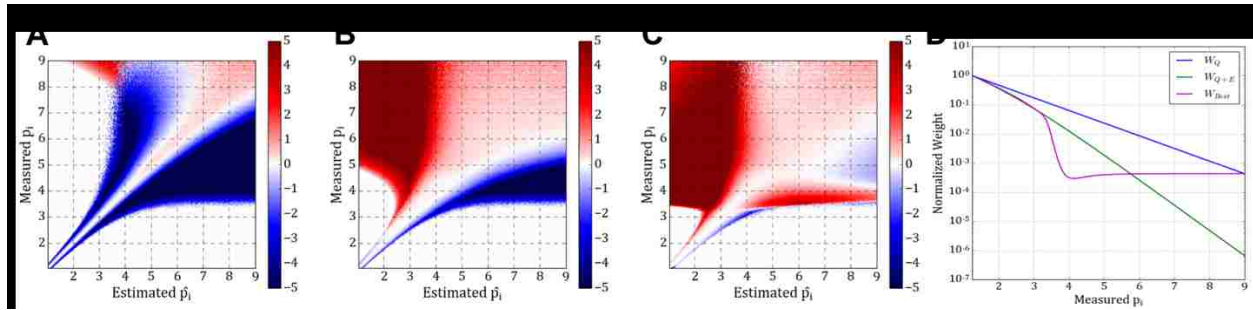
Figure 6-5. 2-D Histograms of log-likelihood differences

Log-likelihood differences between quadratic approximations (A: W_Q, B: W_{Q+E}, C: W_{Best}) and poly-energetic cascade noise model simulated data for 0.5mAs ULD levels with 'flip' non-positivity correction. The red color indicates overestimation and the blue color indicates underestimation of the log-likelihood function by the quadratic approximation approaches. (D) Estimated and simulated weights (W_Q in blue, W_{Q+E} in green, and W_{Best} in magenta) as a function of measured post-log p_i, with data normalized at $p_i = 1.25$.

6.4.4 Experiments 3: Limitation of likelihood estimation

Knowing that the likelihood distribution evolves from a normal distribution to a skewed distribution to a plateau distribution as the attenuation value becomes greater, we can delineate the maximum normal-distributed p_i and the maximum estimable p_i through a normality test and ML value analysis. The deviation to the normal distribution for different measured p_i could be monitored through measuring the D_{max} value by the *K-S test* (*see Figure 6-6A*). We assumed that a steep rise in the D_{max} value represents the regime where the likelihood function of measured p_i starts greatly deviating from the normal distribution, and thus implies a possible bias when using

the quadratic approximation. Besides, the high D_{max} value at around $p_i = 1.5$ are the boundary effect where the histogram binning process in the cascade noise simulation didn't fully cover the lower end of the distribution, and it will not affect locating the normality deviation point here. A decrease of the D_{max} values could be seen after the value has peaked, and this is because the K-S statistics fails when the distribution is no longer in a closed form (*see* blue and magenta lines in *Figure 6-4A*). On the other hand, a maximum estimable p_i could be defined by locating a p_i value where the maximum likelihood value could no longer be found and reach a "likelihood plateau" as we described in the previous section. In Figure 6-6B, by putting all maximum likelihood values of measured p_i together, the measured p_i where its maximum likelihood value is not a random value could be pointed out (*red arrow*). By smoothing and finding the highest 1st derivative, the maximum normally-distributed and estimable measured p_i boundaries could be delineated by repeating the same analysis in different flux levels and with different non-positivity correction methods as shown in Figure 6-7A~C. Figure 6-7D gives the information of the equivalent water thickness for the ideal measured p_i.
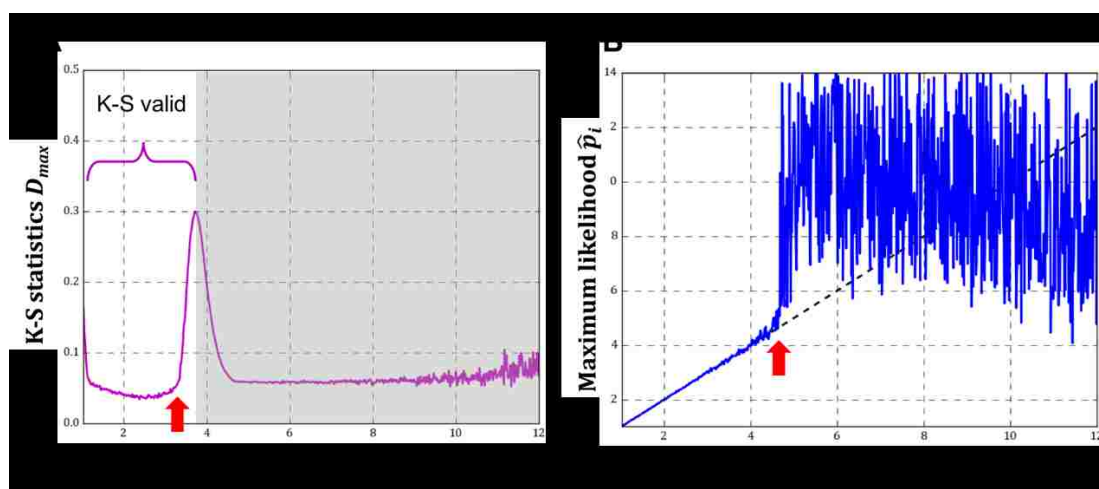
Figure 6-6. Normality and maximum likelihood estimation as function of the noisy signal
Normality and maximum likelihood estimation as function of the noisy p_i for 'flip' non-positivity correction and ultra-low dose level (120kVp, 0.5mAs). (A) CDF maximum distance (D_{max}) of

Kolmogorov-Smirnov statistic as a function of noisy p_i. **(B)** *Maximum likelihood* $\hat{p}_i$ *value as a function of measured* p_i *values. The **red arrow** labels huge gradient* p_i *point for the change of normality and maximum likelihood values.*
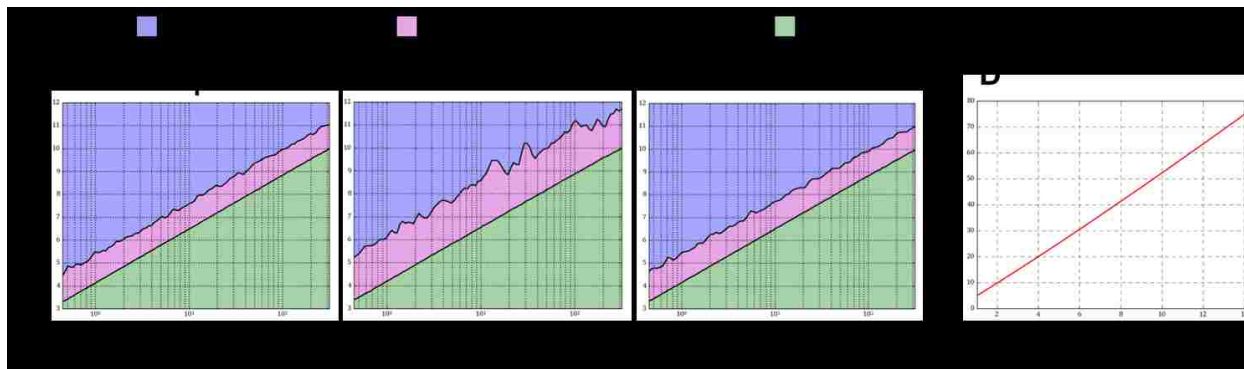
Figure 6-7. Maximum estimable attenuation and the maximum normality deviation point

Maximum estimable p_i *(**upper line**) and normality deviation point (**lower line**) for measured* p_i *of center element in the detector as a function of source intensity shown in the* log_{10} *scale; sinogram levels could be segmented into three regimes: electronic noise regime (**in blue**), skewed distribution statistics regime (**in red**) and normal distribution statistics regime (**in green**). Noisy signal was pre-processed with (A) Flip, (B) Threshold, and (C) MPF' non-positivity corrections. (D) The noisy attenuation (*p_i*) and its correspondent ideal water thickness with 120 kVp radiation source.*

6.4.5   *Experiments 4: Parameterize bias with abnormality*

From previous results, we learned that the likelihood distribution could greatly deviate from the normal distribution, and we expected it could also lead bias in the reconstructed image. With considering the bowtie conformation for calculating the skew and plateau statistics boundaries for detector unit (*as shown in Figure 6-8*), in Figure 6-9, normalized biases of iterative reconstructed image were shown in the function of source flux level (mAs) and non-Gaussian fraction (%) with different settings of electronic noise ($\sigma = 5, 15$), non-positivity correction (Flip, Threshold, MPF') and weight estimation method (W_Q, W_{Q+E}). Overall, bias increased as the source intensity

decreased, and the trend of bias changed as different settings were applied. However, the trends became very similar when biases were shown with non-Gaussian fractions for all cases tested in this study. The bias increased sharply when around 55% of sinogram pixel values were in the skew distribution statistics or electronic noise regimes.
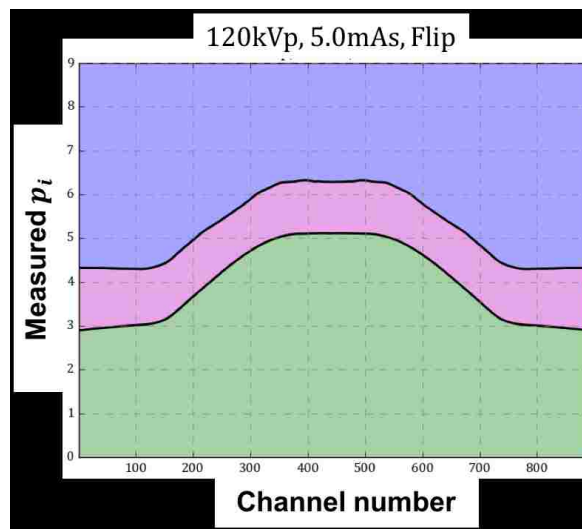
Figure 6-8. Maximum estimable attenuation and the maximum normality deviation point with considering the bowtie filter

*Maximum estimable p_i (**upper line**) and normality deviation point (**lower line**) for measured p_i of center element in the detector as a function of channel number; sinogram levels could be segmented into three regimes: electronic noise regime (**in blue**), skewed distribution statistics regime (**in red**) and normal distribution statistics regime (**in green**). Noisy signal was pre-processed with Flip non-positivity correction under 120 kVp, 5mAs of the radiation source.*
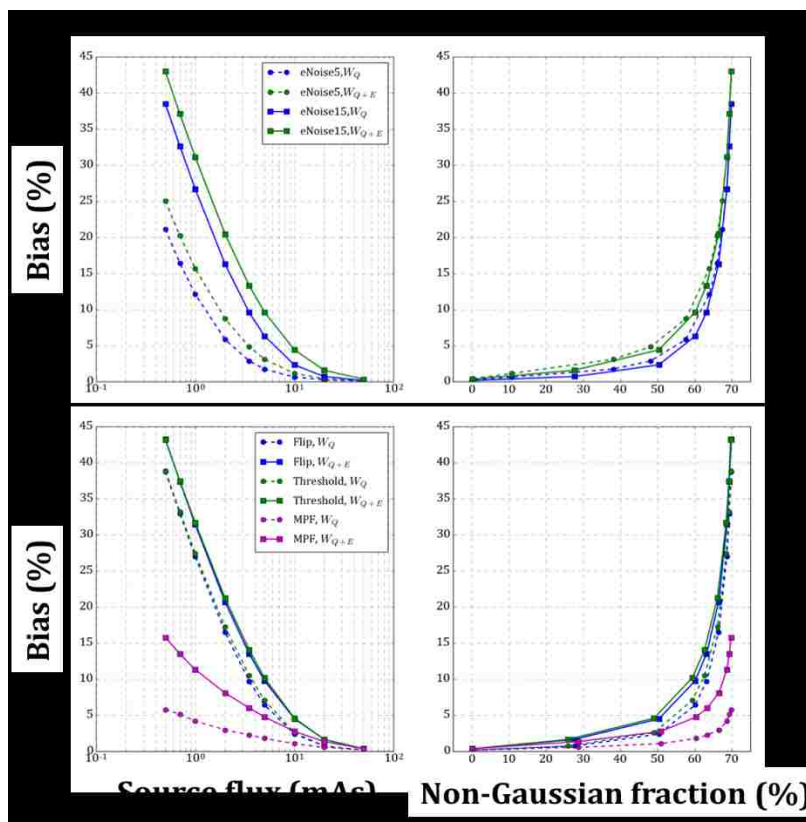
Figure 6-9. Bias of weight-least-squared reconstructed image of 35-cm water phantom

Bias of weight-least-squared reconstructed image of 35-cm water phantom as a function of source flux level and sinogram pixel skew fraction. (A) For two different electronic noise levels (dotted line: $\sigma = 5$, solid line: $\sigma = 15$) and two weight estimation settings (Blue: W_q, Green: W_{q+e}). 'Flip' non-positivity corrections were applied. (B) For three different non-positivity correction methods and two weight estimation settings. The electronic noise level (σ) was set as 15.

6.5 DISCUSSION

In this study, measured data showed that the post-log attenuation distribution is skewed when using a low-dose (6 mAs) protocol, and the multi-energetic cascade noise model simulation also showed similar skew-distribution shapes. The mismatch in Figure 6-2 could partly cause by "data discretization", which means low intensity values in the pre-log detector measurements were limited by quantization precision determined by the least significant bit in the detector's analog-

to-digital converter. In addition, the difference could be also caused by scatter or the imperfect estimation for detector's gain factor and efficiency.

For an even lower dose protocol (<1 mAs), 1-D simulated distribution of the post-log data of various water thicknesses were used for likelihood analysis. As measured integral attenuation increased, its likelihood distribution changed from a narrow normal distribution, to a positive skewed distribution, then to a steady plateau. A similar "likelihood plateau" could also be observed in previous mono-energetic noise model simulations[135,148]; also, the same trend of distribution change could be seen in all three non-positivity correction methods tested in the study. Mismatches between simulated log-likelihood data and WLS data suggested that iterative reconstruction algorithms based on WLS may not be optimal for ULD imaging even if the 'true' likelihood variance (W_{best}) was used for estimating the weight. The quadratic approximation approach may cause bias on ULD data because it cannot reflect the skewed and plateau distributions in the log-likelihood function. For ULD CT imaging, in addition to pursuing better weight estimation methods, the mismatch on the 2-D histogram here implies that the distribution shape change in ULD data also needs to be addressed.

The limits for normal-distributed estimation and for ML estimability can be derived by measuring the change of D_{max} and ML values on the likelihood function: for diagnostic dose level (200 mAs), almost all tested data, for water thickness smaller than 50 cm, were normally distributed. For low-dose scans (10 mAs), data were skewed when noisy $p_i > 5.5$ (~27 cm of equivalent water thickness) applied; a maximum-likelihood (ML) method could still find the peak value although the likelihood bias starts to show. The likelihood function will be further dominated by electronic

noise when the noisy p_i is larger than 7.6 (~40 cm of equivalent water thickness). In even lower ULD scans (0.5 mAs), data were skewed when $p_i > 3.4$ (~15cm of equivalent water thickness), and with p_i over 4.8 (~ 24 cm of equivalent water thickness), distributions were determined solely by electronic noise where likelihood distribution reached a plateau and no ML value could be found. The normality and ML boundaries further explained the reason why normal-based iterative approaches will not work on most of the ULD CT imaging. More importantly, it could be used as a look-up table for determining the limit of radiation dose level for the scan to avoid abnormal statistics in the reconstruction process.

The 1-D nature of the simulation model used here limits its application on the 2-D sinogram directly, and also restricts it from analyzing other more complicated non-positivity correction techniques, which require neighboring information, like adaptive trimmed mean filter (ATMF)[90]; however, considering the attenuation from the bow-tie filter, it is possible to approximately evaluate the non-Gaussian level on the sinogram and to compare it to the corresponding WLS reconstructed image. Bias increases sharply as about 55% of sinogram values were above the skew statistics line, therefore, the result further demonstrated that the skew and plateau likelihood statistics in the ULD acquisitions is one critical factor that causes the bias in the current statistical-based reconstruction approach. For future application, we expect that a more accurate iterative reconstruction method for ULD CT data could be achieved if the skewed and plateau likelihood distribution could be considered.

6.6   CONCLUSION

Low-dose CT projection data distributions can deviate substantially from a normal distribution in the low-dose regime and especially in the ultra-low dose regime, leading to a practical limit for

most statistical-based approaches when applied to ULD imaging. Furthermore, we identified integral attenuation values that lead to skewed and plateau likelihood distributions for a current clinical scanner, these limits represent water thicknesses where, at the X-ray techniques evaluated, bias in image-domain becomes evident and where the image noise begins to be dominated by electronic noise rather than quantum noise. These findings might assist researchers in selecting the lowest reasonable dose level for ultra-low dose CT scans for applications such as PET-CT attenuation correction, and they might also be useful for developing new reconstruction approaches that are more suitable for conditions when CT projection data contain non-Gaussian statistics.

6.7   SUPPLEMENTARY DATA

6.7.1   *Statistical distributions at different processing steps*

Figure 6-10 shows the distributions for 20K realizations for 35 cm of water. The data in the intensity domain are symmetric with a mean close to the truth. After non-positivity transformation, asymmetry is evident in the low-dose and ultra-low dose regimes. After the log transformation, both the low dose and ultra-low dose settings have skewed distributions, and the latter also display a large bias from the truth. The diagnostic regime data behaves as expected.
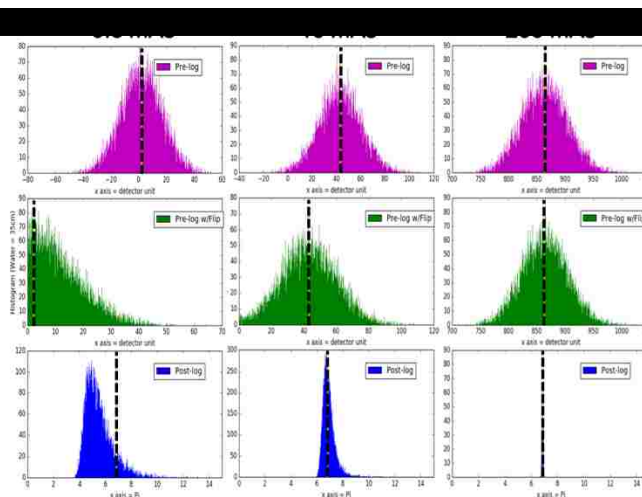
Figure 6-10. Histogram of 20,000 realizations of 1D-single detector model at three processing stages

*top pre-log raw signal in intensity domain (detector unit), **middle** pre-log raw signal with non-positivity correction, and **bottom** after taking logarithm with air-scan in attenuation domain. Ideal values were indicated with vertical line.*

6.7.2   *K-S statistics at different processing steps*

Figure 6-11 shows the K-S distance D_{MAX} but now as function of the water attenuation thickness. Distributions without non-positivity correction in the intensity domain are all very close to zero (<0.01) D_{MAX} indicating a normal distribution. With the non-positivity correction, D_{MAX} increases rapidly at approximately 20, 35, and 51 cm of water attenuation for the ultra-low-dose, low-dose, and diagnostic regimes. After the log transformation, the increase in D_{MAX} occurs for thinner layers of water, but with a more gradual transition.
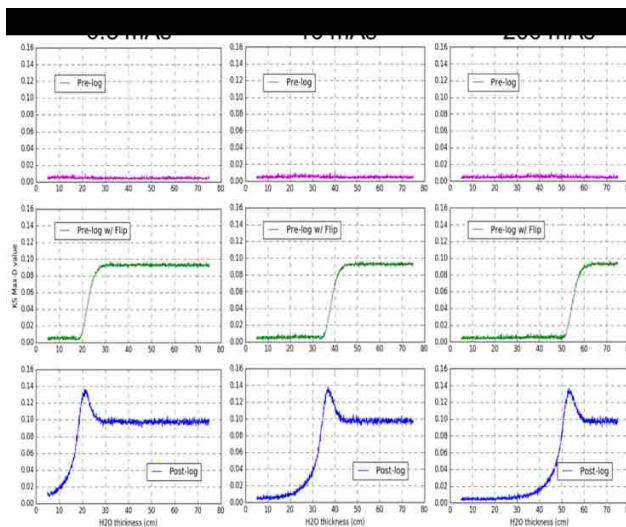
Figure 6-11. K-S statistics as a function of water thickness at three processing stages
*Kolmogorov–Smirnov distance D_{MAX} as a function of water thickness in the 1D-single detector model (20,000 realizations) with the ultra-low-dose, low-dose, and diagnostic regimes and three processing stages: **top** pre-log raw signal in intensity domain (detector unit), **middle** pre-log raw signal with "flip" non-positivity correction, and **bottom** after taking logarithm with air-scan in attenuation domain.*

6.7.3   *Bias of signal distribution in three dose levels*

By comparing the true $\hat{p}_i$ with the measured $\hat{p}_i$ of the distributions (Figure 6-12), one can see the bias starts to show around P_i = 4, 7, and 10 (water thicknesses of 20, 35, and 52 cm). Splitting mode, median and mean values also imply that the distribution of measurements are skew.
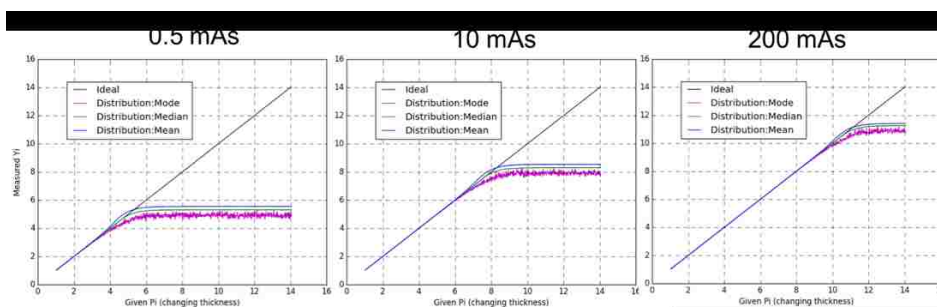
Figure 6-12. Bias of signal distribution in three flux levels

The black line represents the ideal (unbiased) correlation between true attenuation and the measured attenuations. The mean, median, and mode values, are shown in blue, green, and magenta color lines

6.7.4   *Distribution profiles of ultra-low dose signals*

The distribution profiles (Figure 6-13) for the ultra-low dose regime (0.5 mAs) reveal that a positive skewness starts to appear between 15.5 and 22.5 cm of the water thickness.
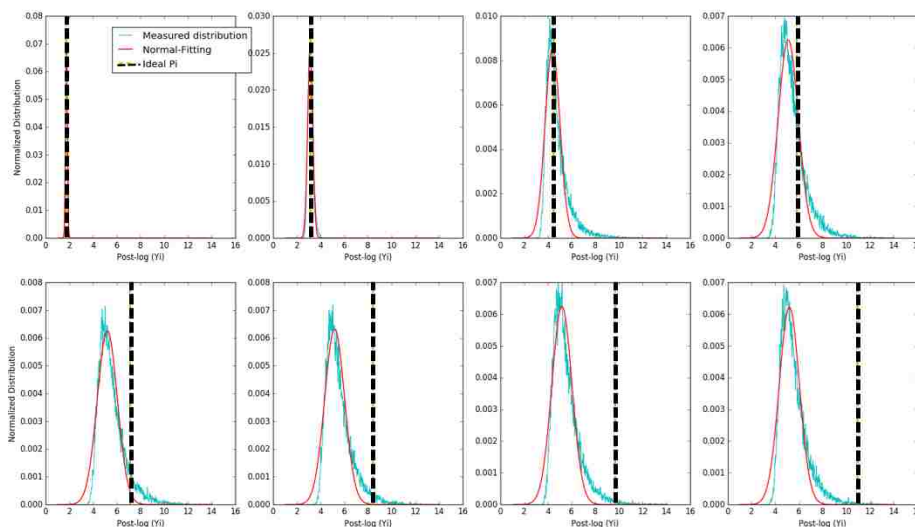
Figure 6-13. Distribution profiles of 0.5 mAs flux setting with different water thickness
Left to right, top to bottom: *8.5, 15.5, 22.5, 29.5, 36.5, 43.5, 50.5, 57.5cm. The cyan line represents the normalized histogram, and the red line shows the least-square normal fitting for the profile. The black vertical line indicates the ideal attenuation value.*

6.7.5   *Likelihood profiles of ultra-low dose signals*

The horizontal profiles in Figure 6-3 correspond to likelihood functions. Figure 6-14 shows likelihood distributions for the ultra-low dose (0.5 mAs) regime, and the ability to find a maximum likelihood disappears between measured attenuation = 4.5 ~ 5.8.
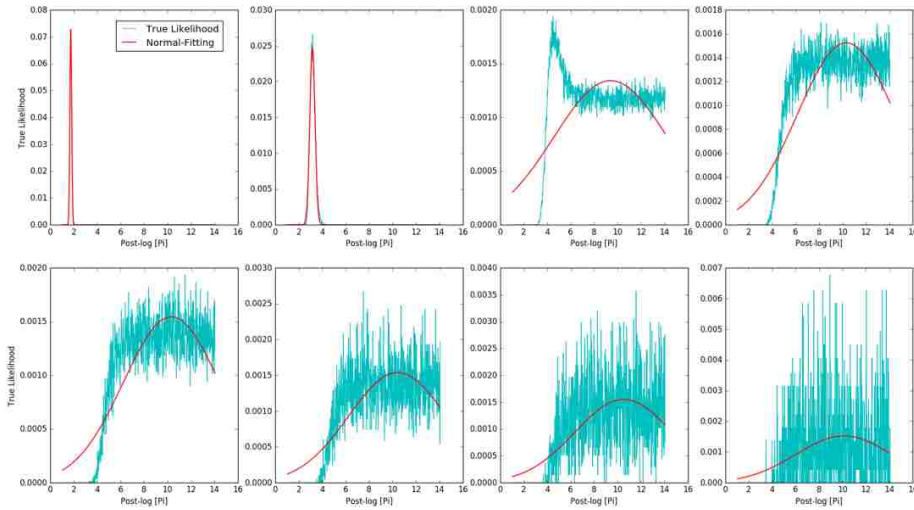
Figure 6-14. Likelihood profiles of 0.5 mAs flux for different measured attenuation

Left to right, ***top to bottom****: measured attenuation = 1.7, 3.1, 4.5, 5.8, 7.1, 8.4, 9.7, 11.0. The cyan line is the likelihood profile of the measured attenuation and the red line shows least-square fittings to the normal distribution.*

Chapter 7. POTENTIAL FUTURE DIRECTIONS

7.1 ADD THE SKEW LIKELIHOOD CORRECTION TERM IN THE IMAGE RECONSTRUCTION ALGORITHM

7.1.1 *Methods*

In Chapter 6, data showed the log likelihood distribution could gradually deviate from the Gaussian distribution and then reach a likelihood plateau as source flux level kept decreasing. Moreover, in section 6.4.3 we showed that the weight-least-square approximation approach, which is commonly used in the model-based iterative reconstruction algorithm, may cause certain level of bias since it doesn't consider the shape change of the likelihood distribution in its approximation. Therefore, the next question will be: is it possible to add the 'skew-shape' correction term into the reconstruction algorithm?

Here I use the ICD-WLS reconstruction algorithm without the penalized term for showing the example[143,146], again, the cost function is defined as:

Eq. 1

And iterative coordinate descent (ICD) approach (as in Eq. 2) is applied for the optimization through Newton-Raphson method (as in Eq. 3, Eq. 4):

Eq. 2

$$\mu_j^{(n+1)} = \underset{\mu_j^{(n+1)} \geq 0}{\operatorname{argmin}} C\left(\mu_1^{(n+1)}, \cdots, \mu_{j-1}^{(n+1)}, \mu_j^{(n+1)}, \mu_{j+1}^{(n)}, \cdots, \mu_J^{(n)}\right)$$

$$\text{Eq. 3}$$

$$\rightarrow \frac{\partial C(x)}{\partial x}\bigg|_{x=\mu_j^{(n+1)}} = C'(\mu_j^{(n)}) + \left(x - \mu_j^{(n)}\right)C''(\mu_j^{(n)})\bigg|_{x=\mu_j^{(n+1)}} = 0$$

$$\therefore C'(\mu_j^{(n)}) = -\sum_i W_i l_{ij}\left(p_i - \hat{p}_i^{(n)}\right)$$

$$\therefore C''(\mu_j^{(n)}) = \sum_i W_i l_{ij}^2$$

So that we can get the updated image pixel value in iterations:

$$\text{Eq. 4}$$

$$\mu_j^{(n+1)} = \mu_j^{(n)} - \frac{C'\left(\mu_j^{(n)}\right)}{C''(\mu_j^{(n)})} = \mu_j^{(n)} + \frac{\sum_i W_i l_{ij}\left(p_i - \hat{p}_i^{(n)}\right)}{\sum_i W_i l_{ij}^2}$$

And the updated sinogram value in iterations as:

$$\text{Eq. 5}$$

$$\rightarrow \mathbf{p}^{(n+1)} = \mathbf{p}^{(n)} + l_{*j}\left(\mu_j^{(n+1)} - \mu_j^{(n)}\right)$$

where μ is the linear attenuation coefficient on the image, p is the attenuation value on the sinogram, F is the system matrix, W is the weight term, l is the pixel-based forward projector, n is the iteration number, and i and j represent index number on the sinogram and the image domain.

The objective for this modification is to add a correction term in Eq. 4 for showing the positive-skew likelihood distribution in the reconstruction process. For convenience, here we called the correction term as skew-likelihood correction (SLC) term, α, and it could be defined as:

$$\text{Eq. 6}$$

$$\alpha_i\left(m < 1, \varepsilon, p_i, \hat{p}_i^{(n)}\right)$$

$$= \begin{cases} \varepsilon(i, p_i) \in eletronic\ noise\ regime \cap \left(p_i - \hat{p}_i^{(n)} < 0\right) \to \alpha_i = m \\ \varepsilon(i, p_i) \in skew\ statistics\ regime \cap \left(p_i - \hat{p}_i^{(n)} < 0\right) \to \alpha_i = 1 \sim m \\ else \to \alpha_i = 1 \end{cases}$$

where ε is the sinogram index-dependent function as shown in Figure 6-8 for categorizing the statistical regime of the measured p_i if $p_i - \hat{p}_i^{(n)} < 0$; m is the maximum correction value, which is always smaller than 1 (e.g. 0.5). α will be interpolated between 1 and m by the distance between measured p_i and two boundary values if $\varepsilon(i, p_i)$ is in the skew statistics regime. With SLC term α, the Eq. 4 could be adapted as:

Eq. 7

$$\mu_j^{(n+1)} = \mu_j^{(n)} - \frac{C'\left(\mu_j^{(n)}\right)}{C''(\mu_j^{(n)})} = \mu_j^{(n)} + \frac{\sum_i \left(W_i l_{ij}\left(p_i - \hat{p}_i^{(n)}\right) \cdot \alpha_i\right)}{\sum_i W_i l_{ij}^2}$$
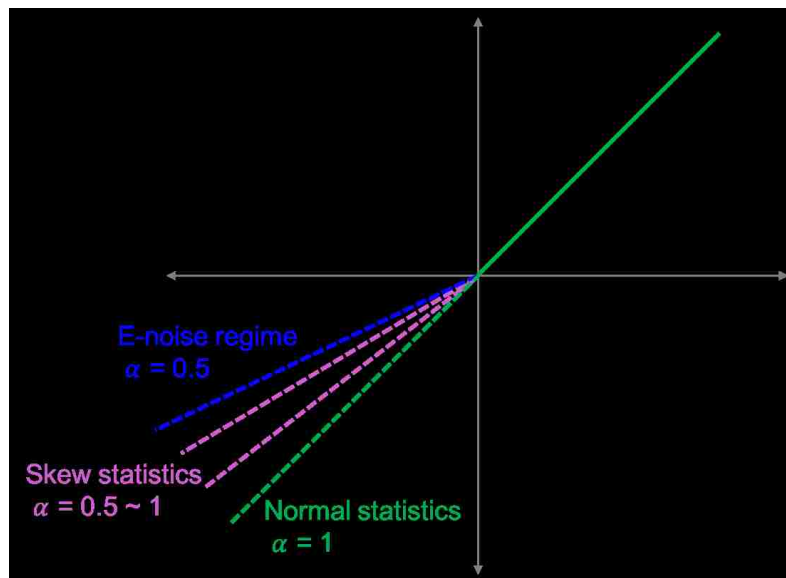
Figure 7-1. Representative image for the skew-likelihood correction with maximum $\alpha = 0.5$

The regimes of normal statistics, skew statistics, and e-noise were determined based on the measured Pi, source flux level and the corresponding detector channel number

On the other hand, the simulated log-likelihood variance could also be used as a look-up table (*see Figure 6-7 D*) for the estimated weighted term in the Eq. 7. In theory, the variance from the look-up table is the best variance estimation we could achieve, therefore, here I labeled W_{Best} for the look-up table weight estimation approach.

Four penalized weight least squared reconstruction (PWLS) image approaches were compared:

1. PWLS with quantum and electronic noise variance model (W_{Q+E})

2. PWLS with simulated likelihood variance model (W_{Best})

3. PWLS with quantum and electronic noise variance model (W_{Q+E}) and skew-likelihood correction term (SLC)

4. PWLS with simulated likelihood variance model (W_{Best}) and skew-likelihood correction term (SLC)

CT simulations with GE VCT scanner's settings were performed of the NCAT chest phantom using the CatSim simulator[129], which generates sinograms (984 views x 888 channel) with poly-energetic compound Poisson data (0.5 & 10 mAs and 120 kVp) and Gaussian electronic noise ($\sigma_e^2 = 15^2$) contributions. Only "Flip" non-positivity correction was evaluated. Ten iterations with optimized penalized terms (penalized constant was set at 10^{-5}) were used for each ICD-PWLS CT (512 x 512 pixels) reconstruction[134]. FBP image with 400 mAs flux level was used as the control group for calculating the bias.

7.1.2 *Preliminary results*
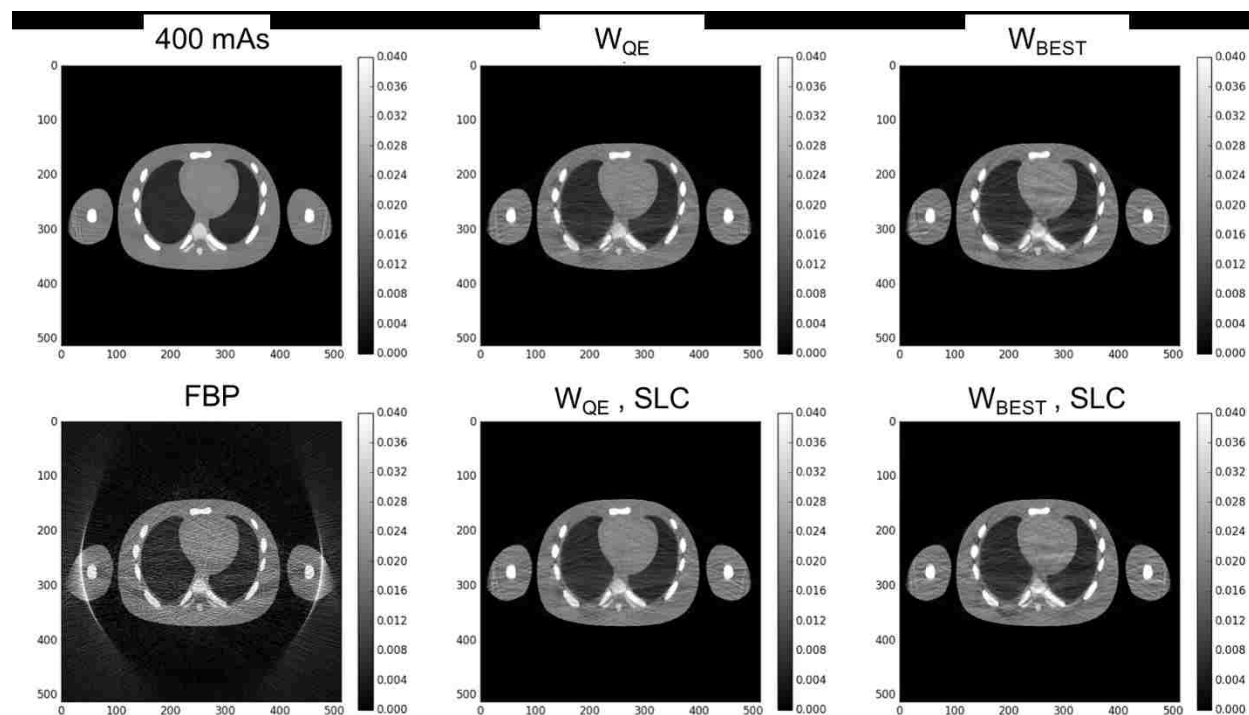
Figure 7-2. Skew-likelihood corrected (SLC) PWLS reconstruction of 10 mAs NCAT phantom simulation
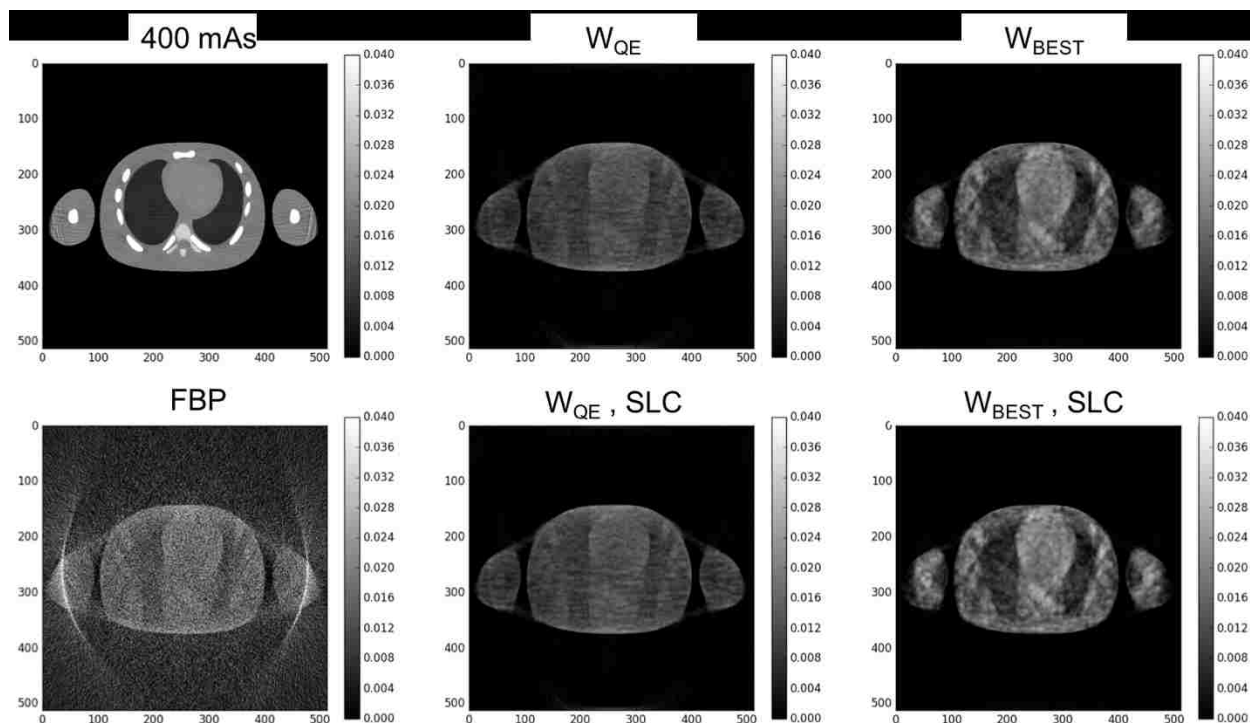
Figure 7-3. Skew-likelihood corrected (SLC) PWLS reconstruction of 0.5 mAs NCAT phantom simulation

Table 7-1. RMSE and mean bias of skew-likelihood-corrected PWLS NCAT reconstructions

7.2 TO CUSTOMIZE THE ULTRA-LOW-DOSE CT SCANNING PROTOCOL

In section 6.4.4, the data showed that the statistical distribution of the attenuation value (measured water thickness) in the sinogram could be categorized into three regimes for every given source flux level. In section 6.4.5, data further showed a strong correlation between the RMSE of the

reconstructed image and the non-Gaussian statistic percentage on the sinogram data. Therefore, one potential direction for this research is to use above information to create a customized ULDCT protocol for every patient in order to achieve the lowest but also reasonable dose deposition. With proper estimation of the attenuation path length for bone and lung tissues plus a prior information of the patient size from the CT scout scan or simply by measuring the chest circumference, a physician could potentially determine the most efficient low-dose protocol (in terms of HU accuracy) for each individual. In addition to the result in the section 6.4.5, we can also correlate the non-Gaussian statistic percentage to the 511-kev attenuation map so that the information could be directly used for determining the lowest CT flux level for generating the accurate attenuation correction map for the PET image.

7.3   THE TUBE PULSING APPROACH FOR THE ULD-CT ATTENUATION CORRECTION FOR PET

In section 4.1.3 and 5.3.2, researches had shown promising preliminary results of using the low-dose sparse-view CT images for producing the attenuation correction map for PET. This approach retains the total radiation dosage on the patient as the continues exposure approach by decreasing the acquisition view number while alleviating the electronic noise by increasing the source level at each view acquisition. However, one restriction for the technique is that the fast-switching (on and off x-ray source) scanning mode is not available on the current PET/CT scanner. The fast-kVp switching scanning mode (~50 microsecond) has been supported in some protocols for the dual-energy (80 and 140 kVp) CT imaging on some models[149]. Therefore, if we can keep increasing the public awareness on the issue of ULD-CTAC for the respiratory-gated PET, the manufacturer may consider equipping the fast-switching CT source which enables the tube-pulsing acquisition mode on the next-generation's PET/CT scanner.

Chapter 8. ORIGINAL CONTRIBUTIONS

This chapter summarizes original contributions in this thesis:

Comparison of different CT attenuation correction methods for the respiratory-gated PET[68] – With current clinical setups and the data processing stream, I compared six commonly-used 3D and 4D CT attenuation correction methods for the PET imaging under the respiratory motion. The phantom data showed that, for irregular breathers, the 4D-matched CT attenuation correction approach for the respiratory-gated PET is not the most accurate correction approach compares to 4D-MIP and 4D-EXH (end-exhale phase) attenuation correction method. The result indicates that the phase-mismatched artifact between the respiratory-gated PET/CT of the irregular breathers may cause the bias and it couldn't be solved by current phase-gating protocols (*see details in Chapter 2*).

Evaluation of a newly-proposed variance estimation model for reconstructing the ULDCT image[146] – Studies had shown that the model based iterative reconstruction method has many advantages for reconstructing the low-dose CT image in terms of noise and the bias. However, most of iterative reconstruction approach didn't consider the data variance change from the process of non-positivity corrections. Since negative values on the pre-log sinogram domain will be much more prominent in the ultra-low dose image, my colleague had proposed a new variance estimation model which took considering the statistical distribution change lead by the mean-preserving-filter non-positivity correction method. I applied it on the real-scale simulation data and showed that the new model could lower the bias in the low-dose CT image. (*see details in Chapter 4.2*)

Phantom and patient studies of the ULDCT attenuation correction for PET – Previous publications from our lab and collaborators had shown the feasibility of using ULDCT and sparse-view CT imaging for the attenuation correction for PET[88,124]. I further extended the idea to the real phantom and the patient data. By applying the model-based iterative reconstruction algorithms on the low-dose CT image, the result showed that the PET uptake bias in the patient lesion improved from -12% to 5% when comparing to the product FBP image. In addition, phantom data also shows the similar improvement. We expect to see that the PET accuracy from ULDCT attenuation correction could be further elevated when the CT tube-pulsing technique is available on the commercialized PET/CT scanner. (*see details in Chapter 5*)

Skew likelihood distribution and limits of estimation for the ULDCT imaging[150] **–** Previous works of mine were focused either on how to lower the phase-mismatch bias between CT and PET under the respiratory motion or on how to achieve the ULDCT attenuation correction for PET. In this part, on the other hand, we are asking the question about the limit on applying model-based iterative reconstruction method on the ULDCT image. And also, we would like to answer what factor did cause the limit and then where is the lowest dose boundary. With simulation and empirical data, I am able to show that the statistical distribution of post-log attenuation data was gradually skew and finally reach a likelihood plateau when source flux kept decreasing. The skew and plateau likelihood distributions contradict the assumption of normal distribution which is commonly used in the model based iterative reconstruction algorithm. We further applied the normality test and the maximum likelihood test on the attenuation values as a function of source flux so that we can categorized the data distribution into three regimes: normal statistic regime, skew statistic regime, and the electronic noise regime. The information could be used as a lookup

table for determining the 'reasonable lowest' source flux level for the patient in the future clinical use. (*see details in Chapter 6*)

Accuracy comparison between the respiratory-gated CT and the respiratory-gated cone-beam CT[151] **–** In Chapter 2 we showed how the phase-mismatch artifacts from the respiratory motion between CT and PET did cause the bias in the final PET uptake value. On the other hand, similar mismatch effect exists between respiratory-gated fan-beam and cone-beam CT imaging. The fan-beam CT modality was a known tool for measuring the lesion size and location in the treatment planning process; however, the cone-beam CT modality is more commonly used on the radiotherapy modality for guiding the high-energy source for the treatment. I used the respiratory motion phantom for comparing the measured volume of the same target lesion between the fan-beam and the cone-beam CT scanner, and we found that the average volume difference between two modalities could be up to 20%. This is first result quantitatively reveals a volume mismatch between two CT modalities, and we believe it could a useful information on defining more precise treatment margins for patients of radiotherapy. (*see details in Appendix A*)

BIBLIOGRAPHY

1. Even-Sapir E, Keidar Z, Bar-Shalom R. Hybrid Imaging (SPECT/CT and PET/CT)—Improving the Diagnostic Accuracy of Functional/Metabolic and Anatomic Imaging. *Semin Nucl Med*. 2009;39(4):264-275. doi:10.1053/j.semnuclmed.2009.03.004.

2. Hasegawa BH, Iwata K, Wong KH, et al. Dual-Modality Imaging of Function and Physiology. *Academic Radiology*. 2002;9(11):1305-1321. doi:10.1016/S1076-6332(03)80564-0.

3. Kinahan PE, Fletcher JW. Positron Emission Tomography-Computed Tomography Standardized Uptake Values in Clinical Practice and Assessing Response to Therapy. *Seminars in Ultrasound, CT and MRI*. 2010;31(6):496-505. doi:10.1053/j.sult.2010.10.001.

4. Chen DL, Kinahan PE. Multimodality molecular imaging of the lung. *Clin Transl Imaging*. 2014;2(5):391-401. doi:10.1007/s40336-014-0084-9.

5. Hasegawa BH, Wong KH, Iwata K, et al. Dual-Modality Imaging of Cancer with SPECT/CT. *Technol Cancer Res Treat*. 2002;1(6):449-458. doi:10.1177/153303460200100605.

6. Kinahan PE, Hasegawa BH, Beyer T. X-ray-based attenuation correction for positron emission tomography/computed tomography scanners. *Semin Nucl Med*. 2003;33(3):166-179. doi:10.1053/snuc.2003.127307.

7. Hofmann M, Steinke F, Scheel V, et al. MRI-based attenuation correction for PET/MRI: a novel approach combining pattern recognition and atlas registration. *J Nucl Med*. 2008;49(11):1875-1883. doi:10.2967/jnumed.107.049353.

8. Kinahan PE, Townsend DW, Beyer T, Sashin D. Attenuation correction for a combined 3D PET/CT scanner. *Med Phys*. 1998;25(10):2046-2053.

9. Seo Y, Wong KH, Sun M, Franc BL, Hawkins RA, Hasegawa BH. Correction of photon attenuation and collimator response for a body-contouring SPECT/CT imaging system. *J Nucl Med*. 2005;46(5):868-877.

10. Cherry SR. Multimodality Imaging: Beyond PET/CT and SPECT/CT. *Semin Nucl Med*. 2009;39(5):348-353. doi:10.1053/j.semnuclmed.2009.03.001.

11. Chen DL, Kinahan PE. Multimodality molecular imaging of the lung. *J Magn Reson Imaging*. 2010;32(6):1409-1420. doi:10.1002/jmri.22385.

12. Cherry SR, Sorenson JA, Phelps ME. *Physics in Nuclear Medicine*. Elsevier Health Sciences; 2012.

13. Hubbell JH. Photon Cross Sections, Attenuation Coefficients, and Energy Absorption

Coefficients from 10 keV to 100 GeV. August 1969.

14. Chang L-T. Attenuation Correction and Incomplete Projection in Single Photon Emission Computed Tomography. *Nuclear Science, IEEE Transactions on*. 1979;26(2):2780-2789. doi:10.1109/TNS.1979.4330536.

15. Wahl RL. To AC or not to AC: that is the question. *Journal of Nuclear Medicine*. 1999.

16. Bai C, Kinahan PE, Brasse D, et al. An Analytic Study of the Effects of Attenuation on Tumor Detection in Whole-Body PET Oncology Imaging. *J Nucl Med*. 2003;44(11):1855-1861.

17. Hendel RC, Corbett JR, Cullom SJ, DePuey EG, Garcia EV, Bateman TM. The value and practice of attenuation correction for myocardial perfusion SPECT imaging: a joint position statement from the American Society of Nuclear Cardiology and the Society of Nuclear Medicine. *J Nucl Cardiol*. 2002;9(1):135-143.

18. Xu EZ, Mullani NA, Gould KL, Anderson WL. A segmented attenuation correction for PET. *J Nucl Med*. 1991;32(1):161-165.

19. Frey EC, Tsui BMW, Perry JR. Simultaneous Acquisition of Emission and Transmission Data for Improved Thallium-201 Cardiac SPECT Imaging Using a Technetium-99m Transmission Source. *Journal of Nuclear Medicine*. 1992;33(12):2238-2245.

20. Ficaro EP, Fessler JA, Ackermann RJ, Rogers WL, Corbett JR, Schwaiger M. Simultaneous transmission-emission thallium-201 cardiac SPECT: effect of attenuation correction on myocardial tracer distribution. *J Nucl Med*. 1995;36(6):921-931.

21. Hsieh J. *Computed Tomography, Second Edition*. 1000 20th Street, Bellingham, WA 98227-0010 USA: SPIE; 2009. doi:10.1117/3.817303.

22. Quick HH. Integrated PET/MR. *J Magn Reson Imaging*. 2013;39(2):243-258. doi:10.1002/jmri.24523.

23. Bezrukov I, Mantlik F, Schmidt H, Schölkopf B, Pichler BJ. MR-Based PET attenuation correction for PET/MR imaging. *Semin Nucl Med*. 2013;43(1):45-59. doi:10.1053/j.semnuclmed.2012.08.002.

24. Delso G, Fürst S, Jakoby B, et al. Performance measurements of the Siemens mMR integrated whole-body PET/MR scanner. *J Nucl Med*. 2011;52(12):1914-1922. doi:10.2967/jnumed.111.092726.

25. Bailey DL, Antoch G, Bartenstein P, et al. Combined PET/MR: The Real Work Has Just Started. Summary Report of the Third International Workshop on PET/MR Imaging; February 17-21, 2014, Tübingen, Germany. *Mol Imaging Biol*. 2015;17(3):297-312. doi:10.1007/s11307-014-0818-0.

26. Hofmann M, Pichler B, Schoelkopf B, Beyer T. Towards quantitative PET/MRI: a

review of MR-based attenuation correction techniques. *Eur J Nucl Med Mol Imaging*. 2009;36(1):93-104. doi:10.1007/s00259-008-1007-7.

27. Buerger C, Tsoumpas C, Aitken A, et al. Investigation of MR-Based Attenuation Correction and Motion Compensation for Hybrid PET/MR. *Nuclear Science, IEEE Transactions on*. 2012;59(5):1967-1976. doi:10.1109/TNS.2012.2209127.

28. Kops ER, Wagenknecht G, Scheins J, Tellmann L, Herzog H. Attenuation correction in MR-PET scanners with segmented T1-weighted MR images. In: IEEE; 2009:2530-2533. doi:10.1109/NSSMIC.2009.5402034.

29. Zaidi H, Montandon M-L, Slosman DO. Magnetic resonance imaging-guided attenuation and scatter corrections in three-dimensional brain positron emission tomography. *Med Phys*. 2003;30(5):937-948. doi:10.1118/1.1569270.

30. Robson MD, Gatehouse PD, Bydder M, Bydder GM. Magnetic resonance: An introduction to ultrashort TE (UTE) imaging. *J Comput Assist Tomogr*. 2003;27(6):825-846.

31. McRobbie DW, Moore EA, Graves MJ, Prince MR. *MRI: From Picture to Proton, 2003*. Cambridge University Press doi:10.1046/j.1440-1673.2002.01119.x/abstract.

32. Marshall HR, Prato FS, Deans L, Théberge J, Thompson RT, Stodilka RZ. Variable lung density consideration in attenuation correction of whole-body PET/MRI. *J Nucl Med*. 2012;53(6):977-984. doi:10.2967/jnumed.111.098350.

33. Hofmann M, Bezrukov I, Mantlik F, et al. MRI-based attenuation correction for whole-body PET/MRI: quantitative evaluation of segmentation- and atlas-based methods. *J Nucl Med*. 2011;52(9):1392-1399. doi:10.2967/jnumed.110.078949.

34. Schreibmann E, Nye JA, Schuster DM, Martin DR, Votaw J, Fox T. MR-based attenuation correction for hybrid PET-MR brain imaging systems using deformable image registration. *Med Phys*. 2010;37(5):2101-2109.

35. Nuyts J, Dupont P, Stroobants S, Benninck R, Mortelmans L, Suetens P. Simultaneous maximum a posteriori reconstruction of attenuation and activity distributions from emission sinograms. *IEEE Trans Med Imaging*. 1999;18(5):393-403. doi:10.1109/42.774167.

36. Defrise M, Rezaei A, Nuyts J. Time-of-flight PET data determine the attenuation sinogram up to a constant. *Phys Med Biol*. 2012;57(4):885-899. doi:10.1088/0031-9155/57/4/885.

37. Conti M. Why is TOF PET reconstruction a more robust method in the presence of inconsistent data? *Phys Med Biol*. 2011;56(1):155-168. doi:10.1088/0031-9155/56/1/010.

38. Rezaei A, Defrise M, Bal G, et al. Simultaneous Reconstruction of Activity and

Attenuation in Time-of-Flight PET. *IEEE Trans Med Imaging*. 2012;31(12):2224-2233. doi:10.1109/TMI.2012.2212719.

39.   Cheng J-C, Salomon A, Yaqub M, Boellaard R. A more optimal initial attenuation image estimate in TOF-MLAA reconstruction for PET/MR. *J Nucl Med*. 2015;56(supplement 3):260-260.

40.   Salomon A, Goedicke A, Schweizer B, Aach T, Schulz V. Simultaneous Reconstruction of Activity and Attenuation for PET/MR. *IEEE Trans Med Imaging*. 2011;30(3):804-813. doi:10.1109/TMI.2010.2095464.

41.   Boellaard R, Hofman MBM, Hoekstra OS, Lammertsma AA. Accurate PET/MR Quantification Using Time of Flight MLAA Image Reconstruction. *Mol Imaging Biol*. 2014;16(4):469-477. doi:10.1007/s11307-013-0716-x.

42.   Mehranian A, Zaidi H. MR constrained simultaneous reconstruction of activity and attenuation maps in brain TOF-PET/MR imaging. *EJNMMI Phys*. 2014;1(1):1-1. doi:10.1186/2197-7364-1-S1-A55.

43.   LaCroix KJ, Tsui BMW, Hasegawa BH, Brown JK. Investigation of the use of X-ray CT images for attenuation compensation in SPECT. *Nuclear Science, IEEE Transactions on*. 1994;41(6):2793-2799. doi:10.1109/23.340649.

44.   FLEMING JS. A technique for using CT images in attenuation correction and quantification in SPECT. *Nuclear Medicine Communications*. 1989;10(2):83.

45.   Carney JPJ, Townsend DW, Rappoport V, Bendriem B. Method for transforming CT images for attenuation correction in PET/CT imaging. *Med Phys*. 2006;33(4):976-983.

46.   Patton JA, Turkington TG. SPECT/CT Physical Principles and Attenuation Correction. *J Nucl Med Technol*. 2008;36(1):1-10. doi:10.2967/jnmt.107.046839.

47.   Lonn AHR. Evaluation of method to minimize the effect of X-ray contrast in PET-CT attenuation correction. *... science symposium conference record*. 2003;3:2220-2221Vol.2223. doi:10.1109/NSSMIC.2003.1352321.

48.   Abella M, Alessio AM, Mankoff DA, et al. Accuracy of CT-based attenuation correction in PET/CT bone imaging. *Phys Med Biol*. 2012;57(9):2477-2490. doi:10.1088/0031-9155/57/9/2477.

49.   Johnson TRC. Dual-Energy CT: General Principles. *American Journal of Roentgenology*. 2012;199(5):S3-S8. doi:10.2214/AJR.12.9116.

50.   Kinahan PE, Alessio AM, Fessler JA. Dual energy CT attenuation correction methods for quantitative assessment of response to cancer therapy with PET/CT imaging. *Technol Cancer Res Treat*. 2006;5(4):319-327.

51.   Guy MJ, Castellano-Smith IA, Flower MA, Flux GD, Ott RJ, Visvikis D. DETECT -

Dual energy transmission estimation CT - for improved attenuation correction in SPECT and PET. *Nuclear Science, IEEE Transactions on*. 1998;45(3):1261-1267.

52.	Chuang K-S, Huang HK. Comparison of four dual energy image decomposition methods. *Phys Med Biol*. 1988;33(4):455. doi:10.1088/0031-9155/33/4/005.

53.	Alessio AM, Kinahan PE, Cheng PM, Vesselle H, Karp JS. PET/CT scanner instrumentation, challenges, and solutions. *Radiologic Clinics of North America*. 2004;42(6):1017-1032. doi:10.1016/j.rcl.2004.08.001.

54.	Rahmim A, Rousset O, Zaidi H. Strategies for Motion Tracking and Correction in PET. *PET Clinics*. 2007;2(2):251-266. doi:10.1016/j.cpet.2007.08.002.

55.	Matsumoto N, Berman DS, Kavanagh PB, et al. Quantitative assessment of motion artifacts and validation of a new motion-correction program for myocardial perfusion SPECT. *J Nucl Med*. 2001;42(5):687-694.

56.	Kiat H, Van Train KF, Friedman JD, et al. Quantitative Stress-Redistribution Thallium-201 SPECT Using Prone Imaging: Methodologic Development and Validation. *Journal of Nuclear Medicine*. 1992;33(8):1509-1515.

57.	Osman M, Cohade C, Nakamoto Y, Wahl R. Respiratory motion artifacts on PET emission images obtained using CT attenuation correction on PET-CT. *Eur J Nucl Med Mol Imaging*. 2003;30(4):603-606.

58.	Goerres GW, Burger C, Kamel E, et al. Respiration-induced attenuation artifact at PET/CT: technical considerations. 2003;226(3):906-910. doi:10.1148/radiol.2263011732.

59.	McQuaid SJ, Hutton BF. Sources of attenuation-correction artefacts in cardiac PET/CT and SPECT/CT. *Eur J Nucl Med Mol Imaging*. 2008;35(6):1117-1123. doi:10.1007/s00259-008-0718-0.

60.	Goetze S, Brown TL, Lavely WC, Zhang Z, Bengel FM. Attenuation correction in myocardial perfusion SPECT/CT: effects of misregistration and value of reregistration. *J Nucl Med*. 2007;48(7):1090-1095. doi:10.2967/jnumed.107.040535.

61.	Wink NM, Panknin C, Solberg TD. Phase versus amplitude sorting of 4D-CT data. *JACMP*. 2006;7(1). doi:10.1120/jacmp.v7i1.2198.

62.	Lu W, Parikh PJ, Hubenschmidt JP, Bradley JD, Low DA. A comparison between amplitude sorting and phase-angle sorting using external respiratory measurement for 4D CT. *Med Phys*. 2006;33(8):2964-2974.

63.	Abdelnour AF, Nehmeh SA, Pan T, et al. Phase and amplitude binning for 4D-CT imaging. *Phys Med Biol*. 2007;52(12):3515-3529. doi:10.1088/0031-9155/52/12/012.

64.	Li R, Lewis JH, Cerviño LI, Jiang SB. 4D CT sorting based on patient internal anatomy.

Phys Med Biol. 2009;54(15):4821-4833. doi:10.1088/0031-9155/54/15/012.

65. Liu C, Alessio AM, Kinahan PE. Respiratory motion correction for quantitative PET/CT using all detected events with internal-external motion correlation. *Med Phys*. 2011;38(5):2715-2723.

66. Mancosu P, Sghedoni R, Bettinardi V, et al. 4D-PET data sorting into different number of phases: a NEMA IQ phantom study. *JACMP*. 2009;10(4). doi:10.1120/jacmp.v10i4.2917.

67. Bettinardi V, Rapisarda E, Gilardi MC. Number of partitions (gates) needed to obtain motion-free images in a respiratory gated 4D-PET/CT study as a function of the lesion size and motion displacement. *Med Phys*. 2009;36(12):5547. doi:10.1118/1.3254431.

68. Nyflot MJ, Lee T-C, Alessio AM, et al. Impact of CT attenuation correction method on quantitative respiratory-correlated (4D) PET/CT imaging. *Med Phys*. 2015;42(1):110. doi:10.1118/1.4903282.

69. Chi P-CM, Mawlawi O, Nehmeh SA, et al. Design of respiration averaged CT for attenuation correction of the PET data from PET/CT. *Med Phys*. 2007;34(6):2039-2047.

70. Pan T, Sun X, Luo D. Improvement of the cine-CT based 4D-CT imaging. *Med Phys*. 2007;34(11):4499-4503.

71. Brendle CB, Schmidt H, Fleischer S, Braeuning UH, Pfannenberg CA, Schwenzer NF. Simultaneously acquired MR/PET images compared with sequential MR/PET and PET/CT: alignment quality. 2013;268(1):190-199. doi:10.1148/radiol.13121838.

72. Dizendorf E, Hany TF, Buck A, Schulthess Von GK, Burger C. Cause and magnitude of the error induced by oral CT contrast agent in CT-based attenuation correction of PET emission studies. *J Nucl Med*. 2003;44(5):732-738.

73. Difilippo FP, Brunken RC. Do implanted pacemaker leads and ICD leads cause metal-related artifact in cardiac PET/CT? *J Nucl Med*. 2005;46(3):436-443.

74. Abdoli M, Ay MR, Ahmadian A, Dierckx RAJO, Zaidi H. Reduction of dental filling metallic artifacts in CT-based attenuation correction of PET data using weighted virtual sinograms optimized by a genetic algorithm. *Med Phys*. 2010;37(12):6166-6177. doi:10.1118/1.3511507.

75. Buether F, Stegger L, Dawood M, et al. Effective methods to correct contrast agent-induced errors in PET quantification in cardiac PET/CT. *J Nucl Med*. 2007;48(7):1060-1068. doi:10.2967/jnumed.107.039941.

76. Xia T, Alessio AM, Kinahan PE. Dual energy CT for attenuation correction with PET/CT. *Med Phys*. 2014;41(1). doi:10.1118/1.4828838.

77. Mawlawi O, Erasmus JJ, Pan T, et al. Truncation Artifact on PET/CT: Impact on

Measurements of Activity Concentration and Assessment of a Correction Algorithm. *American Journal of Roentgenology*. 2006;186(5):1458-1467. doi:10.2214/AJR.05.0255.

78. Beyer T, Bockisch A, Kühl H, Martinez M-J. Whole-body 18F-FDG PET/CT in the presence of truncation artifacts. *J Nucl Med*. 2006;47(1):91-99.

79. Hsieh J, Chao E, Thibault J, et al. A novel reconstruction algorithm to extend the CT scan field-of-view. *Med Phys*. 2004;31(9):2385-2391. doi:10.1118/1.1776673.

80. Hurwitz LM, Reiman RE, Yoshizumi TT, et al. Radiation dose from contemporary cardiothoracic multidetector CT protocols with an anthropomorphic female phantom: implications for cancer induction. 2007;245(3):742-750. doi:10.1148/radiol.2453062046.

81. Sodickson A, Baeyens PF, Andriole KP, et al. Recurrent CT, Cumulative Radiation Exposure, and Associated Radiation-induced Cancer Risks from CT of Adults 1. 2009;251(1):175-184. doi:10.1148/radiol.2511081296.

82. Goske MJ, Applegate KE, Boylan J, et al. The "Image Gently" campaign: increasing CT radiation dose awareness through a national education and awareness program. *Pediatr Radiol*. 2008;38(3):265-269. doi:10.1007/s00247-007-0743-3.

83. Kamel E, Hany TF, Burger C, et al. CT vs Ge-68 attenuation correction in a combined PET/CT system: evaluation of the effect of lowering the CT tube current. *Eur J Nucl Med Mol Imaging*. 2002;29(3):346-350. doi:10.1007/s00259-001-0698-9.

84. Boellaard R, O'Doherty MJ, Weber WA, et al. FDG PET and PET/CT: EANM procedure guidelines for tumour PET imaging: version 1.0. *Eur J Nucl Med Mol Imaging*. 2010;37(1):181-200. doi:10.1007/s00259-009-1297-4.

85. Mattsson S, Johansson L, Liniecki J, et al. Radiation Dose to Patients from Radiopharmaceuticals. In: *World Congress on Medical Physics and Biomedical Engineering, September 7 - 12, 2009, Munich, Germany*. Vol 25/3. IFMBE Proceedings. Berlin, Heidelberg: Springer Berlin Heidelberg; 2009:474-477. doi:10.1007/978-3-642-03902-7_134.

86. Alessio AM, Kinahan PE, Manchanda V, Ghioni V, Aldape L, Parisi MT. Weight-based, low-dose pediatric whole-body PET/CT protocols. *J Nucl Med*. 2009;50(10):1570-1577. doi:10.2967/jnumed.109.065912.

87. Brix G, Lechel U, Glatting G, et al. Radiation exposure of patients undergoing whole-body dual-modality 18F-FDG PET/CT examinations. *J Nucl Med*. 2005;46(4):608-613.

88. Xia T, Alessio AM, De Man B, Manjeshwar R, Asma E, Kinahan PE. Ultra-low dose CT attenuation correction for PET/CT. *Phys Med Biol*. 2012;57(2):309-328. doi:10.1088/0031-9155/57/2/309.

89.   Colsher JG, Jiang Hsieh, Thibault JB, et al. Ultra low dose CT for attenuation correction in PET/CT. ... *Record*. 2008:5506-5511. doi:10.1109/NSSMIC.2008.4774499.

90.   Hsieh J. Adaptive streak artifact reduction in computed tomography resulting from excessive x-ray photon noise. *Med Phys*. 1998;25(11):2139-2147.

91.   Xia T, Alessio A, Kinahan PE. *Xia: Spectral Shaping for Ultra-Low Dose CT Attenuation... - Google Scholar*. The First International Meeting on Image Formation in …; 2010.

92.   Graff CG, Sidky EY. Compressive sensing in medical imaging. *Appl Opt, AO*. 2015;54(8):C23-C44. doi:10.1364/AO.54.000C23.

93.   Thibault J-B, Sauer KD, Bouman CA, Hsieh J. A three-dimensional statistical approach to improved image quality for multislice helical CT. *Med Phys*. 2007;34(11):4526-4544. doi:10.1118/1.2789499.

94.   Whiting BR, Massoumzadeh P, Earl OA, O'Sullivan JA, Snyder DL, Williamson JF. Properties of preprocessed sinogram data in x-ray computed tomography. *Med Phys*. 2006;33(9):3290-3303. doi:10.1118/1.2230762.

95.   La Riviere PJ, Bian J, Vargas PA. Penalized-likelihood sinogram restoration for computed tomography. *IEEE Trans Med Imaging*. 2006;25(8):1022-1036. doi:10.1109/TMI.2006.875429.

96.   Nestle U, Walter K, Schmidt S, et al. 18F-deoxyglucose positron emission tomography (FDG-PET) for the planning of radiotherapy in lung cancer: high impact in patients with atelectasis. *International Journal of Radiation Oncology*Biology*Physics*. 1999;44(3):593-597.

97.   Vansteenkiste JF, Stroobants SG, De Leyn PR, et al. Lymph node staging in non-small-cell lung cancer with FDG-PET scan: a prospective study on 690 lymph node stations from 68 patients. *Journal of Clinical Oncology*. 1998;16(6):2142-2149. doi:10.1200/JCO.1998.16.6.2142.

98.   Vanuytsel LJ, Vansteenkiste JF, Stroobants SG, et al. The impact of (18)F-fluoro-2-deoxy-D-glucose positron emission tomography (FDG-PET) lymph node staging on the radiation treatment volumes in patients with non-small cell lung cancer. *Radiother Oncol*. 2000;55(3):317-324.

99.   Bradley J, Thorstad WL, Mutic S, et al. Impact of FDG-PET on radiation therapy volume delineation in non-small-cell lung cancer. *International Journal of Radiation Oncology*Biology*Physics*. 2004;59(1):78-86. doi:10.1016/j.ijrobp.2003.10.044.

100.   Fox JL, Rengan R, O'Meara W, et al. Does registration of PET and planning CT images decrease interobserver and intraobserver variation in delineating tumor volumes for non-small-cell lung cancer? *International Journal of Radiation Oncology*Biology*Physics*. 2005;62(1):70-75. doi:10.1016/j.ijrobp.2004.09.020.

101.   Bradley J, Bae K, Choi N, et al. A phase II comparative study of gross tumor volume definition with or without PET/CT fusion in dosimetric planning for non-small-cell lung cancer (NSCLC): primary analysis of Radiation Therapy Oncology Group (RTOG) 0515. *Int J Radiat Oncol Biol Phys*. 2012;82(1):435–41.e1. doi:10.1016/j.ijrobp.2010.09.033.

102.   van Elmpt W, De Ruysscher D, van der Salm A, et al. The PET-boost randomised phase II dose-escalation trial in non-small cell lung cancer. *Radiother Oncol*. 2012;104(1):67-71. doi:10.1016/j.radonc.2012.03.005.

103.   Aerts HJWL, van Baardwijk AAW, Petit SF, et al. Identification of residual metabolic-active areas within individual NSCLC tumours using a pre-radiotherapy (18)Fluorodeoxyglucose-PET-CT scan. *Radiother Oncol*. 2009;91(3):386-392. doi:10.1016/j.radonc.2009.03.006.

104.   Erdi YE, Nehmeh SA, Pan T, et al. The CT Motion Quantitation of Lung Lesions and Its Impact on PET-Measured SUVs. *Journal of Nuclear Medicine*. 2004;45(8):1287-1292.

105.   Goerres GW, Kamel E, Seifert B, et al. Accuracy of image coregistration of pulmonary lesions in patients with non-small cell lung cancer using an integrated PET/CT system. *J Nucl Med*. 2002;43(11):1469-1475.

106.   Pan T, Mawlawi O, Nehmeh SA, et al. Attenuation correction of PET images with respiration-averaged CT images in PET/CT. *J Nucl Med*. 2005;46(9):1481-1487.

107.   Nehmeh SA, Erdi YE, Ling CC, et al. Effect of respiratory gating on quantifying PET images of lung cancer. *J Nucl Med*. 2002;43(7):876-881.

108.   Ford EC, Mageras GS, Yorke E, Ling CC. Respiration-correlated spiral CT: a method of measuring respiratory-induced anatomic motion for radiation treatment planning. *Med Phys*. 2003;30(1):88-97. doi:10.1118/1.1531177.

109.   Vedam SS, Keall PJ, Kini VR, Mostafavi H, Shukla HP, Mohan R. Acquiring a four-dimensional computed tomography dataset using an external respiratory signal. *Phys Med Biol*. 2003;48(1):45-62.

110.   Low DA, Nystrom M, Kalinin E, et al. A method for the reconstruction of four-dimensional synchronized CT scans acquired during free breathing. *Med Phys*. 2003;30(6):1254-1263. doi:10.1118/1.1576230.

111.   Pan T, Lee T-Y, Rietzel E, Chen GTY. 4D-CT imaging of a volume influenced by respiratory motion on multi-slice CT. *Med Phys*. 2004;31(2):333-340.

112.   Nagel CCA, Bosmans G, Dekker ALAJ, et al. Phased attenuation correction in respiration correlated computed tomography/positron emitted tomography. *Med Phys*. 2006;33(6):1840-1847.

113.   Pönisch F, Richter C, Just U, Enghardt W. Attenuation correction of four dimensional

(4D) PET using phase-correlated 4D-computed tomography. *Phys Med Biol*. 2008;53(13):N259-N268. doi:10.1088/0031-9155/53/13/N03.

114. Park S-J, Ionascu D, Killoran J, et al. Evaluation of the combined effects of target size, respiratory motion and background activity on 3D and 4D PET/CT images. *Phys Med Biol*. 2008;53(13):3661-3679. doi:10.1088/0031-9155/53/13/018.

115. Killoran JH, Gerbaudo VH, Mamede M, Ionascu D, Park S-J, Berbeco R. Motion artifacts occurring at the lung/diaphragm interface using 4D CT attenuation correction of 4D PET scans. *JACMP*. 2011;12(4). doi:10.1120/jacmp.v12i4.3502.

116. Alessio AM, Kohlmyer S, Branch K, Chen G, Caldwell J, Kinahan P. Cine CT for attenuation correction in cardiac PET/CT. *J Nucl Med*. 2007;48(5):794-801. doi:10.2967/jnumed.106.035717.

117. Wahl RL, Jacene H, Kasamon Y, Lodge MA. From RECIST to PERCIST: Evolving Considerations for PET Response Criteria in Solid Tumors. *Journal of Nuclear Medicine*. 2009;50(Suppl 1):122S–150S.

118. Fayad H, Pan T, Pradier O, Visvikis D. Patient specific respiratory motion modeling using a 3D patient's external surface. *Med Phys*. 2012;39(6):3386-3395. doi:10.1118/1.4718578.

119. Nestle U, Kremp S, Schaefer-Schuler A, et al. Comparison of different methods for delineation of F-18-FDG PET-positive tissue for target volume definition in radiotherapy of patients with non-small cell lung cancer. *J Nucl Med*. 2005;46(8):1342-1348.

120. Geets X, Lee JA, Bol A, Lonneux M, Gregoire V. A gradient-based method for segmenting FDG-PET images: methodology and validation. *Eur J Nucl Med Mol Imaging*. 2007;34(9):1427-1438. doi:10.1007/s00259-006-0363-4.

121. Hatt M, le Rest CC, Turzo A, Roux C, Visvikis D. A Fuzzy Locally Adaptive Bayesian Segmentation Approach for Volume Determination in PET. *IEEE Trans Med Imaging*. 2009;28(6):881-893. doi:10.1109/TMI.2008.2012036.

122. Li H, Thorstad WL, Biehl KJ, et al. A novel PET tumor delineation method based on adaptive region-growing and dual-front active contours. *Med Phys*. 2008;35(8):3711-3721. doi:10.1118/1.2956713.

123. Kinahan P, Wollenweber S, Alessio A, et al. Impact of respiration variability on respiratory gated whole-body PET/CT imaging. *J Nucl Med*. 2007;48(supplement 2):196P–196P.

124. Rui X, Cheng L, Long Y, et al. Ultra-low dose CT attenuation correction for PET/CT: analysis of sparse view data acquisition and reconstruction algorithms. *Phys Med Biol*. September 2015:7437-7460. doi:10.1088/0031-9155/60/19/7437.

125.   Segars WP, Tsui BMW. MCAT to XCAT: The Evolution of 4-D Computerized Phantoms for Imaging Research. *Proc IEEE*. 2009;97(12):1954-1968. doi:10.1109/JPROC.2009.2022417.

126.   Liu C, Pierce LA II, Alessio AM, Kinahan PE. The impact of respiratory motion on tumor quantification and delineation in static PET/CT imaging. *Phys Med Biol*. 2009;54(24):7345. doi:10.1088/0031-9155/54/24/007.

127.   Sidky EY, Pan X. Image reconstruction in circular cone-beam computed tomography by constrained, total-variation minimization. *Phys Med Biol*. 2008;53(17):4777-4807. doi:10.1088/0031-9155/53/17/021.

128.   Yu H, Wang G. Compressed sensing based interior tomography. *Phys Med Biol*. 2009;54(9):2791-2805. doi:10.1088/0031-9155/54/9/014.

129.   De Man B, Basu S, Chandra N, et al. CatSim: a new computer assisted tomography simulation environment. Hsieh J, Flynn MJ, eds. *Medical Imaging*. 2007;6510:65102G–65102G–8. doi:10.1117/12.710713.

130.   Chen G-H, Tang J, Leng S. Prior image constrained compressed sensing (PICCS): a method to accurately reconstruct dynamic CT images from highly undersampled projection data sets. *Med Phys*. 2008;35(2):660-663. doi:10.1118/1.2836423.

131.   Xu Q, Yu H, Mou X, Zhang L, Hsieh J, Wang G. Low-dose X-ray CT reconstruction via dictionary learning. *IEEE Trans Med Imaging*. 2012;31(9):1682-1697. doi:10.1109/TMI.2012.2195669.

132.   Zhang H, Huang J, Ma J, et al. Iterative reconstruction for x-ray computed tomography using prior-image induced nonlocal regularization. *IEEE Trans Biomed Eng*. 2014;61(9):2367-2378. doi:10.1109/TBME.2013.2287244.

133.   Thibault J-B, Bouman CA, Sauer KD, Hsieh J. A recursive filter for noise reduction in statistical iterative tomographic imaging. *Electronic ....* February 2006:60650X–60650X–10. doi:10.1117/12.660281.

134.   Sauer K, Bouman C. A local update strategy for iterative reconstruction from projections. *Signal Processing, IEEE Transactions on*. 1993;41(2):534-548. doi:10.1109/78.193196.

135.   Chang Z, Zhang R, Thibault J-B, et al. Modeling and Pre-Treatment of Photon-Starved CT Data for Iterative Reconstruction. *IEEE Trans Med Imaging*. September 2016:1-1. doi:10.1109/TMI.2016.2606338.

136.   Lin Fu, Tzu-Cheng Lee, Soo Mee Kim, et al. Comparison Between Pre-Log and Post-Log Statistical Models in Ultra-Low-Dose CT Reconstruction. *IEEE Trans Med Imaging*. 2017;36(3):707-720. doi:10.1109/TMI.2016.2627004.

137.   Erdoğan H, Fessler JA. Monotonic algorithms for transmission tomography. *IEEE Trans*

Med Imaging. 1999;18(9):801-814. doi:10.1109/42.802758.

138. Nuyts J, De Man B, Fessler JA, Zbijewski W, Beekman FJ. Modelling the physics in the iterative reconstruction for transmission computed tomography. *Phys Med Biol*. 2013;58(12):R63-R96. doi:10.1088/0031-9155/58/12/R63.

139. Li TF, Li X, Wang J, et al. Nonlinear sinogram smoothing for low-dose X-ray CT. *Nuclear Science, IEEE Transactions on*. 2004;51(5):2505-2513. doi:10.1109/TNS.2004.834824.

140. Lu H, Hsiao I-T, Li X, Liang Z. Noise properties of low-dose CT projections and noise treatment by scale transformations. *Nuclear Science Symposium Conference Record, 2001 IEEE*. 2001;3:1662-1666vol.1663. doi:10.1109/NSSMIC.2001.1008660.

141. Lee TC, Alessio AM, Miyaoka RM, Kinahan PE. Morphology supporting function: attenuation correction for SPECT/CT, PET/CT, and PET/MR imaging. *Q J Nucl Med Mol Imaging*. 2016;60(1):25-39.

142. Bouman CA, Sauer K. A unified approach to statistical tomography using coordinate descent optimization. *IEEE Trans Image Process*. 1996;5(3):480-492. doi:10.1109/83.491321.

143. Kim SM, Alessio AM, De Man B, Asma E, Kinahan PE. Direct reconstruction of CT-based attenuation correction images for PET with cluster-based penalties. In: IEEE; 2013:1-4. doi:10.1109/NSSMIC.2013.6829245.

144. Otsu N. A Threshold Selection Method from Gray-Level Histograms. *IEEE Trans Syst, Man, Cybern*. 1979;9(1):62-66. doi:10.1109/TSMC.1979.4310076.

145. Perlmutter DS, Kim SM, Kinahan PE, Alessio AM. Statistical Comparison of Likelihood Models for Low Dose X-ray CT.

146. Soo Mee Kim, Alessio AM, Perlmutter DS, Thibault J-B, De Man B, Kinahan PE. Analysis of statistical models for iterative reconstruction of extremely low-dose CT data. In: IEEE; 2014:1-4. doi:10.1109/NSSMIC.2014.7430762.

147. Chakravarti IM, Laha RG. *Handbook of Methods of Applied Statistics,* 1967.

148. Zhang R, Chang A, Thibault J-B, Sauer K, Bouman C. Statistical modeling challenges in model-based reconstruction for x-ray CT. *IS&T/SPIE …*. February 2013:86570S–86570S–8. doi:10.1117/12.2013231.

149. Forghani R, De Man B, Gupta R. Dual-Energy Computed Tomography. *Neuroimaging Clinics of North America*. 2017;27(3):371-384. doi:10.1016/j.nic.2017.03.002.

150. Lee T-C, Zhang R, Alessio AM, Fu L, De Man B, Kinahan PE. Statistical distributions of ultra-low dose CT sinograms and their fundamental limits. In: International Society for Optics and Photonics; 2017:101320N–101320N–7. doi:10.1117/12.2254375.

151.   Lee T-C, Bowen SR, James SS, Sandison GA, Kinahan PE, Nyflot MJ. Accuracy Comparison of 4D Computed Tomography (4DCT) and 4D Cone Beam Computed Tomography (4DCBCT). *IJMPCERO*. 2017;06(03):323-335. doi:10.4236/ijmpcero.2017.63029.

152.   Mageras GS, Pevsner A, Yorke ED, et al. Measurement of lung tumor motion using respiration-correlated CT. *International Journal of Radiation Oncology*Biology*Physics*. 2004;60(3):933-941. doi:10.1016/j.ijrobp.2004.06.021.

153.   Shirato H, Seppenwoolde Y, Kitamura K, ONIMURA R, SHIMIZU S. Intrafractional tumor motion: lung and liver. *Seminars in Radiation Oncology*. 2004;14(1):10-18. doi:10.1053/j.semradonc.2003.10.008.

154.   Beyer T, Antoch G, Blodgett T, Freudenberg LF, Akhurst T, Mueller S. Dual-modality PET/CT imaging: the effect of respiratory motion on combined image quality in clinical oncology. *Eur J Nucl Med Mol Imaging*. 2003;30(4):588-596. doi:10.1007/s00259-002-1097-6.

155.   Keall P. 4-dimensional computed tomography imaging and treatment planning. *Seminars in Radiation Oncology*. 2004;14(1):81-90. doi:10.1053/j.semradonc.2003.10.006.

156.   Rietzel E, Chen G, Choi NC, Willet CG. Four-dimensional image-based treatment planning: Target volume segmentation and dose calculation in the presence of respiratory motion. *International Journal of Radiation Oncology*Biology*Physics*. 2005;61(5):1535-1550. doi:10.1016/j.ijrobp.2004.11.037.

157.   Therasse P, Arbuck SG, Eisenhauer EA, et al. New guidelines to evaluate the response to treatment in solid Tumors. *J Natl Cancer Inst*. 2000;92(3):205-216.

158.   Greco C, Rosenzweig K, Cascini GL, Tamburrini O. Current status of PET/CT for tumour volume definition in radiotherapy treatment planning for non-small cell lung cancer (NSCLC). *Lung Cancer*. 2007;57(2):125-134. doi:10.1016/j.lungcan.2007.03.020.

159.   Underberg R, Lagerwaard FJ, Cuijpers JP, Slotman BJ, de Koste J, Senan S. Four-dimensional ct scans for treatment planning in stereotactic radiotherapy for stage I lung cancer. *International Journal of Radiation Oncology*Biology*Physics*. 2004;60(4):1283-1290. doi:10.1016/j.ijrobp.2004.07.065.

160.   Rietzel E, Liu AK, Doppke KP, et al. Design of 4D treatment planning target volumes. *International Journal of Radiation Oncology*Biology*Physics*. 2006;66(1):287-295. doi:10.1016/j.ijrobp.2006.05.024.

161.   Kriminski S, Mitschke M, Sorensen S, et al. Respiratory correlated cone-beam computed tomography on an isocentric C-arm. *Phys Med Biol*. 2005;50(22):5263-5280. doi:10.1088/0031-9155/50/22/004.

162. Sonke J-J, Zijp L, Remeijer P, van Herk M. Respiratory correlated cone beam CT. *Med Phys*. 2005;32(4):1176-1186. doi:10.1118/1.1869074.

163. Dietrich L, Jetter S, Tücking T, Nill S, Oelfke U. Linac-integrated 4D cone beam CT: first experimental results. *Phys Med Biol*. 2006;51(11):2939-2952. doi:10.1088/0031-9155/51/11/017.

164. Sweeney RA, Seubert B, Stark S, et al. Accuracy and inter-observer variability of 3D versus 4D cone-beam CT based image-guidance in SBRT for lung tumors. *Radiat Oncol*. 2012;7:81. doi:10.1186/1748-717X-7-81.

165. Lee S, Yan G, Lu B, Kahler D, Li JG, Sanjiv SS. Impact of scanning parameters and breathing patterns on image quality and accuracy of tumor motion reconstruction in 4D CBCT: a phantom study. *J Appl Clin Med Phys*. 2015;16(6):195-212.

166. Iramina H, Nakamura M, Iizuka Y, et al. The accuracy of extracted target motion trajectories in four-dimensional cone-beam computed tomography for lung cancer patients. *Radiother Oncol*. 2016;121(1):46-51. doi:10.1016/j.radonc.2016.07.022.

167. Purdie TG, Moseley DJ, Bissonnette J-P, et al. Respiration correlated cone-beam computed tomography and 4DCT for evaluating target motion in Stereotactic Lung Radiation Therapy. *Acta Oncologica*. 2006;45(7):915-922. doi:10.1080/02841860600907345.

168. Gupta R, Cheung AC, Bartling SH, et al. Flat-Panel Volume CT: Fundamental Principles, Technology, and Applications. *RadioGraphics*. November 2008. doi:10.1148/rg.287085004.

169. Orth RC, Wallace MJ, Kuo MD, Int TACS. C-arm Cone-beam CT: General Principles and Technical Considerations for Use in Interventional Radiology (Reprinted from J Vasc Interv Radiol, vol 19, pg 814-820, 2008). *Journal of Vascular and Interventional Radiology*. 2009;20(7):S538-S544. doi:10.1016/j.jvir.2009.04.026.

170. Clements N, Kron T, Franich R, et al. The effect of irregular breathing patterns on internal target volumes in four-dimensional CT and cone-beam CT images in the context of stereotactic lung radiotherapy. *Med Phys*. 2013;40(2):021904. doi:10.1118/1.4773310.

171. Wang L, Chen X, Lin M-H, et al. Evaluation of the cone beam CT for internal target volume localization in lung stereotactic radiotherapy in comparison with 4D MIP images. *Med Phys*. 2013;40(11):111709. doi:10.1118/1.4823785.

172. Rit S, Pinho R, Delmon V, Pech M. VV, a 4D slicer. In:; 2011.

173. Loening AM, Gambhir SS. AMIDE: a free software tool for multimodality medical image analysis. *Mol Imaging*. 2003;2(3):131-137.

174. Zhang R, Alessio AM, Pierce LA, et al. Improved attenuation correction for respiratory

gated PET/CT with extended-duration cine CT: a simulation study. In: Flohr TG, Lo JY, Gilat Schmidt T, eds. Vol 10132. International Society for Optics and Photonics; 2017:101321I–101321I–7. doi:10.1117/12.2254599.

175.   Rui X, Jin Y, FitzGerald PF, Alessio A, Kinahan P, Man BD. Optimal kVp Selection for Contrast CT Imaging Based on a Projection-domain Method. *Conf Proc Int Conf Image Form Xray Comput Tomogr*. 2014;2014:173-177.

176.   Sun M, Star-Lack JM. Improved scatter correction using adaptive scatter kernel superposition. *Phys Med Biol*. 2010;55(22):6695-6720. doi:10.1088/0031-9155/55/22/007.

177.   Gao H, Fahrig R, Bennett NR, Sun M, Star-Lack J, Zhu L. Scatter correction method for x-ray CT using primary modulation: phantom studies. *Med Phys*. 2010;37(2):934-946. doi:10.1118/1.3298014.

178.   Zhang Y, Yang J, Zhang L, Court LE, Balter PA, Dong L. Modeling respiratory motion for reducing motion artifacts in 4D CT images. *Med Phys*. 2013;40(4):041716. doi:10.1118/1.4795133.

179.   Johnston E, Diehn M, Murphy JD, Loo BW, Maxim PG. Reducing 4D CT artifacts using optimized sorting based on anatomic similarity. *Med Phys*. 2011;38(5):2424-2429.

180.   Schleyer PJ, O'Doherty MJ, Barrington SF, Marsden PK. Retrospective data-driven respiratory gating for PET/CT. *Phys Med Biol*. 2009;54(7):1935. doi:10.1088/0031-9155/54/7/005.

181.   Bergner F, Berkus T, Oelhafen M, Kunz P, Pan T, Kachelriess M. Autoadaptive phase-correlated (AAPC) reconstruction for 4D CBCT. *Med Phys*. 2009;36(12):5695-5706. doi:10.1118/1.3260919.

182.   Shieh C-C, Kipritidis J, O'Brien RT, Kuncic Z, Keall PJ. Image quality in thoracic 4D cone-beam CT: A sensitivity analysis of respiratory signal, binning method, reconstruction algorithm, and projection angular spacing. *Med Phys*. 2014;41(4). doi:10.1118/1.4868510.

APPENDIX A: ACCURACY COMPARISON OF 4-D CT AND 4-D CONE BEAM CT

ABSTRACT

The ability of respiratory-correlated fan beam CT (4DCT) and respiratory-correlated cone beam CT (4DCBCT) to accurately estimate tumor volume is critical to accurate dosimetry and treatment verification for lung stereotactic body radiation therapy (SBRT) and other motion-managed therapies. However, it is known that 4DCT and 4DCBCT differ in aspects of image acquisition and reconstruction that may lead to discrepancies between the two modalities. To evaluate quantitative differences between 4DCT and 4DCBCT imaging under respiratory motion, we performed a phantom study in the ground truth setting. A programmable respiratory motion phantom was used to simulate the 1D S-I position of a known-size lesion. Ten sinusoidal and twenty patient-specific breathing waveforms were applied to drive lesion motion during the 4DCT and 4DCBCT acquisitions. The difference in lesion volume acquired between the two imaging modalities was as high as 34.4% and 18.4% for sinusoidal and patient-specific breathing motions, respectively. When compared to the true volume, 4DCT measurement often underestimated the lesion size whereas 4DCBCT overestimated the lesion volume in most of the cases. 4DCBCT gave more accurate recovery of the volume than 4DCT for most settings tested in this study. These findings may be helpful for improving the definition of internal target and planning target volume margins, and extracting quantitative information from on-board treatment verification imaging.

I. INTRODUCTION

Accurate computed tomography (CT) studies under the presence of respiratory motion are necessary for treatment planning, treatment verification, and adaptive radiotherapy in many

cancers, most commonly for cancers of the lung, liver, and abdomen[58,106,152-154]. 4DCT imaging may be used for respiratory motion assessment and creating an external beam radiation treatment plan for a free-breathing patient[155,156]. Radiotherapy image-guided verification is commonly performed by comparing lesion position and motion estimated in the treatment room with cone beam CT (CBCT), CT on rails, megavoltage CT (MVCT) or other methods to the primary planning CT study acquired at the time of treatment simulation. Beyond the critical role of verification imaging in patient setup, changes in CT volumes have been used as indications for adaptive re-planning and modeled to extract radiobiological parameters[157,158].

It is known that respiratory motion leads to significant imaging artifacts which may lead to incorrect treatment planning volumes, lesion localization, or inference of change in tumor volume over time. Respiratory-correlated computed tomography (4DCT) using external respiratory surrogates was first proposed as solution for this problem[108-111] and has rapidly become a standard of care for radiotherapy simulation in the presence of respiratory motion[159,160]. In the intervening years, cone beam computed tomography (CBCT) technology has proliferated on linear accelerators to provide image guidance for radiotherapy verification, and recently, respiratory-correlated cone beam CT (4DCBCT) has become clinically available[161-163]. Sonke *et al.* investigated 4DCBCT versus 3DCBCT and fluoroscopy and found motion artifacts in 4D dataset were substantially reduced compared to a 3D scan[162]. Sweeney *et al.* investigated inter-observer variability of target localization for 4DCBCT and 3DCBCT imaging with patient data and found significantly reduced variability with 4DCBCT[164]. Lee *et al.* and Iramina *et al.* further examined the impact of scanning parameters and motion sorting methods related to the accuracy of 4DCBCT images[165,166].

However, clinical investigation of comparisons of 4DCBCT and 4DCT imaging for tumor motion assessment have indicated significant differences in some patients[167]. 4DCT and 4DCBCT imaging differs in numerous aspects in terms of image acquisition, hardware geometry, and binning techniques[168,169]. These differences include smaller x-ray beam volumetric coverage in CT versus much larger coverage in CBCT for a single rotation, scan time on the order of seconds in 4DCT versus minutes in 4DCBCT, arc detector versus flat panel detector geometry employed with different anti-scatter setups, and external surrogates in 4DCT versus internal tracking in 4DCBCT of respiratory motion. To date, investigations of accuracy of respiratory-correlated fan beam versus cone beam CT imaging in the presence of respiratory motion in the ground truth setting have been limited. Researchers have compared 3DCBCT image to the 4DCT maximum intensity projection (MIP) reconstructed image of anthropomorphic respiratory phantoms and found contradictory results[170,171]. Nevertheless, the relative accuracy of 4DCBCT and 4DCT in the ground truth setting is unknown.

We had shown the uptake accuracy in 4D phased-match CT attenuation corrected 4DPET could be significantly compromised due to patient's irregular breathing pattern and the nature of acquisition time difference between two modalities[68]. In this work, we will focus on the impact of respiratory motion on CT acquisition by comparing the accuracy of 4DCT and 4DCBCT in the ground truth setting with an anthropomorphic respiratory phantom. These results may be informative for treatment planning, treatment verification, longitudinal response assessment, and adaptive radiotherapy for thoracic and abdominal cancers.

II. METHODS

A. Anthropomorphic phantom

The Quasar programmable respiratory motion phantom (Modus Medical Devices Inc., ON, Canada) was used for this study. A custom insert was designed, consisting of a water-filled 24 mm outer-diameter sphere simulating a lung lesion, surrounded by polystyrene pellets comparable to the density of lung. The Quasar phantom has a mount for an infrared marker which moves at a 1:1 ratio to the phantom insert. The motion of the infrared marker was captured with an RPM camera (RPM, Varian Medical Systems, Palo Alto, CA). An image of the phantom is shown in figure 1. The motion of the Quasar phantom is one dimensional (superior-inferior) and can be programmed using sinusoidal breathing traces or representative patient traces distributed with the phantom.
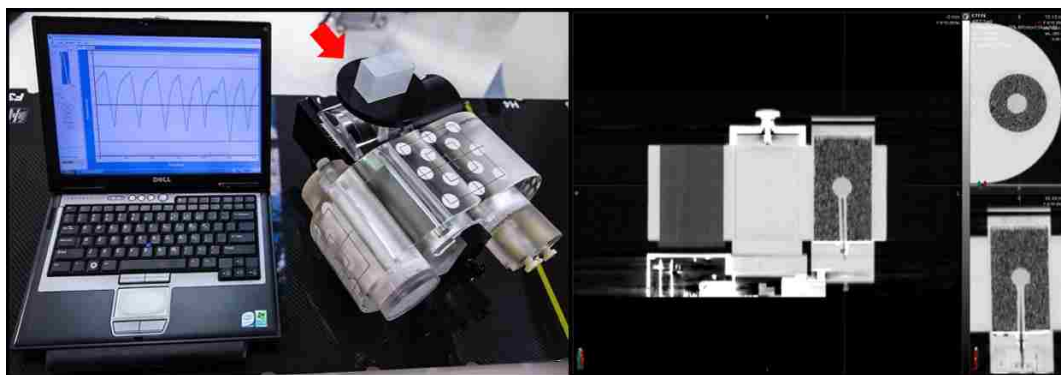
Fig. 1. On left, programmable respiratory phantom with custom anthropomorphic insert. The mount for the infrared marker cubic is indicated with a red arrow. On right, representative CT slice of phantom geometry

B. Phantom motion

To evaluate the fidelity of the 4DCT and 4DCBCT studies, the water sphere was driven by 10 sinusoidal respiratory waveforms (period 3, 4, 5, 6, 7 seconds, 15 and 30 mm amplitude) and 20 patient-derived respiratory waveforms provided by the Quasar software (10 patient waveforms with period 4.2 ± 0.7—6.6 ± 1.6 seconds, nominal 15 and 30 mm peak-to-peak amplitude, mean 9.9 ± 1.2—19.8 ± 2.3 mm amplitude). It should be noted that the patient-specific respiratory waveforms are denoted by their nominal peak to peak amplitudes, however, the mean amplitudes are less in magnitude due to baseline drift in respiration.

C. CT studies

Reference images were acquired of the phantom under static conditions for both CT and CBCT studies. A helical CT scan was acquired using a GE LightSpeed RT16 CT scanner (120 kVp, 320 mAs, 2.5 mm slice thickness, 1.375 pitch factor). For CBCT, the static phantom case was acquired using the Chest M20 F1 preset in Elekta XVI (120 kVp, M20 medium offset field of view with F1 bowtie filter, 40 mA, 40 ms, 660 projections). The water sphere was contoured using threshold segmentation in MIM 6.2.5 (MIM Software, Cleveland, OH) using the known volume of the sphere as ground truth to define segmentation settings. The sphere has a stem which is used to fill the sphere with water; this stem was manually excluded from the contoured volume.

Then, 4DCT and 4DCBCT images were acquired for each motion case, resulting in 30 4D imaging studies (10 sinusoidal, 20 patient-derived). For the 4DCT studies, the cine duration was set as the breathing period plus 1 second. The duration between cine images was set as the respiratory period in seconds divided by 10. All cine CT images were acquired at 120 kVp, 8 mAs, with the same voxel size used in the static study (0.977 mm $\times$ 0.977 mm $\times$ 2.5 mm). All 4DCBCT images were acquired with the Symmetry 4D preset on an Elekta Synergy linear accelerator (Stockholm, Sweden) with M20 field of view, F1 bowtie filter, 120 kVp tube voltage, 20 mA tube current, and 16 ms x-ray pulse length. 1320 projections were acquired over a 360-degree gantry rotation for one CBCT scan.

4DCT studies were phase-sorted into 10 phase images in Advantage 4D (GE Healthcare, Waukesha, WI). The 4DCBCT studies were reconstructed in the XVI software suite (X-ray Volume Imaging ver.4.5, Elekta, Stockholm, Sweden), in ten phases at 128x205x205 voxels and 2.0 x 2.0 x 2.0 mm/voxel. At the time of data analysis, DICOM export of 4DCBCT data was not

possible from the XVI software. Native format 4DCBCT images were reduced in dimensionality from raw 4D data to 10 3D matrices representing individual image phases in ANALYZE format (Biomedical Imaging Resource, Mayo Foundation, Rochester, MN) with VV, a 4D Slicer[172]. Images were then batch converted from ANALYZE to DICOM in AMIDE[173]. 4DCT and 4DCBCT DICOM images were imported into MIM 6.2.5 for image analysis. Object volumes were defined on CT and CBCT images via threshold segmentation, applying the identical threshold as used for the static imaging task. Contours were visually assessed for conformality.

The water sphere was contoured on individual phase images via threshold segmentation on every 4D study. In total 300 4DCT and 300 4DCBCT phase images were analyzed. Differences in the water sphere volumes (compared to the reference volumes) were evaluated. The averages across studies were evaluated, along with the volumes as a function of the phase.

III. RESULTS

A. Segmented volume bias for 4DCT and 4DCBCT imaging

Representative 4DCT and 4DCBCT images are shown in Figure 2. The tabulated percent differences between segmented volumes under motion and the reference volume are shown for 4DCT and 4DCBCT images in Table 1.

Table 1. Segmented volume and percent difference relative to the reference volume as a function of imaging modality, respiratory waveform, and motion amplitude. End-phase volume and difference represent the matrices measured with only maximum inspiration and expiration phases.

Control Volume 7.65 ml	Nominal Amplitude (mm)	Mean Amplitude (mm)	4DCT				4DCBCT			
			Volume (mL)	Difference (%)	End-phase Volume (mL)	End-phase Difference (%)	Volume (mL)	Difference (%)	End-phase Volume (mL)	End-phase Difference (%)
Sinusoid	15	15	6.69±0.82	- 12.8	7.27± 0.14	-5.0	8.28±0.28	8.0	8.28± 0.32	8.2

	30	30	5.54±1.36	**-27.1**	7.07± 0.40	**-7.6**	8.21±0.23	**7.3**	8.32± 0.16	**8.8**
Patient waveforms	15	9.90±1.17	7.16±0.60	**-6.4**	7.16± 0.44	**-6.4**	8.16±0.16	**6.7**	8.11± 0.16	**6.0**
	30	19.80±2.34	6.51±1.51	**-14.9**	6.76± 1.13	**-11.6**	7.92±0.26	**3.5**	7.98± 0.18	**4.3**

The threshold segmentation of the water sphere resulted in a volume of 7.65 mL, 6% greater than the calculated volume of 7.28 mL. With sinusoidal motion of amplitude 15 mm, the threshold volume of the water sphere was found to be underestimated at 6.69±0.82 mL using 4DCT, compared to an overestimation of similar magnitude of 8.28±0.28 mL using 4DCBCT. However, when the amplitude was increased to 30 mm, the magnitude of underestimation was greater for 4DCT at 5.58 ± 1.36 mL, while average volumes measured by 4DCBCT were not greatly changed at 8.21 ± 0.23 mL. Furthermore 4DCBCT volumes were characterized by greater variability over the sinusoidal dataset as measured by standard deviation.
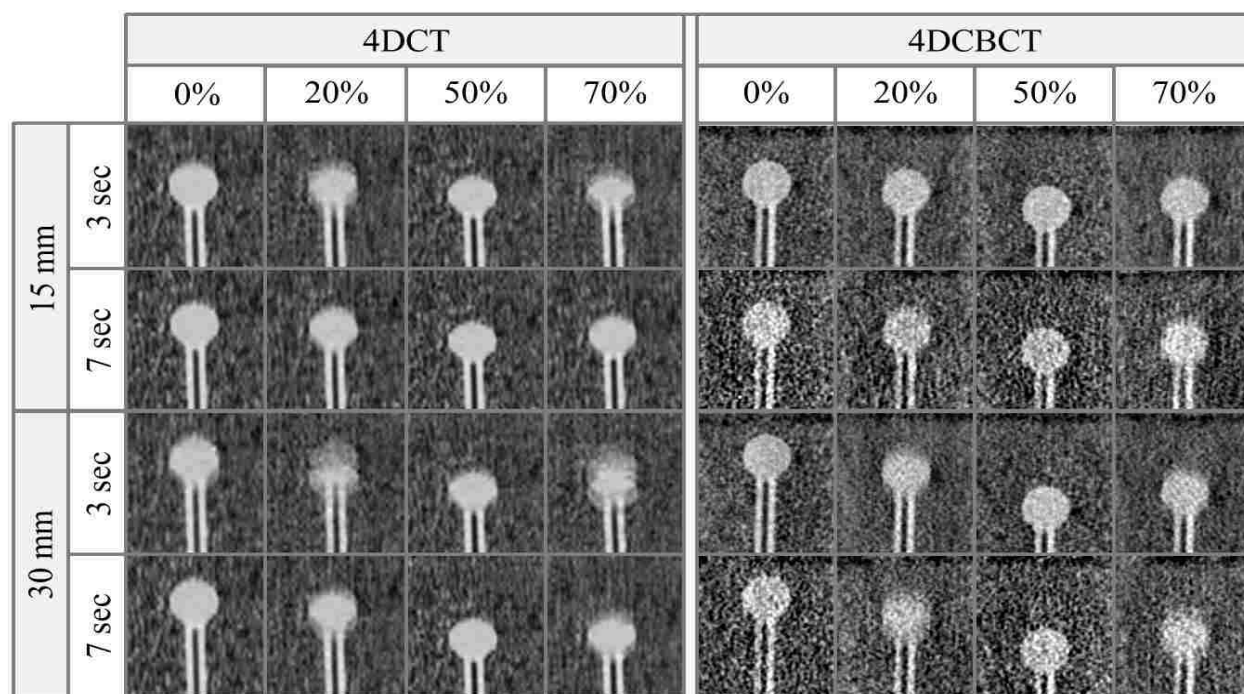

Fig. 2. Representative 4DCT and 4DCBCT phase images for inhale (0%), exhale (50%), and intermediate (20%, 70%)

respiratory phases. For respiratory conditions which correspond to high velocity (low period) or high amplitude, 4DCT images exhibit phase-specific image quality characterized by artifacting and motion blur at intermediate phases. While 4DCBCT images are characterized by increased noise, minimal artifacting at intermediate phases and greatly reduced variability between image phases is seen.

For the patient-derived waveforms of amplitude 15 mm, trends were similar to the sinusoidal case. The threshold volume of the water sphere was found to be 7.16 ± 0.60 mL using 4DCT, compared to 8.16 ± 0.16 mL using 4DCBCT. Again, when the amplitude of the waveforms was increased to 30 mm, greater change in the average volume of the water sphere was found with 4DCBCT (6.51 ± 1.51 mL), compared to 7.92 ± 0.26 mL using 4DCBCT. Three of 20 4DCT patient waveforms, all 15-mm peak-to-peak amplitude with irregular respiration, could not be phase-sorted in Advantage 4D and were excluded from analysis. All 4DCBCT images sets could be phase sorted.

Over all studies, the volumes from the 4DCBCT studies were more accurate than volumes defined on 4DCT images for all motion cases except for the nominal 15 mm patient-specific traces. For sinusoidal waveforms with 30 mm peak-to-peak amplitude, 4DCT image measurements underestimated lesion volume by 27.1% on average (5.54 ± 1.36 mm, range $1.53 - 7.42$ mm). Images segmented on 4DCBCT were more accurate, overestimating lesion volume by 7.3% on average (8.21 ± 0.23, range 7.27—8.56). Similar results were seen for sinusoidal waveforms with 15 mm peak-to-peak amplitude and patient waveforms with 30 mm nominal: images segmented on 4DCT average underestimated lesion volume by 12.8% and 14.9% on average while images segmented on 4DCBCT were more accurate, overestimating lesion volume by 8.0% and 3.5% on average. For the patient waveforms with 15 mm nominal amplitude the trends reversed, with 4DCT underestimating by 6.4% and 4DCBCT overestimating by 6.7%. In this scenario, it should be noted that the 4DCT data set was smaller than the 4DCBCT data set as three patient traces could not be

used for 4D reconstruction as noted in the results section. For all studies, the accuracy was proportional to respiratory amplitude, with greater amplitudes resulting in lower accuracy.

B. Segmented volume for 4DCT and 4DCBCT imaging as a function of respiratory waveform and phase

Graphs depicting accuracy of 4DCT and 4DCBCT imaging as a function of respiratory waveform and image phase are depicted in Figure 3.
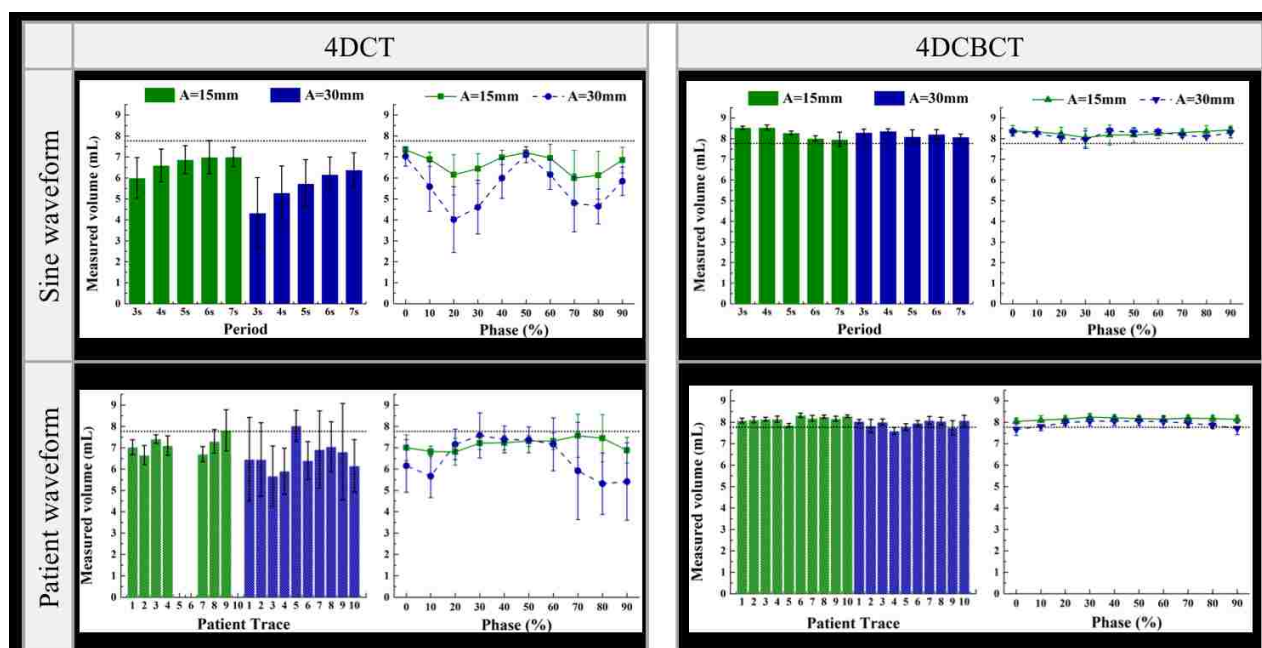
Fig. 3. Segmented volume for 4DCT and 4DCBCT imaging as a function of respiratory waveform and phase. For sinusoidal motion, 4DCT exhibits period-dependent trends where volume recovery decreases with shorter period (greater velocity). Additionally, 4DCT imaging demonstrates phase-dependent trends where volume recovery decreases at intermediate respiratory phases. For patient-specific respiratory motion, phase-specific trends are less pronounced but greatest accuracy is still seen at end-exhale phases. Three waveforms could not be reconstructed in Advantage 4D and were excluded. No strong trends as a function of respiratory waveform or phase are observed for CBCT imaging. Dashed line indicates reference volume.

When evaluating 4DCT images of sinusoidal waveforms as a function of respiratory period, segmented volumes showed reduced accuracy (smaller volumes) with shorter periods (greater velocity). This was observed for the 30 mm amplitude traces, likely due to the fact that greater amplitudes result in greater sphere velocities. For 15 mm sine waveforms, volume recovery

appeared to reach a threshold at periods of approximately 5-6 seconds, above which no benefit was achieved. For 30 mm sine waveforms, no threshold was reached over the range of periods studied (3-7 s). 4DCBCT images showed trends in the opposite direction where longer periods corresponded to smaller volumes, though this trend was smaller in magnitude than that observed for 4DCT imaging.

The variability of volume measured over all 4DCT image phases was large (range 1.50—10.96 mL). Specifically, image phases corresponding to end-inhale and end-exhale phases of the respiratory cycle (0% max. inspiration and 50% max. inspiration) were more accurate than phases corresponding to intermediate portions of the respiratory cycle (*see Table 1*), with this effect being larger for 30 mm sine waveforms than 15 mm sine waveforms. However, volumetric differences from only end-phase imaging between two modalities were still prominent in all combinations of waveform and amplitude (13.2% 16.4%, 12.4%, and 15.9% for 15-mm sinusoid, 30-mm sinusoid, 15-mm patient waveform, and 30-mm patient waveforms, respectively). Differences were not found between end phases and intermediate phases for 4DCBCT imaging.

IV. DISCUSSION

4DCT and 4DCBCT are routinely used in external beam radiation therapy, with 4DCT used at the time of patient simulation and treatment planning and 4DCBCT used at the time of patient treatment. The volume, shape, and position of these two studies are often compared, with the assumption that the differences between the studies are only related to the image quality (e.g. noise, HU bias, spatial resolution) and that volumetric differences are due to anatomic differences alone (e.g. tumor progression or response to therapy). We investigated the volume accuracy and difference of 4DCT and 4DCBCT imaging under the common clinical settings in the ground truth

setting with a respiratory phantom. We found that systematic volume differences could be observed where no volume differences should exist in both sinusoid and patient scans, and 4DCBCT measurement was closer to the truth in most of cases. These volumetric differences between two modalities could be mitigated to a certain extent by choosing end-inhale and end-exhale phases to compare (where the lesion velocity is minimized) and by understanding where discrepancies in volume increase (large amplitude breaths, short breathing cycle). These findings have implications for clinical practice, including verification that treatment planning margins sufficiently encompass tumor motion, construction of maximum intensity and average intensity projections for treatment planning, assessment of longitudinal dose accumulation, or decision to adaptively re-plan based on CBCT imaging.

While both imaging modalities produced artifacts that limited their accuracy, 4DCBCT yielded image-defined target volumes closer to ground truth than 4DCT for all but one of the scenarios tested (15 mm amplitude, patient-derived waveforms). While the use of broad x-ray beams and flat panel detectors inherent to CBCT has led to criticism of image quality due to artifacts caused by scatter and differences in x-ray energy spectrum across the panel, this technology appears well-suited for motion assessment. The modest overestimation of imaging volume was likely due to motion blur, as subjectively 4DCBCT can contain motion blurring artifacts while 4DCT is seen to "freeze" object motion, as well as greater scatter with the broad beam geometry. Beyond lower overall accuracy for 4DCT imaging, object volume measured on the individual phases of the 4DCT varied widely, with the most accurate volume definition being end phases, where the sphere velocity was minimized. Results suggest that 4DCT simulation may underestimate tumor motion, especially in patients with large motion amplitudes.

One limitation of our study is that the respiratory phantom used to simulate the lesion movement had motion only in the S-I direction and respiratory motion naturally occurs in three dimensions. Our finding of inaccuracy in intermediate respiratory phases might lead to greater motion discrepancies in the common case of "c-shaped" respiratory motion. Although we showed the measured volumes between two modalities could also be very different in patient-waveform scans, even if end-phase volume measurements were only phases to be considered, other important matrices for the image-guided radiation treatment (IGRT) process like the bias of tumor motion between CT and CBCT is not reported here because it could not be fairly evaluated with our 1-D phantom motion setup. Previous studies have reported on similar differences in respiratory motion in patients; e.g. Purdie *et al.*[167] reported that two out of twelve patients showed significant tumor motion differences (distance between end-inhale and end-exhale phases of tumor position) between 4DCT and 4DCBCT measurements.

The difference in 4DCT and 4DCBCT can be explained in part through the physics of image acquisition, notably differences in cone-angle coverage and in acquisition time. While CBCT images were acquired with a large flat-panel detector, CT images were acquired with a regular 16-row detector (around 2.0 cm in z-direction). The consequence of this is that tumor motion is in the imaging field of view for the entire acquisition for CBCT imaging, but only for several image slices for the CT acquisition. Additionally, the tumor is in the imaging field of view for a shorter period of time for 4DCT (~5-10 sec vs. 3.5-4 min in 4DCBCT) which may cause bias in patients with irregular respiratory motion because only a small portion of the breathing motion range was covered during the short CT scan[68,123,174]. Another challenge is that threshold segmentation settings

of ROI were defined on static CT acquisitions. Threshold segmentation has known limitations with reproducibility across scanners and acquisition settings. In this study acquisitions-specific threshold settings were determined from the ground truth case. However, for the 4DCT scan, image noise and HU bias are expected to be higher in the low-dose cine acquisition than the helical scan. For CBCT, there were differences in mAs and acquired projections between the 3D and 4D scan. We chose the default manufacturer acquisition profiles for these scans because CBCT parameters are not routinely changed by Elekta XVI users. However, discrepancies in image noise due to photon starvation could be confounding factors in measuring the volume.

The above limitations in terms of image quality imply that conventional protocols used in the 4DCT and 4DCBCT imaging process may not be able to reflect the true anatomic differences from tumor progression or treatment response at this time. To address these challenges, a large body of research is being performed to improve image accuracy under respiratory motion. For 4DCT, optimized low-dose CT protocols[88,136,150,175], scatter corrections[176,177], approaches regarding the acquisition time[174], motion modeling[178], and more advanced motion gating techniques[63,179,180] are being investigated. For 4DCBCT, reconstruction and motion binning techniques[181,182] are being developed. Evaluating improvements from these methods so that the lesion volume under the respiratory motion can be more accurately estimated by both 4DCT and 4DCBCT is a direction for future work.

V. CONCLUSION

Respiratory-correlated CT and CBCT imaging is critical for radiation treatment in thoracic cancers. In this study using a dynamic respiratory motion phantom to study the accuracy of 4DCT and 4DCBCT imaging in the ground truth setting, some advantages were seen in both modalities,

but 4DCBCT images were generally more accurate and reproducible than those measurements derived from 4DCT images due to the reduced presence of respiratory motion artifacts. These results may be relevant to radiation oncology in the areas of target volume definition, verification imaging, longitudinal response assessment, and adaptive re-planning.

VITA

Tzu-Cheng (Efren) Lee

845 NE 66TH ST. APT502,
Seattle, WA98115
206-351-5368, efrenlee@gmail.com

EDUCATION

Ph.D., Bioengineering, Dec. 2017
University of Washington, Seattle, WA
Thesis: Ultra-low-dose CT-based attenuation correction for respiratory motion compensation in PET/CT imaging. Advisor: Dr. Paul E. Kinahan

M.S., Biomedical Imaging, Sept. 2012
University of California - San Francisco, San Francisco, CA
Thesis: Tibia and vertebra bone structure changes in old-male spontaneously hypertensive rats by quantitative micro-CT. Advisor: Dr. Youngho Seo

M.S., Biomedical Science, B.S., Chemistry, June 2009
National Chiao-Tung University, Hsinchu, Taiwan
Thesis: Rapid phenotypes determination of human haptoglobin by a lab-made bio-electrochemical analyzer. Advisor: Dr. Chia-Ching Chang

RESEARCH INTERESTS

- Advanced methods and algorithms for medical imaging systems

PROFESSIONAL EXPERIENCE

CT Reconstruction Scientist, CT Physics and Reconstruction,
Toshiba Medical Research Institute (a Canon group), USA — June 2017 - Now

- Advanced de-noising and scattering correction algorithms

Summer Internship, CT Physics and Reconstruction,
Toshiba Medical Research Institute, USA — July 2016 - Sept. 2016

- Model-based scattering correction approach for the cone beam CT imaging

Pre-Doctoral Research Associate, Imaging Research Laboratory,
Department of Radiology, University of Washington — Sept. 2013 - Dec. 2017

- Demonstrated a respiratory phantom study to examine the most reliable 4D-CT attenuation correction methods for more accurate quantitative information from 4D PET imaging of lung-lesion examinations, and evaluated its potential

improvement on the accuracy of the following image-guided oncological radiotherapy

- Evaluated the potential of using the cone-beam CT scanner to the conventional fan-beam CT scanner for more precise morphological and positional image recoveries of the lung phantom insertions which was affected by irregular respiratory motions

- Compared prone versus supine position of ^{18}FDG PET scan of a breast phantom, and suggested that the prone position will not compromised the uptake recovery values so that it will be a better scan position for PET and MRI multi-modality studies

Junior Specialist & Graduate Student Resident, **Physics Research Lab, Department of Radiology, University of California - San Francisco**   **Apr. 2012 - June 2013**

- Designed and performed the experiment to examine the changes of bone structure in the end-stage cardiovascular diseased rat models with the techniques of quantitative micro-CT and finite element analysis.

- Trained for operating the "Geant4" platform to compute the Monte Carlo simulation for better prediction of radioactivity distribution of a new-designed multi-pinhole collimator for the SPECT imaging.

- Completed the first striatal phantom study with a set of new-design 20 multi-pinhole collimators for SPECT imaging, and proved it had much higher signal efficiency for DaT scan than using conventional parallel-hole collimators.

Research Assistant, Nano-bio & Biophysics Lab, Institute of Molecular Medicine & Bioengineering, National Chiao Tung University, Taiwan — Sept. 2007 - June 2009

- Constructed an electrochemical impedance biosensor to replace the electrophoresis separation method in order to rapidly verify the different phenotypes of human haptoglobin.

PUBLICATIONS

- **Lee, T.-C.**, Bowen, S. R., St. James, S., Sandison, G. A., Kinahan, P. E., and Nyflot, M. J. "Accuracy Comparison of 4D Computed Tomography (4DCT) and 4D Cone Beam Computed Tomography (4DCBCT)" ***International Journal of Medical Physics, Clinical Engineering and Radiation Oncology,*** 6(3), 323-335, Aug. 2017.

- **Lee, T.-C.**, Zhang, R., Alessio, A., Fu, L., De Man, B., Kinahan, P. "Statistical distributions of ultra-low dose CT sinograms and their fundamental limits" ***SPIE Medical Imaging Proceedings***, 101320N–101320N–7, Apr. 2017.

- Fu, L, **Lee, T. -C.**, Kim, S.-M., Alessio A.M., Kinahan P.E, Chang Z., Sauer K., Kalra, M., De Man, B. "Comparison between Pre-log and Post-log Statistical Models in Ultra-Low-Dose CT Reconstruction" ***IEEE Transactions on Medical Imaging***, 36(3), 707-720, Mar. 2017.

- **Lee, T. -C.**, Alessio, A. M., Miyaoka, R. M., & Kinahan, P. E. "Morphology supporting function: attenuation correction for SPECT/CT, PET/CT, and PET/MR imaging." ***The Quarterly Journal of Nuclear Medicine and Molecular Imaging***, 60(1), 25–39, Mar. 2016.

- Nyflot, M. J., **Lee, T.-C.**, Alessio, A. M., Wollenweber, S. D., Stearns, C. W., Bowen, S. R., and Kinahan, P. E. "Impact of CT attenuation correction method on quantitative respiratory-correlated (4D) PET/CT imaging." ***Medical Physics***, vol. 42, no. 1, Jan. 2015

- Williams, J. M., Rani, S. D., Li, X., Arlinghaus, L. R., **Lee, T.-C.**, MacDonald, L. R., et al. Comparison of prone versus supine 18F-FDG-PET of locally advanced breast cancer: Phantom and preliminary clinical studies. ***Medical Physics***, 42(7), 3801–3813. July 2015.

- **Lee, T.-C.** Bowen, J.D. Ellin, J.R. Shrestha, U. Gullberg, G.T. and Seo, Y. "Multipinhole collimator with 20 apertures for a brain SPECT application." ***Medical Physics***, vol. 41, no. 11, p.112501, Nov. 2014.

- **Lee, T.-C.** Burghardt, A. J. Yao, W. Lane, N.E. Majumdar, S. Gullberg, G.T. and Seo, Y "Improved trabecular bone structure of 20-month-old male spontaneously hypertensive rats.," ***Calcified Tissue International***, vol. 95, no. 3, pp. 282–291, Sep. 2014.

- Bowen, J.D. Huang, Q. Ellin, J.R. **Lee, T.-C.**, Shrestha, U. Gullberg, G.T. and Seo, Y. "Design and performance evaluation of a 20-aperture multipinhole collimator for myocardial perfusion imaging applications.," ***Physics in Medicine and Biology***, vol. 58, no. 20, pp. 7209–7226, Oct. 2013.

- Cheng, T.-M. **Lee, T.-C.** Tseng, S.-H. Chu, H.-L. Pan, J.P. and Chang C.-C. "Human haptoglobin phenotypes and concentration determination by nanogold-enhanced electrochemical impedance spectroscopy.," ***Nanotechnology,*** vol. 22, no. 24, p. 245105, Jun. 2011.

- Chang, C.-C. Chen, P.-H. Chu, H.-L. **Lee, T.-C.** et. al. Chou, C.-C. Chao, J.-I. Su, C.-Y. Chen, J.-S. Tsai, C.-M. Ho, Y.-P. Sun, K.-W. Cheng, C.-L and Chen, F.-R. "Laser induced popcornlike conformational transition of nanodiamond as a nanoknife," ***Applied Physics Letters***, vol. 93, no. 3, p. 033905, Jul. 2008.

RESEARCH AWARD

- ***Student Travel Award,*** SPIE Medical Imaging Conference, 2017, Orlando, FL.
- ***Awardee of Study Abroad Fellowship***, Ministry of Education Fellowship and Scholarship Program, 2015, Taiwan.
- ***Winners of the Young Investigator's Presentations (3rd place),*** 2014 NW AAPM Fall Meeting, 2014, Seattle, WA.
- ***Award to Excellence in Format, Content and Presentation***, 24th Joint Annual Conference of Biomedical Sciences, 2009, Taiwan.

CERTIFICATE AND RELATIVE SKILLS

- Skilled in operating many imaging instruments: µCT, CT, PET/CT, SPECT/CT system, IVIS bioluminescence imager, confocal laser microscopy.
- Proficient in image processing language and software: Python, Tensorflow, MATLAB, OsiriX, AMIDE, ImageJ.

OTHER EXPERIENCE

Curriculum committee student representative, Department of Bioengineering, University of Washington, Seattle, WA — Sept. 2015 - June 2017

Vice Chair, iTaiwan Graduate Student and Professional Association, University of Washington, Seattle, WA — June 2016 - June 2017

Internship, Manufacturing Techniques Department, AU Optronics, Taoyuan, Taiwan — Apr. 2011 - July 2011

Second Lieutenant , Army Military Police, Ministry of National Defense Taiwan, Taichung, Taiwan — Aug. 2009 - July 2010